UNIVERSITÀ
DEGLI STUDI
FIRENZE

Università degli Studi di Firenze
European Laboratory for Non-Linear Spectroscopy

PhD in Atomic and Molecular Photonics

CYCLE XXXVI

Advancing Anti-Matter-Wave Interferometry: Design and Implementation of Techniques for Gravity Measurement on Positronium Atoms

Academic Discipline (SSD) FIS/03 Fisica della Materia

Supervisor:
Prof. Guglielmo Maria Tino

Candidate:
Giuseppe Vinelli

Co-Supervisor:
Dr. Leonardo Salvi

PhD Coordinator:
Prof. Diederik Wiersma

September 2024

Abstract

Advancing Anti-Matter-Wave Interferometry: Design and Implementation of Techniques for Gravity Measurement on Positronium Atoms

by Giuseppe Vinelli

This thesis explores the application of matter-wave interferometry techniques to antimatter, with a particular focus on measuring the gravitational effect on positronium atoms using a Large Momentum Transfer (LMT) interferometer and a high-power cavity for photodetachment of the negative positronium ion. The experimental phase of the photodetachment process is currently being refined, with simulation activities demonstrating the feasibility of the experiment and guiding the optimization of the experimental setup. Optical cavity simulations using the OSCAR package, FEM simulations via Ansys for thermal effects, and Monte Carlo simulations for beam divergence have been conducted. Results indicate that thermal effects are negligible and a circulating power of about 200 kW is achievable. The cavity has been assembled and tested in air, showing promising characteristics similar to high-finesse cavities.

The final part of the thesis involves designing a single-photon LMT interferometer (SPLMT) to measure gravitational effects on positronium, operating with a fast atomic beam and high energy spread to accommodate the short lifetime of positronium. Simulations indicate that with a 10^8 Ps/s beam, an angular divergence of 10 mrad, and a relative measurement precision of $\Delta g/g = 10\%$, a data integration time of approximately 11 months is required. Quantum simulations for parasitic pattern influence show negligible effects. Comparisons between SPLMT and Bragg interferometers reveal that the SPLMT approach offers greater sensitivity due to its robustness against the Doppler effect.

This work lays the groundwork for future developments in the positronium gravity measurement, highlighting its potential impact on understanding gravity on quantum scales and verifying fundamental physics theories. The results provide a foundation for further advancements in matter-wave interferometry and antimatter physics.

Acknowledgements

This thesis represents only a small part of the personal and professional growth I have experienced during my doctoral years. Throughout this period, I have learned a great deal, and for this, I wish to express my gratitude to all the people with whom I had the privilege of collaborating and sharing various experiences.

A special thanks goes to Gabriele, Leonardo, and Paolo, who, with tireless dedication and remarkable generosity, have taught me everything I know about laboratory work. Their guidance was always accompanied by a good dose of humor, making every experience more stimulating and enjoyable. They have been a true model of passion and commitment to their work and their beliefs.

I would like to express my gratitude to my Supervisor, Professor Guglielmo Tino, and Professors Marco Giammarchi and Rafael Ferragut, for giving me the opportunity to embark on this journey. Their advice, enlightening discussions and support, along with that of the groups from Milan and Como, whom I sincerely thank, have greatly contributed to my growth.

I am also grateful to Professor Holger Müller and Dr. Richard Hobson for their thorough review of my thesis, offering valuable suggestions and insights that have enriched this work.

My thanks also go to Istituto Nazionale di Fisica Nucleare, which believed in the QUPLAS project, partially described in this thesis, and which has inspired me and many other scholars, as well as individuals outside the research world, captivated by the beauty and mystery of nature.

I would like to thank Università di Firenze and European Laboratory for Non-Linear Spectroscopy for the honor of being part of such a prestigious program.

A special thanks goes to the lunch group friends for the conversations, laughter, company, and discussions that have enriched me both personally and intellectually.

A heartfelt thanks to my family, always present and loving, despite my (only apparent) distance.

Finally, my deepest thanks go to Agnese, my life companion and cornerstone of my journey.

Contents

Introduction

This thesis aims to apply matter-wave interferometry techniques to antimatter, seeking to advance the current state of the art. Its objective is to assess the experiment's feasibility while highlighting critical aspects in its implementation. The subsequent discussion primarily revolves around designing and developing a Large Momentum Transfer (LMT) Mach-Zehnder interferometer to measure the gravitational effect on positronium atoms, along with addressing the construction of a high-power optical cavity for photodetachment of the negative ion of positronium. It should be noted that part of this discussion involves experimental work on the photodetachment stage, which is currently being refined, but being a project in the design phase, most of this work has been devoted to simulation activities.
This study is part of a project named QUPLAS (Quantum interferometry with Positrons and LASers), based in Italy and primarily distributed across the University of Milan, Polytechnic of Milan, at the L-NESS laboratory in Como, and the University of Florence at the physics department in Sesto Fiorentino. The project benefits from a significant contribution from Istituto Nazionale di Fisica Nucleare.

Positronium (Ps) is the hydrogen-like quasi-stable bound system of an electron and its antiparticle, the positron. Ps is the lightest element (about 10^3 times lighter than hydrogen) and exists in the ground state in two sublevels depending on the spins of the electron and positron: singlet (para-Ps, spin 0) and triplet (ortho-Ps, spin 1). Given the multiplicity of these states, positronium in the ground state forms as 75% ortho-Ps and 25% para-Ps. Their lifetimes in vacuum are very different, 0.125 and 142 ns for para-Ps and ortho-Ps, respectively. Also, the annihilation characteristics in vacuum are different: para-Ps annihilates with emission of two gamma rays of 511 keV each (equal to $m_e\mathrm{c}^2$, with m_e the electron rest mass), while ortho-Ps annihilates by emitting at least three gamma rays with a maximum energy of 511 keV each and with a total energy of $2m_e\mathrm{c}^2$. Given the short lifetime of para-Ps, only the triplet state (ortho-Ps) is of interest for this work and in the context of this thesis Ps will always mean ortho-Ps.

Since its discovery [1], Ps has been the subject of many experimental and theoretical investigations (see e.g. [2, 3]). Indeed, as the simplest purely leptonic bound state, Ps, together with muonium, gives a privileged opportunity for high-precision studies of quantum electrodynamics (QED) [4, 5]: the low electron and positron mass implies that weak force contributions to Ps energy levels are negligible [6], and that Ps is well described as a bound-state QED system. Measured deviations from theoretical predictions can then be interpreted as possible indications of new physics [2, 7–10]. Being neutrally charged, Ps has also the advantage of being insensitive to external electric fields that probably represent the main difficulty in measuring the gravitational fall of free electrons [11]. In recent decades, interest in this atom has grown considerably also thanks to the development of positronium beam technology [12]. Two of the main limitations in dealing with the Ps atom are its reduced lifetime and the possibility of annihilation with electrons in the surrounding environment; this implies that to obtain intense Ps beams it is necessary to work with high Ps velocities and efficiently guide the atoms in an ultra-high vacuum system.

The effect of the Earth's gravitational field on antimatter is the subject of ongoing research and discussions at present and during the last decades [13–24]: any differences in the gravitational behavior between matter and antimatter would in fact represent a violation of Einstein Equivalence Principle (EEP). Antimatter gravitation has never been measured, except for a result obtained by the ALPHA collaboration at CERN, showing that anti-hydrogen atoms behave in a way consistent with gravitational attraction to the Earth measuring an acceleration $a_{\bar{g}} = 0.75 \pm 0.13\,(\text{statistical+systematic}) \pm 0.16\,(\text{simulation})g$ [25], which needs more precise investigation to address theoretical issues about fundamental laws also because of the non negligible contributions of the weak force.

This kind of experiments can often take advantage of the accuracy of interferometry to measure gravitational effects. Solutions based on different types of interferometry have been proposed, also for antimatter [26]. Some of these rely on Ps excitation to high-order Rydberg states to increase its lifetime [27, 28].

In this thesis, I propose a new approach for measuring the gravitational effect on positronium (Ps) atoms, involving the development of a Mach-Zehnder Large Momentum Transfer (LMT) interferometer and a photodetachment stage for detaching an electron from the negative Ps^- ion. The subsequent discussion encompasses the design and development of the photodetachment cavity, the design of the LMT Mach-Zehnder interferometer, and exploration of the photodetachment process: I will present simulation results to assess the impact of the photodetachment process on the atomic beam, as well as for the design of the high-power cavity intended for this purpose. Additionally, I will detail the experimental phase of the photodetachment process, encompassing the construction and characterization of the cavity in its current stage of ongoing work. I will discuss the interferometer geometry, show numerical simulation results, and estimate the data taking time required to achieve a given accuracy on the gravity acceleration measurment. The work is organized as follows.

After a presentation of the theoretical interest in Ps gravitation in Chapter 1, I give an overview of the stages of the experiment by mentioning the production and preparation of atoms in 1.1. In Chapter 2, we will discuss the main figures of merit of an atomic interferometer and take a look at the theory behind its applications for gravity measurements. In Chapter 3, we will discuss the photodetachment stage, discussing the finite element simulation of the optical cavity mirrors for the evaluation of the thermal effect and the simulation of the optical cavity based on the fast Fourier transform (FFT). Finally, in section 3.3 I will present the experimental activity of this thesis, which consists of the construction and locking photodetachment cavity. In Chapter 4 I describe the LMT interferometer, its main operating parameters and the numerical simulations used to determine the integration time of the experiment and the influence of parasitic interferometers. The results are compared with another interferometric light-pulses approach proposed in the literature [21] in section 4.3.

Chapter 1

Motivation and design of the experiment

The study of gravitation with systems containing antimatter addresses some of the main unresolved issues in Modern Physics.
First of all, our Universe features a striking particle-antiparticle asymmetry; according to the widely accepted Big Bang scenario [29], the unbalance was generated close to the Grand Unification era, around 10^{-35} s of cosmic evolution time. Therefore, at the time of baryon formation (temperature of 10^{13} K, or 10^{-6} s) only protons and neutrons could be formed, and not their antiparticles. The likely explanation of this effect is some level of violation of fundamental laws (like CP invariance, the combination of Charge and Parity symmetries) as well as the occurrence of the Sakharov conditions [30], all of this implying that only baryons (and not anti-baryons) fueled the first stages of cosmic nucleosynthesis.

While the Standard Model of particle physics has the possibility of naturally generating CP violation for instance through the phase of the Cabibbo-Kobayashi-Maskawa mixing matrix in the hadronic sector, the amount of violation seems largely insufficient to explain the primordial asymmetry.

The Standard Model itself, despite of its remarkable successes, appears to be an incomplete theory for a variety of reasons: it does not include gravitational interaction, and does not explain the oscillation of neutrinos or the existence of dark matter and dark energy, constituting the vast majority of the energy budget of the Universe. Finally, it does not satisfactorily explain the predominance of matter over antimatter in the Universe. Moreover, it seems natural that new Physics or some violation of fundamental laws would appear at energies close to the Planck-scale, because of the unavoidable interplay between Quantum Physics and Gravitation, which in turn could lead to residual effects at the present energy level.

For these reasons, the study of antimatter holds the possibility of both improving the Standard Model and to shed light on the composition of our Universe. Matter and antimatter are related by two key symmetries of Modern Physics: Charge-

Parity-Time reversal (CPT) and the Einstein Equivalence Principle (EEP). CPT invariance is the main theoretical tool linking particles and antiparticles at the quantum level and in a flat spacetime. The EEP, on the other hand, relates any form of matter and energy, for instance, through the feature of Universal Free Fall, but only at the macroscopic level in any curved spacetime. For these reasons matter and antimatter asymmetry can effectively be addressed by studying the behaviour of subatomic particles in a gravitational field.

In spite of its short lifetime, Ps offers two important features which make it a very interesting system from this point of view. First of all, it is the only bound system made of elementary constituents of the Standard Model. Its mass is therefore directly composed by key parameters of the model, while (for instance) the mass of an antiproton is mostly made of the energy of the color field, and not of the mass of the quarks. From the theoretical viewpoint, possible violations of fundamental symmetries (Lorentz Invariance, CPT and the EEP) are related by the Greenberg's theorem [31] and – more in general – by the framework of the Standard Model Extension (SME) [32, 33]. The SME is an effective field theory combining General Relativity and the Standard Model, aimed at extending the Standard Model of elementary particles to include in a gauge-invariant way all the possible spacetime operators violating CPT and Lorentz symmetry. The main goal of the SME is to provide a theoretical framework for exploring and testing deviations from the Standard Model through precision experiments. By measuring the coefficients of the additional terms introduced by the SME, scientists can search for signs of new physics beyond the Standard Model, such as dark matter, supersymmetry, or other theories that extend the description of elementary particles. In the frame of the SME, the hydrogen-antihydrogen gravitational difference depends on a combination of four Lorentz violating parameters (CPT-odd and CPT-even coefficients for antiproton and positron) that also incorporate the influence of the color field. Instead, the gravitation of Positronium, because of his highly symmetric structure (elementary particle with its own antiparticle), is only sensitive to the CPT-even Lorentz violating parameter c_e:

$$\left.\frac{\Delta g}{g}\right|_{\mathrm{Ps}} = \frac{8}{3} c_{\mathrm{e}} \tag{1.1}$$

So that, Ps gravitation is directly sensitive to pure fermionic masses in the Standard Model and holds the potential to determine unambiguously the c_e parameter of the SME. It has been shown that gravitation with Ps can address CPT-even Lorentz violation already at the 10% accuracy level [34].

1.1 Design of the experiment

The basic principle of the experiment analyzed in detail in this thesis is to exploit the relationship that links the phase shift of the wavefunction of an atom passing through an interferometer $\Delta\Phi$ and a generic gravity acceleration g (eventually different for antimatter):

$$\Delta\phi_{\mathrm{g}} = k_{\mathrm{eff}} g T^2 \tag{1.2}$$

with T the interrogation time (half of the propagation time through the whole interferometer) and k_{eff} the effective transferred momentum from the laser pulses of the interferometer to Ps atoms. As will be explained in Chapter 2, the relevant quantity to be measured is the number of atoms leaving one of the two arms of the interferometer, which depends on the cosine of the phase shift [35–38]: $N_{out} = N_0[1 + C\cos(\Delta\phi)]$, where N_0 is half of the total number of atoms considered, C is the contrast of the interferometer, and $\Delta\phi$ contains $\Delta\phi_g$. To measure this phase shift, a beam of Ps atoms is clearly needed and it must eventually be excited to the state chosen for the interferometer. In this work I present the design of a LMT Mach-Zehnder interferometer which makes use of single-photon transitions between the $n = 2$ state and the dipole-allowed $n = 3$ Ps states. The laser light is designed to have a wavelength of 1312 nm and to be circularly polarized to exploit the 2-3 transition by using the states $2^3\mathrm{S}_1$ with m_{J}=1 and $3^3\mathrm{P}_2$ with m_{J}=2. These states and light polarization have been chosen to ensure that the transition can be well described by a two-level system formalism (the circularly polarized light can excite this transition only). The Ps must therefore enter the interferometer in the state $2^3\mathrm{S}_1$ with m_{J}=1.

To produce a Ps beam, it is necessary to produce a positron (e^+) beam. There are several ways to do this: some involve the use of a radioactive source such as ^{22}Na [39] that decays $\beta+$; others, as in the production of positron beams for medical applications or for high energy physics, generate an electron beam and convert it to e^+ by absorption of brehmstrahlung photons in the nuclear field [40,41]. Once an e^+ beam has been produced, it is possible to convert it into relatively slow Ps (energy on the order of tens of meV) by passing it through mesoporous materials [42–44]. This method, however, does not allow Ps to be directed and focused by electrostatic focusing since, being neutrally charged, it is immune to the action of electric fields. One way to obtain a Ps collimated beam is to guide Ps^- ions leaving a positron-Ps^- converter [45–47]. The advantage of producing Ps through the negative Ps^- ion, compared to Ps formed in mesoporous materials, is the possibility to obtain a tunable and monoenergetic beam with low divergence and high coherence well suited for interferometric experiments [48]. On the other hand, the disadvantage is the short Ps^- lifetime (479 ps), so a very compact system is needed to produce, accelerate and focus the Ps^- beam via electrodes. This topic is discussed in Ref. [49], where a proposal to produce a Ps beam is presented: the idea is based on production, acceleration and focusing of Ps$^-$ ions, followed by photodetachment of one electron via high-power cavity pumped by an Erbium fiber laser [50], leaving Ps essentially in the ground triplet state. We will explore this issue further in the section 3.2. After the Ps beam production stage, the atoms will be prepared according to the following additional steps:

i. 243 nm laser excitation to $2^3\mathrm{P}_0$;

ii. 18 GHz microwave excitation to $2^3\mathrm{S}_1$ (m_J=1).

For the UV transition, a magnetic field is needed to define a quantization axis. To avoid Doppler effects in excitation the laser beam is directed perpendicularly to the Ps collimated beam. Excitation of one or all the ground triplet states, corresponding to transitions Δm_J=0, ±1, is obtained with suitable linearly polarized light. The second excitation uses circular polarization to selectively couple the $2^3\mathrm{P}_0$ and $2^3\mathrm{S}_1$ in a $\sigma+$ transition. A similar UV-microwave excitation scheme can be found in Ref. [51]. Starting from Ps$^-$, the Ps preparation, the interferometer and the detection stage are shown in Figure 1.1.

Note that the state chosen for the interferferometer ($2^3\mathrm{S}_1$ with m_J=1) is optimized

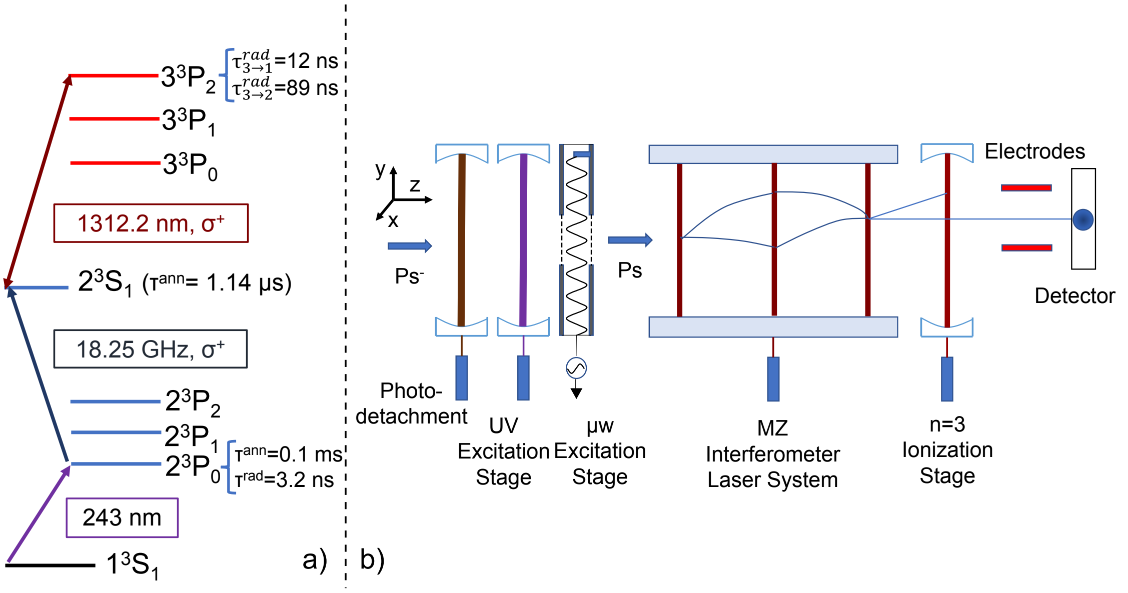

Figure 1.1: a) Energy level scheme of Ps, transitions and lifetimes [12, 52]. b) Representation of the Ps preparation, interferometric and detection stages. The Ps$^-$ beam is photodetached so that the resulting Ps beam is excited to the $2^3\mathrm{S}_1$ state and propagates through the Mach-Zehnder interferometer. At the end of the apparatus, the $n = 3$ state is ionized, and the particles that have remained charged are swept away by a moderate electric field, leaving the Ps ($n = 2$) state to be detected. In the scheme, gravity acts along the negative y direction and the Ps$^-$ production system is not shown.

to be as insensitive as possible to external electric and magnetic fields: m_s=±1 states with zero orbital angular momentum experience a negligible effect of magnetic fields [53] (unlike common matter atoms having spin pairs, such as atoms with two valence electrons), and electric fields have only second-order effects for m_J=1 [12]. This makes the system particularly robust with respect to external perturbations. The Ps preparation stage is not the focus of this work so it will not be covered further.

After crossing the interferometer (which will be described in detail in Chapter 4), the weakly bound $n = 3$ state is laser-ionized [28] by means of an Erbium fiber laser at 1560 nm in order to allow the measurement of the number of $n = 2$ Ps atoms alone (Figure 1.1). The still charged particles (electrons and positrons) are swept away by means of a moderate electric field. This choice is motivated by the fact that, without the removal of the $n = 3$ level, in order to distinguish between the $n = 2$ and $n = 3$ populations, one would need to drastically increase the spatial distance between them requiring the addition of a considerable number of pulses (and linear space) to the interferometer. At least eight π pulses and one meter of propagation would be required downstream, admitting a maximum angular divergence of the order of few tens of microradians. Given the speeds involved, this constraint would require an additional 3 meters of upstream collimation resulting in a substantial Ps beam population loss due to annihilation. Given the interferometer's tendency to scatter atoms that have not interacted properly with the laser pulses, the signal-to-noise ratio at the detector can be greatly improved by affixing a physical mask that selects the area with the highest signal concentration.

Since the $n = 3$ atoms are not on the same detector, it is not necessary to distinguish them from the $n = 2$ states and therefore detector spatial resolution is not required. There are several possibilities for this type of detection. Some of these are scintillators, microchannel plate detectors, which are still sensitive to the atomic velocities involved [54], or germanium detectors [55, 56]. Once the $n = 3$ atoms have been ionized, they can be counted for flux normalization by detecting the free positron annihilation events by means of germanium detectors or by counting the electron charge (e.g. by means of a Faraday cup).

1.2 Brief overview of the Ps beam production system

The apparatus for the production, acceleration, and focusing of Positronium is currently in the design phase by the team of Politecnico di Milano and is not among the topics covered in this thesis. However, we will discuss some key points of this system here to provide a broader overview of the experimental setup.

The initial phase of the QUPLAS project (referred to as QUPLAS-0) utilized a positron beam to measure, for the first time, an antimatter interferometric signal with Talbot-Lau interferometry and material gratings [57]. Its apparatus obtained positrons from the $\beta+$ decay of a 4 mCi ^{22}Na source, subsequently accelerated, transported, and focused using an electrostatic electrode system (see Figure 1.2).

To moderate the positrons and reduce their energy spread, they pass through a 1 μm tungsten foil, resulting in about 0.1% of the initial beam being released with an energy of approximately 2 eV.

A crucial component of the setup is a 90° bend in the electrode system, designed to exclude high-energy positrons and diminish secondary γ photon flux originating from the ^{22}Na source. However, this bend introduces beam aberrations and losses, necessitating the use of three additional lenses to refocus, accelerate, and focus the beam onto the target, which serves as the first grating of the interferometer.

The final kinetic energy of the positrons can be adjusted within a maximum value of 20 keV by varying the voltage of the apparatus. The configurations of the potentials shown in Figure 1.2b corresponds to a final kinetic energy of 1 keV and the last electrode is grounded to allow unimpeded particle propagation through the interferometer.

High-voltage control electronics enable users to optimize beam focusing by modifying relative potential differences. The resulting focused beam spot exhibits a Gaussian intensity profile with a full width at half maximum (FWHM) of a few millimeters, and its size on the target plane can be controlled by adjusting the voltage of the last focusing electrode.

Working with Ps instead of positrons necessitates several adjustments to the beamline. Firstly, a Ps production system capable of continuously generating antiatoms and guiding them through the electrode system is required. Since Ps carries no net charge, it's imperative to devise a method for transporting and focusing its beam, while considering the finite lifetimes of antimatter's bound states. As mentioned, the chosen strategy involves producing negative positronium ions ($e^-e^+e^-$ bound-state, Ps^-) and incorporating a laser photodetachment stage to remove an electron, yielding the desired ortho-Ps atoms.

The $e^+ \rightarrow Ps^-$ conversion step also serves as a moderator: as positrons traverse the converter material, they thermalize, potentially forming Ps^-, thereby reducing beam kinetic energy and energy spread. Ps^- atoms are emitted from the opposite side of the target surface impacted by the beam. One of the possible converters is a 1 μm thick, sodium-coated tungsten foil, known for its high Ps^- production efficiencies. These ions are emitted perpendicular to the converter surface as cylindrical beam with a diameter of 1 mm with a kinetic energy of approximately 4 eV. A compact electrostatic system, comprising electrodes at varying potentials, is designed to accommodate the brief Ps^- lifetime. A simulation, crafted using SIMION® software, mapped the trajectory of Ps^- ions by computing their paths within defined electric fields. The electrode configuration, illustrated in Figure 1.3, includes a positron/Ps^-

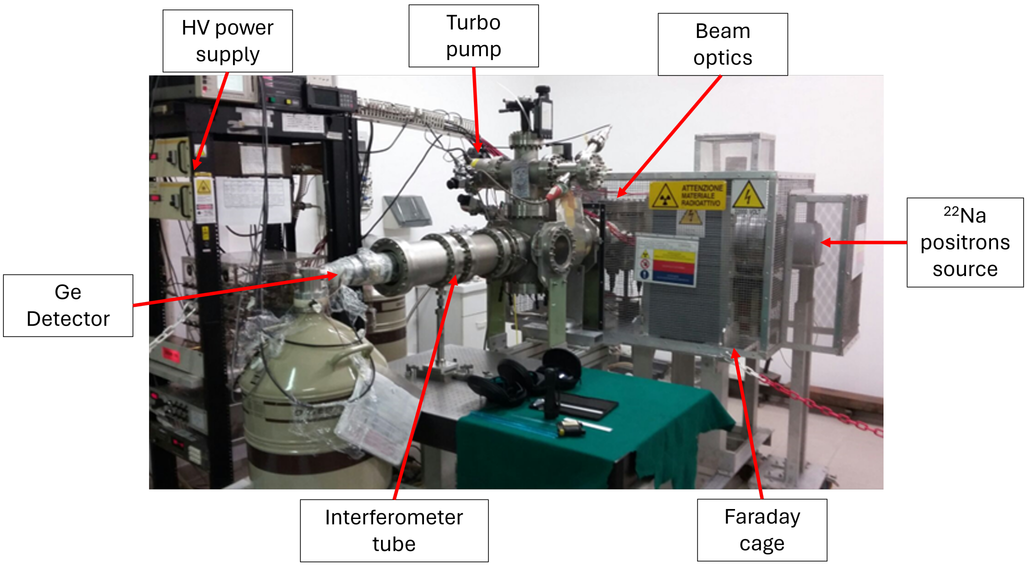

(a) Photograph of the QUPLAS positron accelerator at the Politecnico di Milano laboratory used for positron interferometry. The source is situated on the right-hand side of the image, inside the shielding, while the accelerating electrodes are in the vacuum tubes at the center. The interferometer here is a Talbot-Lau material gratings interferometer.

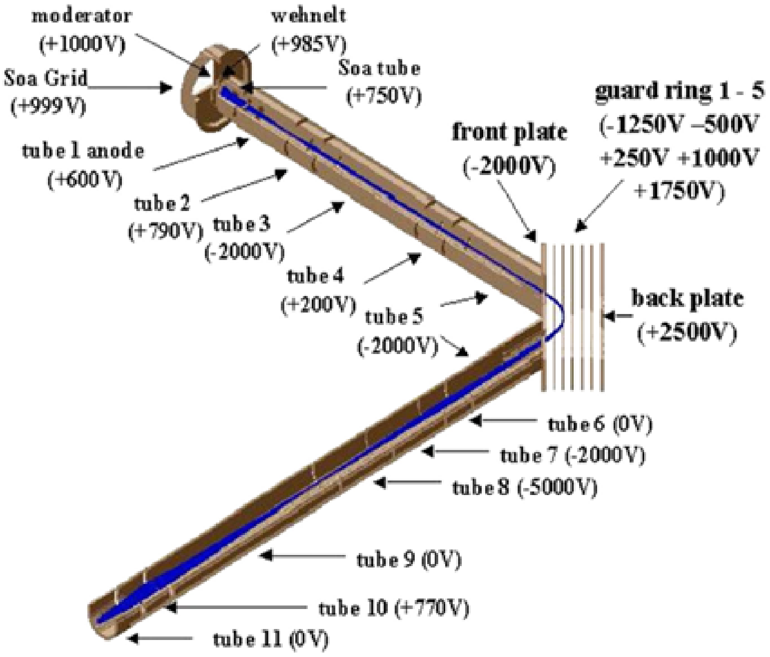

(b) Schematic of the electrode system for the focusing and transport of the positrons beam. The positrons emitted by the source located before the moderator cross the Soa Grid until they reach the bend made up of a series of electrodes with increasing potential [58]. The potentials are shown as examples.

Figure 1.2: Photograph and schematic of the QUPLAS positron accelerator.

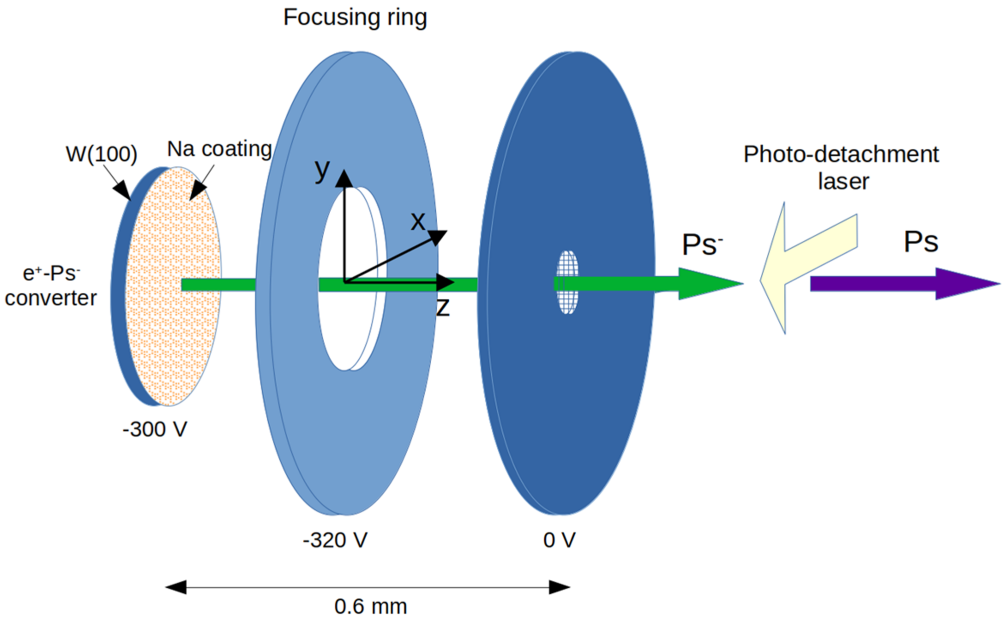

Figure 1.3: Schematic diagram of the Ps$^-$ beam acceleration and focusing system [49].

converter (monocrystalline Na-coated W sample), a focusing ring, and a grounded electrode featuring a central hole. The converter, modeled as a disk with a 2.5 mm radius and a potential of -300 V, repels Ps$^-$ ions towards the grounded electrode, reaching a kinetic energy of 300 eV. A 1 mm diameter hole in the last electrode allows the beam to pass through, closed with a conductive grounded grid to prevent electrostatic fields from extending beyond the system. The high transmission grid comprises metal wires (1 μm in diameter) spaced 50 μm apart. To enhance beam control and minimize divergence, a 2 mm diameter focusing ring, positioned 0.3 mm after the converter, applies a potential of -320 V to optimize beam divergence reduction. Maintaining a 0.3 mm distance between each component ensures adequate dielectric strength to prevent electric discharges.

As will be explained in Chapter 4, the gravitational measurement proposed in this thesis requires a high-intensity collimated Positronium beam. While a recently acquired ^{22}Na source can be utilized, providing approximately 10^8 e$^+$/s, a linear accelerator (LINAC) represents a better solution.

A commercial LINAC, pursued by the GBAR antimatter experiment at CERN [59], coupled with an electron-to-positron conversion technique, could generate an e$^+$ beam with a flux of around 10^{10} particles/s, offering better collimation and higher activity than the ^{22}Na source.

The BriXSinO Injector [60–62], situated at the LASA Laboratory in Segrate (Milano), stands as a more effective choice. This Energy Recovery LINAC (ERL) program is dedicated to showcasing high peak and average brightness beam generation, emphasizing energy sustainability.

In the quest to conduct interferometric measurements of Ps gravity over a year-long period (see Chapter 4), a brilliantly intense positron beam is imperative. The Milan BriXSinO facility proposes a superconducting LINAC operating at 92 MHz, with an average electron current of 2-5 mA and an acceleration energy of 10 MeV. This setup yields at least 5x10^{16} fast electrons per second, with a beam spot less than 1 mm and minimal divergence of about 50 μrad. By employing an effective positron moderator like tungsten meshes, a total conversion efficiency (cold e^+)/(hot e^-) of at least 10^{-5}-10^{-6} can be achieved. Under these technical specifications, the projected positron rate of the slow beam is estimated to be around 10^9-10^{10} positrons per second. The utilization of this LINAC is a realistic hypothesis, as the BriXSinO project is in an advanced stage of construction, and the QUPLAS research group is currently interacting with the BriXSinO personnel to explore how to collaborate and interface the two projects. Alternatively, a commercial LINAC similar to that of GBAR could be acquired, with which a flow of 10^5-10^6 Ps^-/s is estimated.

Chapter 2

Interferometry for gravity measurements

Atom interferometry is a versatile and powerful tool for precision measurements, in particular in gravitational physics [35, 63–68]. The light-pulse interferometer uses sequences of optical pulses to split, redirect and recombine matter waves by transferring photon momenta [69, 70] and emulating optical elements (e.g., mirrors and beam splitters) for coherent manipulation of atomic wave packets [71]. This type of interferometer has been proposed to improve sensitivity to inertial forces with large momentum transfer techniques using several light pulses to increase the space-time area of the interferometer [72].

A schematic of a basic Mach-Zehnder interferometer is shown in Figure 2.1. The horizontal axis of this graph represents time while the vertical one is the z coordinate. Two interferometric patterns are depicted: one influenced by gravitational acceleration acting along the negative z-axis and the other unaffected, indicated by the subscript 0. Three pulses of $\pi/2$, π, and $\pi/2$ intercept the atomic wavefunction at times 0, T, and 2T, respectively. The $\pi/2$ pulses split the wavefunction in two, acting as beam splitters, while the π pulse alters its internal state and momentum, serving as a mirror. Generically, the working principle of an interferometer for inertial sensing is based on the fact that an atom is split into a quantum superposition of states whose wavefunctions travel different paths and accumulate a different phases. To estimate this phase shift, it is possible to follow different strategies such as the perturbative approach [73] and the Feynman path integral approach [74, 75], which we will use in this discussion. The aim of this section is to develop a fairly general discussion of some of the figures of merit of an atomic interferometer, reserving the application on the case study of positronium for Chapter 4. In the application of the path integral and the rest of this treatment we will assume infinitesimally short light pulses but studies of the issue of the spatial extension of the pulses can be found in the literature [76]. Until otherwise specified, we will reduce the analysis to the one-dimensional case, considering laser pulses perfectly parallel to the acceleration

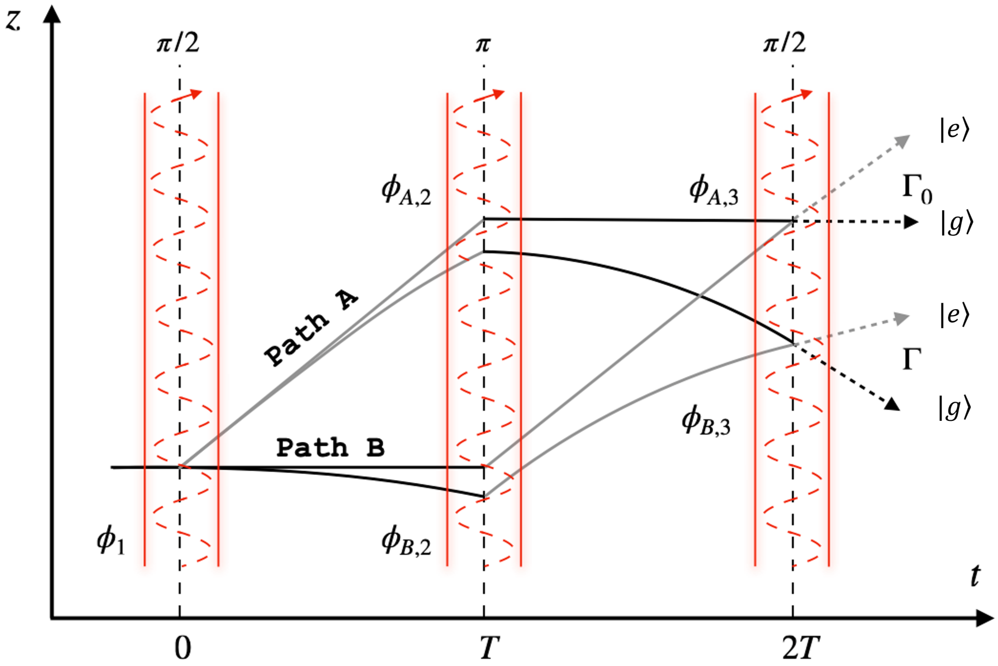

Figure 2.1: Schematic space-time diagram of a basic Mach-Zehnder intererometer with (path Γ) and without gravitational field effect (path Γ_0). The gravity acts along the negative z-axis which indicates the wavefunctions position. Laser pulses at instants 0, T and 2T behave similarly to beam splitters and mirrors of a light interferometer, splitting and reflecting the wavefunctions (quantum superposition) of an atom passing through them.

of gravity.

The fundamental concept of the path integral method lies in considering the path travelled by classical particles moving from a starting point (z_a,t_a) to an endpoint (z_b,t_b). Between these two points, there exists an infinite number of possible space-time paths (Γ, Γ′,..) connecting them, where each path is described by a function z(t) satisfying the conditions $z(t_a) = z_a$ and $z(t_b) = z_b$. Among all these potential paths, there is one that is actually followed by the particle, and this path can be determined using the system's Lagrangian, $L(z, \dot{z})$, which is the difference between its kinetic and potential energy.

The actual trajectory taken by a classical particle corresponds to the path for which the action $S_\Gamma(z_b, t_b; z_a, t_a)$ is extremal. The action is defined as the integral of the Lagrangian over the specific path Γ.

$$S_\Gamma = \int_{t_a}^{t_b} L(z, \dot{z})\, dt \tag{2.1}$$

By varying the path and evaluating the action for each variation, one can find the path that minimizes or maximizes the action, which in turn determines the trajectory of the particle according to the principle of least action. We will denote by Γ_{cl} the actual classical path, for which the action is extremal, and by S_{cl} the corresponding value of the action.

The starting point of the path integral method involves defining a quantum propagator K which denotes the amplitude for the particle to arrive at point (z_b,t_b) given that it starts from point (z_a,t_a). In quantum mechanics, the propagator is defined by:

$$K(z_b, t_b; z_a, t_a) = \langle z_b| U(t_b, t_a) |z_a\rangle \tag{2.2}$$

where U(t_b,t_a) is the evolution operator which evolves the state of a quantum system from t_a to t_b, $|\psi(t_b)\rangle = U(t_b, t_a) |\psi(t_a)\rangle$. This allows us to define the wavefunction at the final position as a function of the propagator:

$$\begin{aligned}\Psi(z_b, t_b) &= \langle z_b| U(t_b, t_a) |\Psi(z_a)\rangle \\ &= \int K(z_b, t_b; z_a, t_a)\Psi(z_a, t_a)\, dz_a\end{aligned} \tag{2.3}$$

From Feynman's formulation we define the quantum propagator as a sum of contributions from all possible paths connecting the initial and final points [74, 77]. The modulus of each contribution is independent of the path Γ but the phase factor equals $S_\Gamma/\hbar$:

$$K(z_b, t_b; z_a, t_a) = \int_a^b Dz(t) e^{iS_\Gamma/\hbar} \tag{2.4}$$

where Dz(t) represents an infinitesimal change in position along the path over time t and indicates an integration over all possible z(t) trajectories that the system could follow, allowing the entire spectrum of possible evolutions of the system over time to be considered. In the classical limit where $S_\Gamma \gg \hbar$, the phase $S_\Gamma/\hbar$ varies rapidly among neighboring paths Γ, leading to destructive interference. However, along the classical path, the action is extremal, resulting in constructive interference. Consequently, only paths near the classical trajectory significantly contribute to the integral 2.4. Equations 2.3 and 2.4 show an important result, namely that the phase shift of a wavefunction propagating in space and time is proportional to the action corresponding to the path travelled:

$$\Psi(z_b, t_b) \propto \Psi(z_a, t_a) \exp(iS_{\mathrm{cl}}/\hbar) \tag{2.5}$$

In the limit of a large action, the integral in 2.4 simplifies and the wavefunction is

$$\Psi(z_b, t_b) = \Psi(z_a, t_a) \exp(iS_{\mathrm{cl}}/\hbar) \tag{2.6}$$

The same result can be obtained by applying the perturbative method to the Lagrangian of the particle in free motion [75]. Since the action is a function of the Lagrangian, it is possible to consider the potentials to which the particle is subjected during propagation, such as the gravitational one.

It is worth mentioning the Van Vleck formula, which establishes the equivalence between the path integral and a regular integral for potentials that are at most quadratic in the coordinates. The Van Vleck formula provides a connection between the Green's function associated with the propagator operator and the phase accumulated along classical paths, allowing the quantum propagator to be expressed as a sum over all classical paths weighted by a prefactor that depends on the second derivative of the action with respect to the coordinates:

$$K(z, z_a, t) \propto \sum_{\text{cl}} \left(\sqrt{\left| \frac{\partial^2 S_{\text{cl}}}{\partial z \partial z_a} \right|} \exp(iS_{\text{cl}}(z, z_a, t)/\hbar) \right)$$

This is particularly useful in cases where the potential has a quadratic dependence, facilitating the comparison between the path integral formalism and more traditional approaches based on the use of the propagator operator.

Since the Hamiltonian is defined as the sum of kinetic and potential energy, a relationship exists between H and L and is given by:

$$H = p\dot{z} - L \tag{2.7}$$

Keeping the initial spacetime point fixed, the variation in the classical action due to a change in the final spacetime point (z, t) is

$$dS_{\text{cl}} = \frac{\partial S_{\text{cl}}}{\partial z} dz + \frac{\partial S_{\text{cl}}}{\partial t} dt = pdz - Hdt \tag{2.8}$$

which gives an expression of the classical action as a function of the Hamiltonian:

$$S_{\text{cl}} = \int_{\Gamma_{\text{cl}}} (pdz - Hdt) \tag{2.9}$$

This also justifies the use of the Hamiltonian in the next sections. If we plug this equation into 2.6 we obtain the typical equation which describes the external motion of a plane wavefunction:

$$\Psi(z_b, t_b) = e^{i \int_{\Gamma_{\text{cl}}} (kdz - \omega dt)} \Psi(z_a, t_a) \tag{2.10}$$

2.1 The phase shift in an atom interferometer

Before studying the effect of the gravitational field, it is necessary to contextualise this analysis to the case of an atom interacting with an interferometer. In Figure 2.2 there is a representation of the effects of a resonant light pulse with a single-photon transition of an atom passing through it: when the atom absorbs a photon it is excited and acquires a laser momentum $\hbar k_{\text{L}}$ along the laser propagation direction;

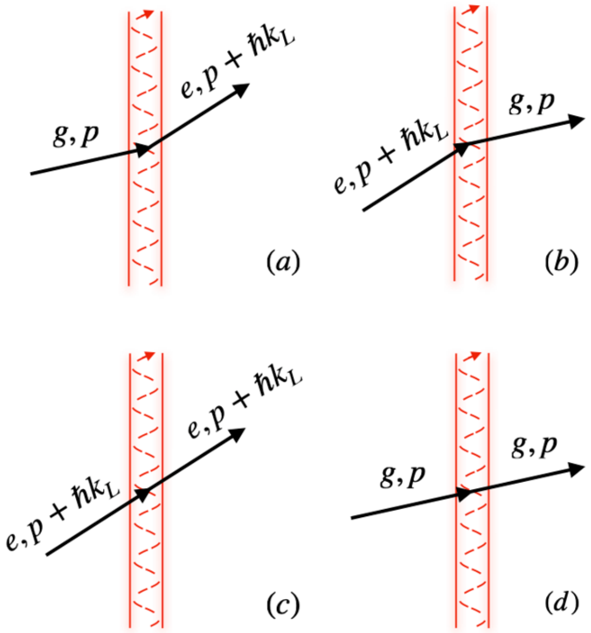

Figure 2.2: Schematisation of the atom-light interaction in 4 basic cases. a) A ground state absorbs a photon and changes its internal state and momentum along the direction of light propagation. b) Inversely to a), an atom in an excited state returns to the ground state by stimulated emission, losing a momentum in the direction of the laser. In c) and d), the atom passes through the laser beam without interacting with the light, which therefore does not alter its state.

when the atom de-excites it also loses a photon by stimulated emission and a laser momentum along the laser projection direction or, equivalently, acquires one in the opposite direction. Note that this representation may be different for interferometers exploiting multi-photon transitions, such as in the case of Raman or Bragg pulses. Whenever an atom interacts with a light pulse, causing an excitation or de-excitation action, it undergoes a phase shift represented by

$$\Delta\phi^{\Gamma}_{L,i} = \pm(k_{\mathrm{L}} z^{\Gamma}_{i} - \omega_{\mathrm{L}} t_i - \phi_{L_i}) \tag{2.11}$$

where the sign depends on the nature of the interaction (excitation or de-excitation). $\mathrm{k_L}$ and ω_{L} represent the wave vector and frequency of the incident light pulse, while ϕ_{L} is the laser phase. In the equation, the subscript Γ represents the interferometric path (Γ=A, B) while i indicates the interferometric sequence (i=1, 2, 3). z_i and t_i respectively represent the position and time at which the atomic interaction with the light pulse occurs, determining the location and instant of the interaction: $\mathrm{t_1}$=0, $\mathrm{t_2}$=T, $\mathrm{t_3}$=2T. Based on what has been discussed so far, the total phase of an atom passing through the interferometer is determined by the phase shift due to propagation along the interferometric trajectories and that generated by interaction with laser pulses.

$$\Delta\phi^{\Gamma} = \Delta\phi^{\Gamma}_{\mathrm{p}} + \Delta\phi^{\Gamma}_{\mathrm{L}} \tag{2.12}$$

Each branch has its phase, and we are interested in determining the phase difference between the two branches, which determines the type of interference on the final pulse.

$$\Delta\phi_{\text{tot}} = \Delta\phi^{\text{B}} - \Delta\phi^{\text{A}} \tag{2.13}$$

Another contribution could be made by the free evolution of wavefunctions in different internal states, but we can already state that this is null by observing that the wavepacket spend the same amount of time in the two internal states. The propagation phase shift between i and $i+1$ can be defined using the results of the previous section:

$$\Delta\phi^{\Gamma}_{\text{p}_{(i,i+1)}} = S^{\Gamma}_{\text{cl}}(z_{i+1}, t_{i+1}; z_i, t_i) = \int_{t_i}^{t_{i+1}} L(z,\dot{z})\,dt \tag{2.14}$$

This equation is valid in general and we can use it to study the case of an atom moving in a constant gravitational field:

$$L(z,\dot{z}) = \frac{1}{2}m\dot{z}^2 - mgz \tag{2.15}$$

where m is the mass of the atom. Calculating the integral 2.14 and considering the relationship between the gravity-influenced pattern and the undeflected parallelogram

$$z_i^{\Gamma} = z_i^{\Gamma_0} - \frac{1}{2}gt_i^2 \tag{2.16}$$

we obtain that the phase shift due to propagation is zero

$$\begin{aligned}\Delta\phi_{\text{p}} &= S^{\text{B}}_{\text{cl}}(z_2, t_2; z_1, t_1) + S^{\text{B}}_{\text{cl}}(z_3, t_3; z_2, t_2) \\ &\quad - \left(S^{\text{A}}_{\text{cl}}(z_2, t_2; z_1, t_1) + S^{\text{A}}_{\text{cl}}(z_3, t_3; z_2, t_2)\right) = 0\end{aligned} \tag{2.17}$$

In this frame, the total phase shift is therefore only determined by the phase shift of the lasers. Given that for path B we have $\Delta\phi^{\text{B}}_{L_1} = \Delta\phi^{\text{B}}_{L_3} = 0$ while $\Delta\phi^{\text{B}}_{L_2} = -(k_{\text{L}}z_2^{\text{B}} - \omega_{\text{L}}t_2 - \phi_{L_2})$, we obtain

$$\Delta\phi_{\text{tot}} = \Delta\phi^{\text{B}}_{\text{L}} - \Delta\phi^{\text{A}}_{\text{L}} = k_{\text{L}}gT^2 + \phi_{\text{L}_1} - 2\phi_{\text{L}_2} + \phi_{\text{L}_3} \tag{2.18}$$

which is sensitive to the gravity acceleration g. Note that the phase difference remains unaffected by the initial velocity, thus remaining constant even after averaging over the velocity spread of the atomic beam. However, it's important to note that the velocity spread can significantly influence the probability of atom-laser interaction, thereby impacting the measurement in various other ways.

There is another phase factor that needs to be considered: in Figure 2.3 interferometric patterns with a spatial separation on the last pulse $\pi/2$ that is in general different from zero are shown. This spatial discrepancy gives rise to a phase sepa-

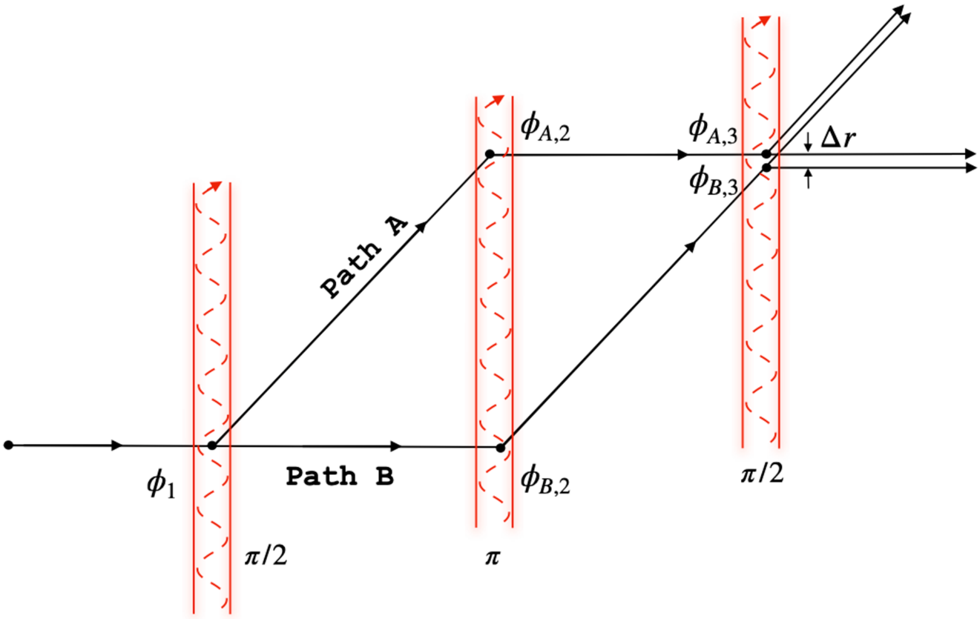

Figure 2.3: Basic schematic of the Mach-Zehnder interferometer with spatial mismatch Δr of wavefunctions at the last laser pulse

ration $\Delta\phi_{\mathrm{s}}$ [78]. The de Broglie waves from the two wave packets interfere with a differential phase:

$$\Delta\phi_{\mathrm{s}} = \frac{p \cdot \Delta r}{\hbar} \tag{2.19}$$

where p is the momentum of the atom, and Δr is the spatial separation of the two wave packets.

Before the last $\pi/2$-pulse, let's consider the wave packet in path (A,2) moving at velocity v_{g}, and the wave packet in path (B,2) moving at velocity v_{e}, with their separation being Δr (pointing from path A to path B). The pulses have a wave vector k_{eff}, which, as we shall see, has a different definition depending on the type of interferometer. In the example illustrated in Figure 2.3 with single-photon transitions we consider $\mathrm{k}_{\mathrm{eff}} = k = 2\pi/\lambda_{\mathrm{L}}$, with λ_{L} wavelength of the laser. Thus the last $\pi/2$-pulse gives a recoil kick of $v_{\mathrm{r}} = \hbar k_{\mathrm{eff}}/m$. Due to the separation of the two wave packets, $\phi_{\mathrm{B,3}}$ and $\phi_{\mathrm{A,2}}$ are not the same and are related by:

$$\phi_{\mathrm{B,3}} = \phi_{\mathrm{A,3}} + k_{\mathrm{eff}} \cdot \Delta r \tag{2.20}$$

The velocities of the two wave packets in the ground state after the last $\pi/2$-pulse are v_{g} and $(v_{\mathrm{e}} - v_r)$ (ideally, these two velocities are exactly the same). The separation phase of the ground state is calculated using the average speed of these two velocities:

$$\phi_{\mathrm{g,s}} = \frac{m(v_{\mathrm{g}} + v_{\mathrm{e}} - v_r)\Delta r}{2\hbar} \tag{2.21}$$

Similarly,

$$\phi_{\mathrm{e,s}} = \frac{m(v_{\mathrm{g}} + v_{\mathrm{e}} + v_r)\Delta r}{2\hbar} \tag{2.22}$$

The excited state and ground state have different laser phase and separation phase contributions, but it's easy to prove that the sum of these two is exactly the same:

$$\phi_{\mathrm{g,s}} + \phi_{\mathrm{B},3} = \phi_{\mathrm{e,s}} + \phi_{\mathrm{A},3} \tag{2.23}$$

As a result, the total phase of the two states is equal and p of 2.19 can be substituted by $p = \hbar k_{\mathrm{eff}} : \Delta\phi_{\mathrm{s}} = k_{\mathrm{eff}} \cdot \Delta r$.

In discussing phase shifts in an atomic interferometer, it's crucial to understand that there isn't a distinct physical quantity representing the laser phase or path phase. Instead, the only observable quantity is the total phase. By transitioning all calculations into a moving frame, we discover that both the path phase and separation phase differ, rendering them essentially arbitrary and devoid of physical significance. However, the sum of these two phases remains consistent with that in the laboratory frame, with special relativity ensuring the laser phase remains unchanged under Lorentz transformations. Consequently, the total phase, or the ratio of population between two states, remains invariant under inertial frame transformations, as expected.

2.1.1 Other Lagrangians

Other factors influencing the motion of the atom through the interferometer can be considered and introduced into the phase shift calculation by modifying the Lagrangian 2.15. One can for example consider the variation of the gravitational field with respect to the z-coordinate by inserting a linear gradient γ:

$$L(z, \dot{z}) = \frac{1}{2}m\dot{z}^2 - mgz + m\gamma z^2/2 \tag{2.24}$$

By calculating the action again through the equation 2.1, the phase difference between path B and A and expressing it as a series of powers in γ we obtain a correction on the acceleration of gravity due to the gradient [64]:

$$\begin{aligned} g' =& g_0 + g_1 + g_2 = \\ g + \gamma\left(\frac{7}{12}gT^2 - \bar{v_0}T - z_0\right) &+ \gamma^2T^2\left(\frac{31}{360}gT^2 - \frac{1}{4}\bar{v_0}T - \frac{7}{12}z_0 - \frac{1}{2}v_r(T + T_{\mathrm{det}})\right) \end{aligned} \tag{2.25}$$

Where we have stated only the first two terms of the expansion. In the equation z$_0$ is the initial coordinate of the interferometric sequence (z$_0$=0 for us), $\bar{v_0}$ is the average velocity after the fist pulse equal to $\bar{v_0} = v_0 + v_{r,\mathrm{eff}}/2$, with v_0 initial velocity of the atom, $v_{r,\mathrm{eff}} = \hbar k_{\mathrm{eff}}/m$ and T_{det} is the time delay between the last pulse and the detector. The corresponding phase shift is:

$$\Delta\phi_\gamma = k_{\mathrm{eff}}(g_1 + g_2)T^2 \tag{2.26}$$

Another variation to the Lagrangian considers rotations by transforming the laboratory into a rotating frame. To do this we have to break the one-dimensionality and substitute the velocity $\mathbf{v}' = \mathbf{v_0} + \mathbf{\Omega} \times \mathbf{r}$, which contains the angular velocity Ω, into the equation 2.15 [37]:

$$L'(\mathbf{r}', \mathbf{v}') = \frac{1}{2}m\left[\mathbf{v} + (\mathbf{\Omega} \times \mathbf{r})\right]^2 = \frac{1}{2}m\mathbf{v}^2 + m\mathbf{\Omega} \cdot (\mathbf{r} \times \mathbf{v}) + \frac{1}{2}m(\mathbf{\Omega} \times \mathbf{r})^2 \tag{2.27}$$

For $\Omega\Delta t \ll 1$, where Δt id the transit time of the atoms through the interferometer, the rotation can be considered a small perturbation:

$$L' = L_0 + L_1 = \frac{1}{2}m\mathbf{v}^2 + m\mathbf{\Omega} \cdot (\mathbf{r} \times \mathbf{v}) \tag{2.28}$$

where only the term to the first order in $\mathbf{\Omega}$ was kept. Thus, the phase difference between the two paths is then given by the action of the perturbing Lagrangian integrated along the unperturbed (straight-line) paths:

$$\Delta\phi_{L_1}^{\Gamma_0} = \frac{1}{\hbar}\int_{\Gamma_0} L_1\, dt = \frac{m\mathbf{\Omega}}{\hbar}\int_{\Gamma_0} [\mathbf{r}(t) \times \mathbf{v}(t)]\, dt \tag{2.29}$$

By substituting $\mathbf{v}(t) = d\mathbf{r}(t)/dt$ or $\mathbf{r}(t) = t \cdot \mathbf{k}_{\mathrm{eff}}\hbar/m$ we obtain respectively:

$$\Delta\phi_{\mathrm{c}} = \frac{2m\mathbf{\Omega}}{\hbar}A_0 = -2T^2\mathbf{v} \cdot (\mathbf{k}_{\mathrm{eff}} \times \mathbf{\Omega}) \tag{2.30}$$

where A_0 is the total area enclosed by the interferometer. Applying the last form of the result to the case of the Earth where, in the reference frame $\hat{\mathbf{u}} = (\hat{u}_{\mathrm{we}}, \hat{u}_{\mathrm{n}}, \hat{u}_{\mathrm{up}})$ indicating the West-Est, North and upward components, $\mathbf{\Omega} = (0, \Omega\cos\theta_{\mathrm{l}}, \Omega\sin\theta_{\mathrm{l}})$, with θ_{l} latitude, we have that

$$\Delta\phi_{\mathrm{c}} = -2T^2 v_{\mathrm{we}} k_{\mathrm{eff,up}} \Omega\cos\theta_{\mathrm{l}} \tag{2.31}$$

2.2 Probability amplitudes and measurement

As anticipated, one wants to exploit the phenomenon of interference between atomic wavefunctions to determine phase shift and thus gravity acclection. This is equivalent to turning phase variations into amplitude variations at the output of the interferometer, similarly to a light Mach-Zehnder. In this section we want to determine the probability of finding the atom in one of the two interferometric states and the relationship between the number of atoms exiting the output ports and the interferometric phase shift.

Let's assume we are dealing with a two-level system and describe the atom in a basis representing a ground state $|\mathrm{g}\rangle$ and an excited state $|\mathrm{e}\rangle$. As mentioned in Section 2.1, each change of internal state is associated with a change of momentum state. To model this interaction, we start with the definition of an electric field

$$\mathbf{E} = \mathbf{E}_0 \cos\left(\mathbf{k}_\mathrm{L}\mathbf{x} - \omega_\mathrm{L} t + \phi\right) = \frac{\hat{\mathbf{e}} E_0}{2}\left(e^{i(\mathbf{k}_\mathrm{L}\mathbf{x}-\omega_\mathrm{L}t+\phi)} + e^{-i(\mathbf{k}_\mathrm{L}\mathbf{x}-\omega_\mathrm{L}t+\phi)}\right) \tag{2.32}$$

The action of the field on a momentum state $|\mathbf{p}\rangle$ can be described by

$$e^{\pm i\mathbf{k}_\mathrm{L}} = \int d^3\mathbf{p} e^{\pm i\mathbf{k}_\mathrm{L}\mathbf{x}} |\mathbf{p}\rangle\langle\mathbf{p}| = \int d^3\mathbf{p}\, |\mathbf{p} \pm \hbar\mathbf{k}_\mathrm{L}\rangle\langle\mathbf{p}| \tag{2.33}$$

which indicates the change in the total momentum of the atom following the stimulated absorption or emission of a photon. The change of internal state and momentum state occur simultaneously and we can therefore summarise the atomic states of the interferometer in 2.1 with the state vector $|\mathrm{g},\mathbf{p}\rangle$ and $|\mathrm{e},\mathbf{p}+\hbar\mathbf{k}_\mathrm{L}\rangle$. However, we often omit the momentum indices for cleaner notation, identifying the atomic state only with the internal state. We define the wavefunction at time t as

$$|\psi\rangle = c_{\mathrm{g,p}} e^{-i\omega_{\mathrm{g,p}}t} |\mathrm{g},\mathbf{p}\rangle + c_{\mathrm{e,p}+\hbar\mathrm{k}_\mathrm{L}} e^{-i(\omega_{\mathrm{e,p}+\hbar\mathrm{k}_\mathrm{L}})t} |\mathrm{e},\mathbf{p}+\hbar\mathbf{k}_\mathrm{L}\rangle \tag{2.34}$$

and a Hamiltonian given by the sum

$$\hat{H} = \hat{H}_0 + \hat{H}_\mathrm{L} = \frac{\hat{\mathbf{p}}^2}{2m} + \hbar\omega_\mathrm{g} |\mathrm{g}\rangle\langle\mathrm{g}| + \hbar\omega_\mathrm{e} |\mathrm{e}\rangle\langle\mathrm{e}| - \mathbf{d}\cdot\mathbf{E} \tag{2.35}$$

where $\hat{H}_0$ is the Hamiltonian for the internal degrees of freedom and $\hat{H}_\mathrm{L}$ describes the interaction between atom and electric field. In these equations $c_{\alpha,l}$ are the slow varying time dependent probability amplitudes of the states $|\alpha,\mathbf{l}\rangle$, $\mathbf{d}$ is the electric dipole moment and

$$\omega_{\alpha,l} = \omega_\alpha + \frac{|\mathbf{l}|^2}{2\hbar m} \tag{2.36}$$

with ω_α optical frequency of the atomic internal state. We can define the Rabi frequency as $\Omega_\mathrm{eg} = \frac{-\langle\mathbf{e}|\mathbf{d}\cdot\mathbf{E}_0|\mathbf{g}\rangle}{\hbar}$ and the detuning

$$\delta = \omega_\mathrm{L} - (\omega_{\mathrm{e,p}+\hbar\mathrm{k}_\mathrm{L}} - \omega_{\mathrm{g,p}}) = \omega_\mathrm{L} - \left(\omega_e - \omega_g + \frac{\hbar|\mathbf{k}_\mathrm{L}|^2}{2m} + \mathbf{v}\cdot\mathbf{k}_\mathrm{L}\right) \tag{2.37}$$

where the term $\hbar|\mathbf{k}_\mathrm{L}|^2/2m$ corresponds to the photon-recoil shift and $\mathbf{v}\cdot\mathbf{k}_\mathrm{L}$ corresponds to the Doppler shift given by a non zero initial velocity of the atom in the laser direction. If $\Omega_\mathrm{eg} \ll \omega_\mathrm{e}, \omega_\mathrm{g}$ we can solve the Schrödinger equation in the rotating wave approximation (neglecting the $e^{i(\omega_{\mathrm{eg}}+\omega_{\mathrm{L}})}$, with $\omega_{\mathrm{eg}} = \omega_{\mathrm{e}} - \omega_{\mathrm{g}}$) and obtain the following system:

$$\begin{cases} i\dot{c}_{\mathrm{e}} = \frac{\Omega_{\mathrm{eg}}}{2} c_{\mathrm{g}} \mathrm{e}^{-i(\delta t+\phi)} \\ i\dot{c}_{\mathrm{g}} = \frac{\Omega^*_{\mathrm{eg}}}{2} c_{\mathrm{e}} \mathrm{e}^{i(\delta t+\phi)} \end{cases} \tag{2.38}$$

This system is used to determine the evolution of the probability amplitudes of the atomic states passing through the interferometer and is the starting point of the ineterferometer simulation that we will see in chapter 4. For a constant Ω_{eg} is convenient to refer to a frame rotating about the **z**-axis (the same of Figure 2.1) with frequency δ. The Hamiltonian in the rotating frame is give by [79]

$$\hat{H}_{\mathrm{R}} = \left\{ \frac{\hat{\mathbf{p}}^2}{2m} + \frac{\hbar}{2} \begin{bmatrix} -\delta & \Omega_{\mathrm{eg}} e^{i(\mathbf{k}_{\mathrm{L}}\mathbf{x}-\phi)} \\ \Omega^*_{\mathrm{eg}} e^{-i(\mathbf{k}_{\mathrm{L}}\mathbf{x}-\phi)} & \delta \end{bmatrix} \right\} \tag{2.39}$$

By solving the eigenvalue problem, it is possible to determine eigenvalues and eigenstates of the rotating Hamiltonian [80] and obtain the following system:

$$\begin{cases} i\dot{c}_{\mathrm{e}} = \frac{\delta}{2} c_{\mathrm{e}} + \frac{\Omega_{\mathrm{eg}}}{2} c_{\mathrm{g}} \mathrm{e}^{-i\phi} \\ i\dot{c}_{\mathrm{g}} = \frac{\Omega^*_{\mathrm{eg}}}{2} c_{\mathrm{e}} \mathrm{e}^{i\phi} - \frac{\delta}{2} c_{\mathrm{g}} \end{cases} \tag{2.40}$$

What emerges is the presence of a shift in energy levels when the lasers are detuned from the transition. For example, the ground level shift is given by $E_{\mathrm{g}\pm} = \hbar \left[\omega_{\mathrm{g}} + \frac{\delta}{2} \pm \frac{1}{2} \sqrt{\delta^2 + \left|\Omega^2_{\mathrm{eg}}\right|} \right]$ where the sign depends on the sign of δ: for large positive detuning $E_{\mathrm{g}-} \simeq \left(\omega_{\mathrm{g}} - \frac{1}{4} \frac{|\Omega_{\mathrm{e,g}}|^2}{|\delta|} \right)$, while for a large negative detuning $E_{\mathrm{g}+} \simeq \left(\omega_{\mathrm{g}} + \frac{1}{4} \frac{|\Omega_{\mathrm{e,g}}|^2}{|\delta|} \right)$.

We are now interested in understanding how the original wavefunction evolves in the non-rotating frame. To do this, we need to rotate the initial wavefunction by multiplying it by the operator $D(\mathbf{x}, -\delta t_0) = e^{i\sigma_{\mathrm{z}}\delta t_0/2}$, where σ_{z} is the Pauli spin matrix, project it onto the eigenstates of $\hat{H}_R$, and then anti-rotate it with $D^\dagger$. The wavefunction evolution after an interaction time equal to τ, $|\psi(t_0+\tau)\rangle = \hat{U}(t_0 + \tau, t_0) |\psi(t_0)\rangle = D^\dagger(\mathbf{x}, -\delta(t_0+\tau)) \hat{U}_{\mathrm{R}}(t_0+\tau, t_0) |\psi(t_0)\rangle$ with $\hat{U}(t_0+\tau, t_0)$ given by:

$$e^{-i\sigma_{\mathrm{z}}\delta\tau/2} \cdot \begin{bmatrix} \cos\left(\frac{\Omega_{\mathrm{r}}\tau}{2}\right) - i\cos\theta \sin\left(\frac{\Omega_{\mathrm{r}}\tau}{2}\right) & e^{-i(\delta t_0+\phi)} \left[-i\sin\theta \sin\left(\frac{\Omega_{\mathrm{r}}\tau}{2}\right)\right] \\ e^{i(\delta t_0+\phi)} \left[-i\sin\theta \sin\left(\frac{\Omega_{\mathrm{r}}\tau}{2}\right)\right] & \cos\left(\frac{\Omega_{\mathrm{r}}\tau}{2}\right) + i\cos\theta \sin\left(\frac{\Omega_{\mathrm{r}}\tau}{2}\right) \end{bmatrix} \tag{2.41}$$

where $\Omega_{\mathrm{r}} = \sqrt{|\Omega_{\mathrm{eg}}|^2 + \delta^2}$ is the off-resonant Rabi frequency and θ is defined by the following relations:

$$\sin\theta = \Omega_{\mathrm{eg}}/\Omega_{\mathrm{r}},\ \cos\theta = \delta/\Omega_{\mathrm{r}},\ 0 \leq \theta \leq \pi.$$

We can derive the probability amplitude of the excited state assuming $t_0 = 0, c_\mathrm{e}(t_0) = 0, c_\mathrm{g}(t_0) = 1$. In the limit of large detuning ($\theta \simeq 0$, $\sin\theta \simeq \theta$) the probability of finding the atom in $|\mathrm{e}\rangle$ is

$$|c_\mathrm{e}(\tau)|^2 = \left(\frac{\Omega_{eg}}{\Omega_r}\right)^2 \sin^2\left(\frac{\Omega_\mathrm{r}\tau}{2}\right) \tag{2.42}$$

while if $0 < |\delta| \ll \Omega_\mathrm{eg}$, $\sin\theta \simeq 1$,

$$|c_\mathrm{e}(\tau)|^2 = \frac{1}{2}\left[1 - \cos(\Omega_\mathrm{r}\tau)\right] \tag{2.43}$$

These equations tell us that by properly setting the pulse duration or the electric field amplitude we can decide the probability of transition from one state to the other and thus obtain the pulses $\pi, \pi/2$, or other types, just by setting $\Omega_\mathrm{r}\tau \simeq \Omega_\mathrm{eg}\tau = \pi, \pi/2$ etc. For a higher δ the probability oscillates faster and can not be unitary. The probability amplitudes for generic $c_\mathrm{g}, c_\mathrm{e}$ and $\delta \ll \Omega_\mathrm{eg}$, for π and $\pi/2$ pulses are reported in table 2.1.

	$\pi/2$	π
$c_\mathrm{g}(t_0+\tau)$	$e^{i\delta\tau/2}\left[-ic_\mathrm{e}(t_0)e^{i(\delta t_0+\phi)} + c_\mathrm{g}(t_0)\right]/\sqrt{2}$	$-ic_\mathrm{e}(t_0)e^{i\delta\tau/2}e^{i(\delta t_0+\phi)}$
$c_\mathrm{e}(t_0+\tau)$	$e^{-i\delta\tau/2}\left[c_\mathrm{e}(t_0) - ic_\mathrm{g}(t_0)e^{i(\delta t_0+\phi)}\right]/\sqrt{2}$	$-ic_\mathrm{g}(t_0)e^{-i\delta\tau/2}e^{-i(\delta t_0+\phi)}$

Table 2.1: Probability amplitudes of states $|g\rangle$ and $|e\rangle$ for single-photon transitions assuming $\delta \ll \Omega_\mathrm{eg}$.

At this point we can retrace the interferometer of Figure 2.1 computing the amplitudes after each interaction. Assuming that the pulses have the same Rabi frquency and the pulse duration of the $\pi/2$ is $\tau/2$, we obtain the final probability amplitude of the excited state:

$$|c_{\mathrm{e,p}+\hbar\mathrm{k_L}}(2T+2\tau)|^2 = \frac{1}{2}\left[1 - \cos(\Delta\phi - \delta\tau/2)\right] \tag{2.44}$$

where $\Delta\phi = \phi_{\mathrm{L}_1}(0) - 2\phi_{\mathrm{L}_2}(T) + \phi_{\mathrm{L}_3}(2T)$. This phase shift can be related to the gravity acceleration by considering the motion of the atom in the gravity field and the corresponding time dependent phase shift:

$$\phi_{\mathrm{L}_i}(t) = \phi_{\mathrm{L}_i} + \mathbf{k}_\mathrm{L} z(t_i)\hat{\mathbf{z}} = \phi_{\mathrm{L}_i} + \mathbf{k}_\mathrm{L}\left(z(t_1) + \dot{z}t_i - \frac{1}{2}gt_i^2\right)\hat{\mathbf{z}} \tag{2.45}$$

which gives $\Delta\phi = \mathbf{k}_\mathrm{L} gT^2\hat{\mathbf{z}} + \phi_{\mathrm{L}_1} - 2\phi_{\mathrm{L}_2} + \phi_{\mathrm{L}_3}$, as in equation 2.18. This important result lets us link the probability of finding an atom in one of the two states to the phase shift of the atomic wavefunction, which is in turn connected to the gravity acceleration. This means that by counting the number of atoms leaving one of the interferometer's output ports, for a large enough number of atoms it is possible to estimate the gravitational acceleration. Moreover, we can modulate the probability to find the atom in the ground or excited state by modulating the laser phases.

2.2.1 Bragg interferometer

The sensitivity of atom interferometers can be significantly improved by maximizing the momentum differences between their paths. For instance, in Sagnac-effect gyroscopes, sensitivity is directly proportional to the area enclosed by the two interferometer arms (as shown in Equation 2.30). Consequently, larger momentum differences result in larger enclosed areas, leading to greater sensitivity; similarly, in gravimeters, sensitivity increases linearly with the separation between wave packets, assuming a fixed time duration, and a larger momentum recoil translates to higher sensitivity. Such interferometers are often referred to as large area or *Large Momentum Transfer* (LMT) interferometers.

Multi-photon transitions offer an effective approach for implementing atom interferometers, where the two states differ in momentum without internal excitation. These processes are commonly known as Bragg diffraction, drawing an analogy to the scattering of X-rays and neutrons off crystals.

In atomic Bragg diffraction, an optical lattice formed by counterpropagating laser fields serves as the diffracting crystal planes, with atomic matter-waves acting akin to beams of X-rays. Described in terms of combined cycles of absorption and stimulated emission, Bragg diffraction transfers pairs of photon momenta.

Generally speaking, in this technique, two laser pulses with frequencies ω_1 and ω_2, detuned from the atomic resonance, interact with an atom. The frequency difference is chosen to be an even multiple of the recoil frequency $\omega_r = \hbar k_{\mathrm{L}}^2/2m$. This interaction enables transitions between states, with the atom absorbing a photon from frequency ω_1 and de-exciting via stimulated emission into light with frequency ω_2, resulting in a net energy gain $\propto \hbar\omega_r$. This gained energy alters the atom's kinetic energy without affecting its internal state, leading to observed atomic motion in one direction.

Bragg pulses, similarly to Raman pulses [69], exploit an intermediate energy level to facilitate transitions to a third state. However, strong coupling with the intermediate level can result in significant losses due to spontaneous emission. Hence, it's essential for the laser to be detuned by a certain amount Δ relative to the atomic transition between the ground and intermediate states. This concept is expressed by the equation defining the residual spontaneous decay rate [38]:

$$R_{\mathrm{sp}} = \frac{(\Gamma_1\Gamma_2)^{3/2}}{8\Delta^2}\sqrt{\frac{I_1}{I_{\mathrm{sat},1}}\frac{I_2}{I_{\mathrm{sat},2}}} = \frac{\Gamma^3}{8\Delta^2 I_{\mathrm{sat}}}\sqrt{I_1 I_2} \tag{2.46}$$

where I_j and $I_{sat,j}$ denote the intensity and the saturation intensity of the two light beams, and Γ_j is the natural linewidth of the corresponding transition. Unlike Raman pulses, Bragg diffraction solely alters the momentum state of the atom while keeping the internal state unchanged. This distinction is crucial in applications where changes in the internal state could lead to significant losses, such as the one discussed in this thesis. The second part of the equation accounts for this, and since there is only one ground state, we have $\Gamma_1 = \Gamma_2 = \Gamma$ and $I_{\text{sat},1} = I_{\text{sat},2} = I_{\text{sat}}$.

To develop a quantum treatment of Bragg pulses, we can start with the same Hamiltonian described in the equation 2.35 but considering the interaction with two counterpropagating pulses:

$$\mathbf{E} = \frac{1}{2}\left(\mathbf{E}_1 e^{i(\mathbf{k}_1\mathbf{x} - \omega_1 t + \phi_1)} + \mathbf{E}_2 e^{i(\mathbf{k}_2\mathbf{x} + \omega_2 t + \phi_2)} + c.c.\right) \tag{2.47}$$

Starting from a plane wave with momentum $\mathbf{p}$ and in the ground internal state, $|\mathrm{g}, \mathbf{p}\rangle$,

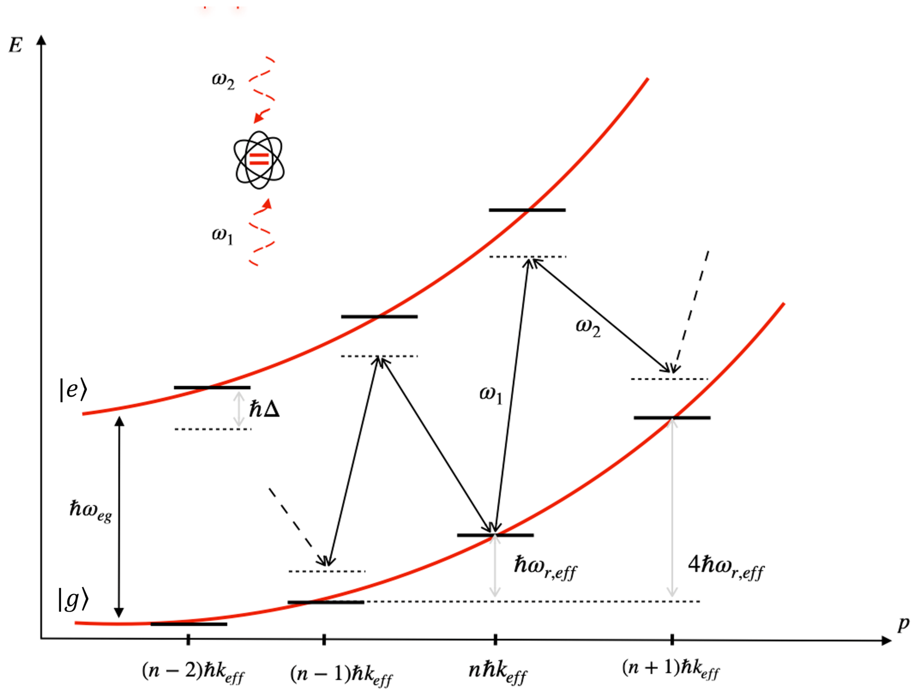

Figure 2.4: Schematisation of the Bragg diffraction process. Ta energy difference between momentum states is $\hbar\omega_{\text{r,eff}} = (\hbar k_{\text{eff}})^2/2m$.

the field with frequency ω_1 and Rabi frequency Ω_1 couples to the excited state $|\mathrm{e}, \mathbf{p} + \hbar\mathbf{k}_1\rangle$. Similarly, the counterpropagating field with frequency ω_2 and Rabi frequency Ω_2 couples the excited state to the ground $|\mathrm{g}, \mathbf{p} + \hbar(\mathbf{k}_1 + \mathbf{k}_2)\rangle$ state. Both laser fields are detuned from the transition to the excited state by the quantities $\Delta_1 = \omega_1 - (\omega_\mathrm{e} - \omega_\mathrm{g})$ and $\Delta_2 = \omega_2 - (\omega_\mathrm{e} - \omega_\mathrm{g})$. We now wish to extend the definition of the wavefunction 2.34 to the superposition of N (theoretically infinite) momentum states that are in the same ground state and are coupled with two internal excited states:

$$
\begin{aligned}
|\psi\rangle = \sum_{n=-\infty}^{\infty} \Big[& c_{\mathrm{g},\mathrm{p}_{(n-1)}} e^{-i\omega_{\mathrm{g},\mathrm{p}_{(n-1)}} t} \left|\mathrm{g}, \mathbf{p}_{(n-1)}\right\rangle + c_{\mathrm{g},\mathrm{p}_n} e^{-i\omega_{\mathrm{g},\mathrm{p}_n} t} \left|\mathrm{g}, \mathbf{p}_n\right\rangle \\
& + c_{\mathrm{g},\mathrm{p}_{(n+1)}} e^{-i\omega_{\mathrm{g},\mathrm{p}_{(n+1)}} t} \left|\mathrm{g}, \mathbf{p}_{(n+1)}\right\rangle + c_{\mathrm{e},\mathrm{p'}_n} e^{-i\omega_{\mathrm{e},\mathrm{p'}_n} t} \left|\mathrm{g}, \mathbf{p}'_n\right\rangle \\
& + c_{\mathrm{e},\mathrm{p'}_{(n-1)}} e^{-i\omega_{\mathrm{e},\mathrm{p'}_{(n-1)}} t} \left|\mathrm{e}, \mathbf{p}'_{(n-1)}\right\rangle \Big]
\end{aligned}
\tag{2.48}
$$

where $n \in \mathbb{Z}$ and we have used the notation 2.36 but with $\mathbf{p}_l = \mathbf{p} + l\hbar\mathbf{k}_{\mathrm{eff}}$ and $\mathbf{p'}_l = \mathbf{p} + \hbar(l\mathbf{k}_{\mathrm{eff}} + \mathbf{k}_1)$, where $\mathbf{k}_{\mathrm{eff}} = (\mathbf{k}_1 + \mathbf{k}_2)$. Denoting the state projectors by $P_{\alpha,\mathrm{p}_l} = |\alpha, \mathbf{p}_l\rangle \langle \alpha, \mathbf{p}_l|$, we define the new internal Hamiltonian as

$$
\begin{aligned}
\hat{H}_0 = \frac{\hat{\mathbf{p}}^2}{2m} + \sum_{n=-\infty}^{\infty} \Big[& \hbar\omega_{\mathrm{g}} \left(P_{\mathrm{g},\mathrm{p}_{(n-1)}} + P_{\mathrm{g},\mathrm{p}_n} + P_{\mathrm{g},\mathrm{p}_{(n+1)}} \right) \\
& + \hbar\omega_{\mathrm{e}} \left(P_{\mathrm{e},\mathrm{p'}_{(n-1)}} + P_{\mathrm{g},\mathrm{p'}_n} \right) \Big]
\end{aligned}
\tag{2.49}
$$

The states described by 2.48 and coupled by this Hamiltonian are those showed in Figure 2.4. We now express the interaction Hamiltonian in a more explicit form than the equation 2.35:

$$
\begin{aligned}
\hat{H}_L = & \frac{\hbar\Omega_1}{2} e^{-i(\omega_1 t + \phi_1)} \left(\left|e, \mathbf{p'}_{(n-1)}\right\rangle \left\langle g, \mathbf{p}_{(n-1)}\right| + |e, \mathbf{p'}_n\rangle \langle g, \mathbf{p}_n| + h.c. \right) \\
& + \frac{\hbar\Omega_2}{2} e^{-i(\omega_2 t + \phi_2)} \left(|g, \mathbf{p}_n\rangle \left\langle e, \mathbf{p'}_{(n-1)}\right| + \left|g, \mathbf{p}_{(n+1)}\right\rangle \langle e, \mathbf{p'}_n| + h.c. \right)
\end{aligned}
\tag{2.50}
$$

where we have omitted Hermitian conjugates for brevity. By plugging the equations 2.48, 2.49 and 2.50 into the Schrödinger equation we obtain the following differential system:

$$
\begin{aligned}
i\dot{c}_{\mathrm{g},\mathrm{p}_{(n-1)}} &= \frac{\Omega_1}{2} c_{\mathrm{e},\mathrm{p'}_{(n-1)}} e^{i(\Delta_{1,(n-1)} t + \phi_1)} \\
i\dot{c}_{\mathrm{e},\mathrm{p'}_{(n-1)}} &= \frac{\Omega_1}{2} c_{\mathrm{g},\mathrm{p}_n} e^{-i(\Delta_{1,n} t + \phi_1)} + \frac{\Omega_2}{2} c_{\mathrm{g},\mathrm{p}_{(n+1)}} e^{-i(\Delta_{2,n} t + \phi_2)} \\
i\dot{c}_{\mathrm{g},\mathrm{p}_n} &= \frac{\Omega_1}{2} c_{\mathrm{e},\mathrm{p'}_n} e^{i(\Delta_{1,n} t + \phi_1)} + \frac{\Omega_2}{2} c_{\mathrm{e},\mathrm{p'}_{(n-1)}} e^{i(\Delta_{2,(n-1)} t + \phi_2)} \\
i\dot{c}_{\mathrm{e},\mathrm{p'}_n} &= \frac{\Omega_1}{2} c_{\mathrm{g},\mathrm{p}_{(n-1)}} e^{-i(\Delta_{1,(n-1)} t + \phi_1)} + \frac{\Omega_2}{2} c_{\mathrm{g},\mathrm{p}_n} e^{-i(\Delta_{2,(n-1)} t + \phi_2)} \\
i\dot{c}_{\mathrm{g},\mathrm{p}_{(n+1)}} &= \frac{\Omega_2}{2} c_{\mathrm{e},\mathrm{p'}_n} e^{i(\Delta_{2,n} t + \phi_2)}
\end{aligned}
\tag{2.51}
$$

where the detunings are:

$$\begin{aligned}
\Delta_{1,(n-1)} &= \omega_1 - \left(\omega_{\mathrm{e},\mathrm{p'}_{(n-1)}} - \omega_{\mathrm{g},\mathrm{p}_{(n-1)}}\right)\\
\Delta_{1,n} &= \omega_1 - \left(\omega_{\mathrm{e},\mathrm{p'}_{n}} - \omega_{\mathrm{g},\mathrm{p}_{n}}\right)\\
\Delta_{2,(n-1)} &= \omega_2 - \left(\omega_{\mathrm{e},\mathrm{p'}_{(n-1)}} - \omega_{\mathrm{g},\mathrm{p}_{n}}\right)\\
\Delta_{2,n} &= \omega_2 - \left(\omega_{\mathrm{e},\mathrm{p'}_{n}} - \omega_{\mathrm{g},\mathrm{p}_{(n+1)}}\right)
\end{aligned} \tag{2.52}$$

if the population of the excited state is kept small, $|\Delta_{\alpha,l}| \gg \Omega_\alpha$, and the coefficients of the ground states and Rabi frequencies vary slowly with respect to exponentials, it is possible to adiabatically eliminate the excited state amplitude by integrating the equation defining $\dot{c}_{\mathrm{e},\mathrm{p'}_{(n-1)}}$ and $\dot{c}_{\mathrm{e},\mathrm{p'}_{n}}$ and substituting the results in $\dot{c}_{\mathrm{g},\mathrm{p}_{(n-1)}}$, $\dot{c}_{\mathrm{g},\mathrm{p}_{n}}$ and $\dot{c}_{\mathrm{g},\mathrm{p}_{(n+1)}}$ of the system 2.51:

$$\begin{aligned}
i\dot{c}_{\mathrm{g},\mathrm{p}_{(n-1)}} &= \frac{\Omega_1^2}{4\Delta_{1,(n-1)}} c_{\mathrm{g},\mathrm{p}_{(n-1)}} + \frac{\Omega_1\Omega_2}{4\Delta_{2,(n-1)}} c_{\mathrm{g},\mathrm{p}_{n}} e^{i[\delta_{(n-1)}t+\phi_1-\phi_2]}\\
i\dot{c}_{\mathrm{g},\mathrm{p}_{n}} &= \left[\frac{\Omega_1^2}{4\Delta_{1,n}} + \frac{\Omega_2^2}{4\Delta_{2,(n-1)}}\right] c_{\mathrm{g},\mathrm{p}_{n}} + \frac{\Omega_1\Omega_2}{4\Delta_{2,n}} c_{\mathrm{g},\mathrm{p}_{(n+1)}} e^{i[\delta_n t+\phi_1-\phi_2]}\\
&\quad + \frac{\Omega_1\Omega_2}{4\Delta_{1,(n-1)}} c_{\mathrm{g},\mathrm{p}_{(n-1)}} e^{-i[\delta_{(n-1)}t+\phi_1-\phi_2]}\\
i\dot{c}_{\mathrm{g},\mathrm{p}_{(n+1)}} &= \frac{\Omega_2^2}{4\Delta_{2,n}} c_{\mathrm{g},\mathrm{p}_{(n+1)}} + \frac{\Omega_1\Omega_2}{4\Delta_{1,n}} c_{\mathrm{g},\mathrm{p}_{n}} e^{-i[\delta_n t+\phi_2-\phi_1]}
\end{aligned} \tag{2.53}$$

In this system we have introduced $\delta_n = \Delta_{1,n} - \Delta_{2,n} = \omega_1 - \omega_2 - \left[\frac{(2n+1)\hbar|\mathbf{k}_{\mathrm{eff}}|^2}{2m} + \mathbf{v}\mathbf{k}_{\mathrm{eff}}\right]$ and $\delta_{(n-1)} = \omega_1 - \omega_2 - \left[\frac{(2n-1)\hbar|\mathbf{k}_{\mathrm{eff}}|^2}{2m} + \mathbf{v}\mathbf{k}_{\mathrm{eff}}\right]$. If we focus on the rightmost terms in the equation 2.53, we observe similarities with those of an actual two-level system, albeit with an effective (two-photon) Rabi frequency $\Omega_{\mathrm{eff}} = \Omega_1\Omega_2/(2\Delta_{\alpha,l})$. In this scenario, the system is driven by an effective laser with frequency $\omega_{\mathrm{eff}} = \omega_1 - \omega_2$, effective wavevector $\mathbf{k}_{\mathrm{eff}}$, and effective phase $\phi_{\mathrm{eff}} = \phi_1 - \phi_2$.
Conversely, the first two terms depict the light-induced shift of the atomic levels. Notably, if these terms are equal, they merely alter the energy offset without inducing any significant effects. However, discrepancies between these terms result in a modification of the frequency difference between the two ground states. These light-induced shift terms can pose challenges in precision measurements, particularly when considering the intensity profile of the laser beams. Under such circumstances, the spatial variation of the Rabi frequency may lead to undesirable interferometer phase shifts.

The system 2.53 reveals that the state of an atom in a particular internal and momentum state, immersed in two counter-propagating fields, couples with neighboring momentum states in a manner dependent on the fields' power, their detuning, and the probability amplitudes of the states. By properly setting the field parameters, it is possible to carry out multiple cycles of absorption and emission, coupling

states that differ by a high number of laser momenta (higher diffraction orders).
A Mach-Zehnder interferometer such as the one shown in Figure 2.1 composed of Bragg pulses should consist of three pairs of counterpropagating pulses capable of transferring the same number of laser moments and with powers and interaction times such that the configuration $\pi/2$, π, $\pi/2$ is respected. In this framework, one can write the g-dependent phase shift with the wave vector and the effective laser phase shift as:

$$\Delta\phi = \mathbf{k}_{\text{eff}} g T^2 \hat{\mathbf{z}} + \phi_{\text{eff}_1} - 2\phi_{\text{eff}_2} + \phi_{\text{eff}_3} \tag{2.54}$$

where $\phi_{\text{eff}_i} = \phi_1(t_i) - \phi_2(t_i)$.

Chapter 3

Photodetachment Stage

Photodetachment, a fundamental process in atomic and molecular physics, involves the interaction of a photon with a neutral atom or ion: the ionization process, which occurs after the absorption of photon energy, results in the liberation of a bound electron, transforming it into a free electron [81]. This dual process has wide-ranging implications across scientific and technological domains such as photoelectron spectroscopy, a technique used to study the electronic structure of atoms and molecules [82]. By measuring the kinetic energy of the electrons emitted during the photodetachment process, detailed information about the distribution of electronic states in the system under investigation can be obtained [83]. Moreover, photodetachment is important for molecular chemistry [84], and antimatter research [46–48, 85, 86]. In research laboratories, it is used to study, manipulate and control atomic and molecular systems.

In the context of this work, photodetachment finds its usefulness considering that Ps is an electrically neutral system and it is therefore necessary to use the negatively charged ion, Ps^-, to guide and focus the atomic beam. Ps^- can be considered an intermediate system between atomic H^+ and molecular H^{2+} systems due to its mass ratio, which makes it an intriguing subject for fundamental physics investigations that also touches on the three-body problem that lacks an analytical solution. Theoretical studies suggest that Ps^- possesses only a ground state where the two electrons exhibit opposite spins, distinguishing it from the H^- ion [47].

The prediction of Ps^- by Wheeler in 1946 marked the beginning of its theoretical exploration, leading to its experimental discovery by Mills in 1981 using the beam-foil method [87, 88]. Despite its theoretical interest, experimental investigations on Ps^- have been limited due to its low ion yield and short annihilation lifetime of 479 ps. However, advancements in Ps^- formation have facilitated studies on Ps^- photodetachment and the production of energy-tunable Ps beams, expanding the scope of experimental research on this exotic ion [48, 85].

In the photodetachment of Ps^-, the resulting Ps atoms are typically found in the ground state, with two spin eigenstates depending on the total spin of the constituents [89]. Para-positronium (p-Ps, 1^1S_0) primarily decays into two photons with a short lifetime of 125 ps, while ortho-positronium (o-Ps, 1^3S_1) decays into three photons with a longer lifetime of 142 ns in vacuum [90]. The population ratio of p-Ps and o-Ps formed during photodetachment follows the spin statistics weight of 1:3, with o-Ps being the dominant state [91]. A review of the status of the research for the three-body positronium negative ion ($e^-e^+e^-$) and the four-body positronium molecule ($e^-e^+e^-e^+$) is reported in Ref. [92].

Ps$^-$ may not possess any excited states, but Ps ions have a rich structure of resonances. One can simply think of Ps ion as a ground-state Ps atom surrounded by a weakly bound electron in a singlet-state relative to the Ps electron. Quasi-bound states (resonances) have been theoretically predicted in the vicinity of the formation thresholds of Ps (for principal quantum number $n \geq 2$). Although the resonance states spontaneously dissociate into positronium, for example in the ground state, the interference between the direct detachment process and the detachment via the resonance state produces distinguishing features on the cross sections near the resonance energy. Mills [93] estimated the cross section for photoionization of the Ps ion system at the lowest ($n = 2$) Feshbach resonance in 2013. He neglected the influence of the weakly bound outer electron. The obtained result is $\sigma_F = 1.4 \times 10^{-12}$ cm^2. The cross section of the Ps$^-$ photodetachment has been extensively studied over the past decades: a two-photons deteachment has been reported in Ref. [94] while Figure 3.1 shows the results of several studies for the single photon case. The image and the curve labeled as "present" refers ti the study in Ref. [50]. The Figure 3.1 shows two peaks that might be convenient to exploit: the one with a peak at about 0.7 eV and the resonance peak at about 5.5 eV (n=2). The wavelengths corresponding to these peaks are approximately 1800 nm and 225 nm. We decide to exploit the region around the peak at the highest wavelength and to discard the resonance at $n = 2$ for two main reasons:

- The UV peak has a very narrow width and therefore, due to the Doppler effect, imposes a more stringent upper limit on the velocity classes of the atomic beam that can be used; moreover, the Doppler effect is more significant for higher frequencies.
- As we will see in Section 3.2, photodetachment can have a detrimental effect on the beam's kinematics, causing broadening. This effect is proportional to the energy of the photons.

For experimental convenience, including access to a wide range of commercially available equipment, the capability to achieve high powers, and availability of components in the laboratory, we opt to operate at a wavelength of 1560 nm, corresponding to a cross-section of approximately 6.5×10^{-17} cm^2.

The efficiency of the photodetachment thus depends on the nature of the atom

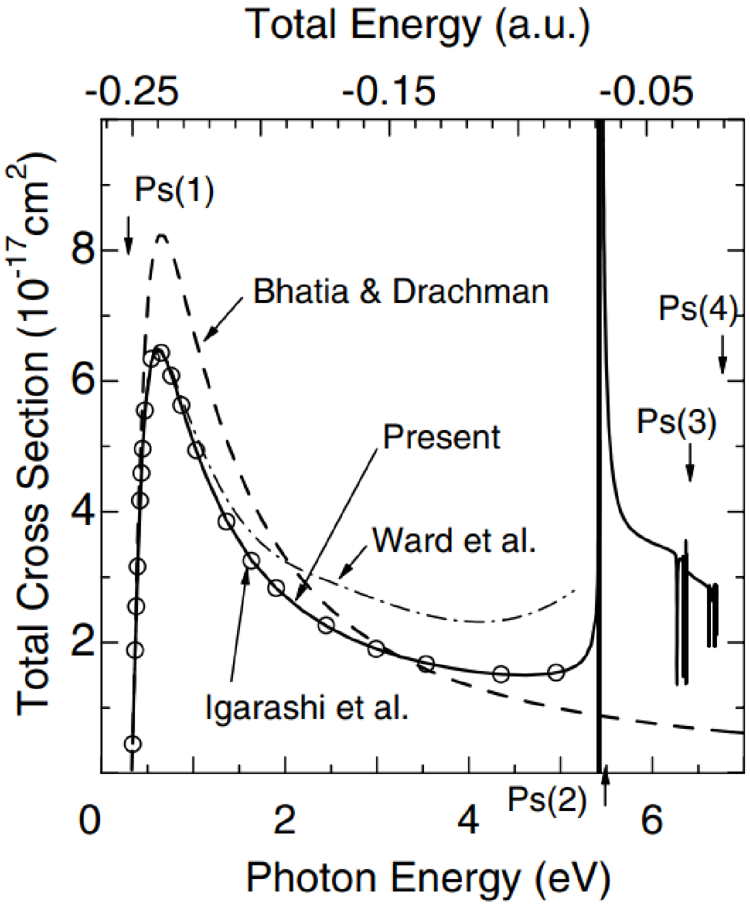

Figure 3.1: Theoretical values of the total cross section for the positronium negative ion photodetachment below the Ps (n = 4) threshold according to various works in the literature [95–97]. The image and the curve labeled as "present" refer to the study in Ref. [50].

or ion via the cross section, the energy of the incident photon, but also the interaction time between the atomic beam and the laser. These dependencies are well summarised by the equation defining the photodetachment probability [98]:

$$P_{\mathrm{pd}} = 1 - e^{-\sigma \int_{t_1}^{t_2} \Phi_{\mathrm{ph}}\, dt} \tag{3.1}$$

where Φ_{ph} is the photon flux, σ is the photodetachment cross section and (t_2-t_1) is the time interval in which an ion interacts with the laser. The flux is defined by $\Phi_{\mathrm{ph}} = \frac{I(t)}{hc/\lambda}$ with h Planck's constant, c speed of light and I(t) laser intensity. Given the Ps and Ps^- lifetimes, it is necessary for the atomic beam to be accelerated to relatively high speeds. In fact, the design speed of the Ps beam is 200 eV, which corresponds to approximately 6x10^6 m/s. Assuming a 0.7 mm waist beam and an atom passing through it along its diameter, the interaction time is therefore about Δt=0.23 ns. Considering the relation between intensity and peak power, $I_0 = \frac{2P_0}{\pi w_0^2}$, with w_0 laser waist, and neglecting the Gaussian shape for the moment, we can estimate the power required to obtain a 95% maximum photodetachment probability with

$$P_0 = -\frac{\pi h c w_0^2}{2\sigma\lambda\Delta t}\ln(1-0.95) \simeq 193\,kW \tag{3.2}$$

Since we want to ensure a high photodetachment probability even for ions crossing the laser beam peripherally, we round up the design power to 200 kW. To achieve a broader waist for capturing a larger number of atoms from a poorly collimated atomic beam and to ensure high light intensity and resonator stability a confocal Fabry-Pérot resonator was chosen. This choice was made to optimize the photodetachment process efficiency, while balancing experimental feasibility. Considering that powers of the order of 30 W are commercially available and assuming a laser-cavity coupling of 50%, to attain the required optical power, a finesse of 40000 has been chosen. The cavity operates in continuous mode primarily because the experiment was originally designed to use ^{22}Na as the positron source. Sodium requires continuous operation to avoid losses in accumulation stages. The consideration of using a LINAC is a recent development, and its operational parameters-such as repetition rate and pulse length-need to be defined with greater precision. This process could take time, especially if we use the LINAC currently under construction, as previously mentioned in Section 1.2. Therefore, project plans to use continuous-mode cavity, with the added goal of testing the excitation and interferometry components using the ^{22}Na source already available in the Milan laboratory. This versatile cavity then has the advantage that it can also be used effortlessly with a LINAC, being totally independent of its operating parameters.

3.1 Optical cavity simulation

During the design and optimization activities of the high-power optical cavity, simulations were conducted to address two main issues regarding the interfacing of the atom source electrodes with the laser cavity and the risk of mirror deformation due to the high circulating power.

One of the main aspects concerned the correct positioning of the electrodes of the atomic source with respect to the laser beam inside the cavity. This issue stems from the need to bring the Ps$^-$ source as close as possible to the laser beam in order to minimise annihilation losses but at the same time the interference with the laser beam could compromise the overall cavity performance due to diffraction losses. To address this issue, optical simulation using OSCAR [99] has been employed.

Another significant issue is associated with the possibility of the high circulating power within the cavity causing mirror deformations, thereby compromising the efficiency and performance of the cavity. To analyze this potential issue, thermal and structural analysis was performed by Finite Element Modeling (FEM) using Ansys. The integration of the results obtained from Ansys with the optical simulations from

OSCAR allowed for a comprehensive assessment of the impact of high power on the geometry and performance of the mirrors.

3.1.1 OSCAR: working principles

OSCAR, or Optical Simulation Code for Advanced Resonators, is a powerful FFT-based simulation tool made by Jérôme Degallaix for LIGO simulations and designed to model Fabry-Pérot cavities with arbitrary mirror profiles. The underlying principle of OSCAR's optical propagation code resembles the Fourier transformation method employed to compute the response of a linear system to an arbitrary function $f_i(t)$.

In this method, $f_i(t)$ is represented as a continuous superposition of harmonic functions of various frequencies ν:

$$f_i(t) = \int \tilde{f}_i(t) e^{2\pi j \nu t} d\nu$$

where $\tilde{f}_i$ denotes the Fourier transform of f_i, and $e^{2\pi j\nu t}$ represents the harmonic function of frequency ν used to expand f_i.

By knowing the system's response to each elementary harmonic function $e^{2\pi j\nu t}$, the response to the input f_i can be derived through three fundamental steps. Firstly, f_i is decomposed into the sum of basic harmonic functions via Fourier transformation. Secondly, the system's response to each harmonic function is computed, simply achieved by multiplication in the frequency domain. Finally, the output of the system to the input f_i is obtained by performing the inverse Fourier transformation of the output harmonic functions. In the context of OSCAR, the elementary functions are represented by plane waves of differing spatial frequencies.

A plane wave propagating a distance d along the x-axis can be written as

$$u(d, y, z) = \exp\{-j(k_x d + k_y y + k_z z)\} \tag{3.3}$$

which identifies the phase of the wave along the plane perpendicular to the propagation axis. With the paraxial approximation ($k_x \gg k_y, k_z$)we can write

$$k_x = \sqrt{|\mathbf{k}|^2 - k_y^2 - k_z^2} \simeq |\mathbf{k}| - \frac{(k_y^2 + k_z^2)}{2|\mathbf{k}|} \tag{3.4}$$

Plugging in the spatial frequencies $\nu_i = k_i/2\pi$ we obtain that the equation 3.3 becomes:

$$u(d, y, z) = u(0, y, z) \exp\bigl\{-j(|\mathbf{k}| - \lambda\pi(\nu_y^2 + \nu_z^2))d\bigr\} \tag{3.5}$$

The term $\exp(-j|\mathbf{k}|d)$ represents the phase shift of a plane wave propagating along the x axis and the term $\exp\bigl(-j\lambda\pi(\nu_y^2 + \nu_z^2)d\bigr)$ adds a phase correction to take into account the fact that the wave propagates with a small angle with respect to the x axis.

We now want to understand how to propagate a generic electric field $\mathbf{E}(y,z)$ that will represent the laser inside the optical cavity. We can expand the field into a set of plane waves such as:

$$\mathbf{E}(y,z) = \int\int \tilde{\mathbf{E}}(\nu_y,\nu_z)\exp\{-2\pi j(\nu_y y+\nu_z z)\}d\nu_y d\nu_z \tag{3.6}$$

If we think of this equation as an inverse Fourier transform, we have that

$$\tilde{\mathbf{E}}(\nu_y,\nu_z) = \int\int \mathbf{E}(y,z)\exp\{2\pi j(\nu_y y+\nu_z z)\}dydz \tag{3.7}$$

In summary, OSCAR performs the following tasks:

- Decomposition of the field $\mathbf{E}(0,y,z)$ into a sum of elementary plane waves by calculating the 2D Fourier transform: $\tilde{\mathbf{E}}(0,y,z) = \mathcal{F}(\mathbf{E}(0,y,z))$.
- Propagation of each plane wave by adding a phase shift in the frequency domain: $\tilde{\mathbf{E}}(d,\nu_y,\nu_z) = \tilde{\mathbf{E}}(0,\nu_y,\nu_z)\exp\big(-j(|\mathbf{k}| - \lambda\pi(\nu_y^2+\nu_z^2))d\big)$.
- Recomposition of the electric field from the propagated plane waves by computing the inverse Fourier transformation: $\mathbf{E}(d,y,z) = \mathcal{F}^{-1}(\tilde{\mathbf{E}}(d,y,z))$.

As previously mentioned, equation 3.3 defines a wave in a plane perpendicular to its direction. However, when implementing this equation computationally, the plane needs to be discretized, effectively creating a 2D matrix. The dimensions of this matrix should be chosen carefully, depending on the specific physical system under simulation. It's crucial to select a matrix size with a sufficiently high number of rows and columns to ensure a high-resolution representation of the propagating fields over the desired physical length.

Moreover, the process involves computing the discrete Fourier transform (DFT) of this 2D matrix. The DFT of a complex 2D matrix results in another complex 2D matrix with the same dimensions. In the transformed domain, the low spatial frequencies are concentrated in the center of the matrix, while the high spatial frequencies are located towards the edges. This distribution reflects the nature of the Fourier transform, where lower frequencies correspond to variations occurring over longer distances, while higher frequencies represent rapid changes over shorter distances.

Furthermore, the spatial frequency resolution, which determines the level of detail captured in the simulation, is inversely proportional to the total spatial length of the system. Therefore, a larger system with more significant spatial extent would require finer frequency resolution to accurately represent the propagating fields. After setting up the problem in this way, propagation becomes nothing more than an element-wise multiplication between the matrix containing $\tilde{\mathbf{E}}(\nu_y, \nu_z)$ and a propagation matrix defined at the beginning of the calculation, which is used each time the field needs to propagate from one end of the cavity to the other. What is missing in this discussion is the inclusion of mirrors and optical components.

When a laser field $\mathbf{E}_i$ traverses a medium with a non-uniform refractive index $n(x, y, z)$, it undergoes distortion of the wavefront at each point in space (y, z) due to the difference in optical path length between all points in the plane (y, z) and the propagation axis:

$$\Delta\text{OPL}(y, z) = \int_0^L n(x, y, z)dx - \int_0^L n(0, y, z)dx \tag{3.8}$$

$$\mathbf{E}_f(y, z) = \mathbf{E}_i(y, z)\exp\{-j|\mathbf{k}|\Delta\text{OPL}(y, z)\} \tag{3.9}$$

When propagating a laser beam towards a mirror, its profile must be taken into account. If, for example, the mirror is concave, the optical path difference will be two times the sagitta (see Figure 3.2) $\Delta s = R_{ofC} - \sqrt{R_{ofC}^2 - \Delta r^2}$. By changing the mirror profile, realistic optics can be simulated by adding, for example, tilts, roughness or other deformations such as thermal deformations.

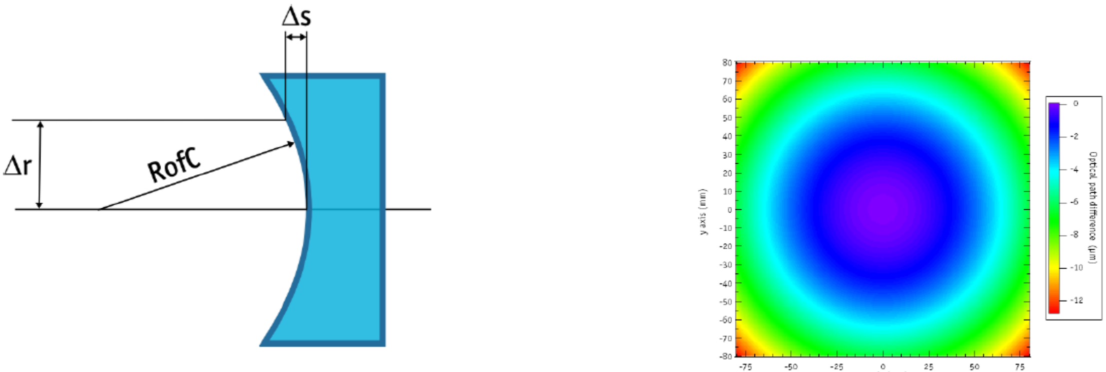

(a) Profile of a spherical mirror with radius of curvature R_{ofC} and sagitta Δs.

(b) Corresponding optical path difference.

Figure 3.2: Profile and optical path difference of a spherical mirror. Images taken from OSCAR manual [99].

After specifying the laser properties (such as wavelength and initial beam shape), mirror characteristics (including diameter, profile, refractive index, reflectivity and losses), and resonator (such as configuration and length), we can estimate the characteristics of the field inside the cavity. This can be done by launching the beam either from outside, considering the coupling, or from inside the cavity. The code is capable of adjusting the Gaussian beam parameters to optimize its coupling with the cavity, determining parameters like waist and radius of curvature, or it can accept these parameters from the user.

The simulation of the cavity begins with a field, defined for example outside, which propagates through the first mirror and then into the cavity. A portion of the field is reflected by the mirror, accumulating and adding up within the cavity, while the rest is transmitted or absorbed depending on the mirror's characteristics. This process continues until reaching the maximum number of iterations, and the total field is the sum over all round trips of the transient fields. The procedure is analogous to the analytical method for calculating the circulating field in an optical cavity [100] and is illustrated in Figure 3.3. In a lossy cavity, the accumulated field is always finite, and the power of the transient field decreases by (1-$\mathcal{L}$) per round trip, with $\mathcal{L}$ being the round trip cavity loss. This implies that we can choose the number of iterations as desired, provided it is high enough to represent a steady-state condition.

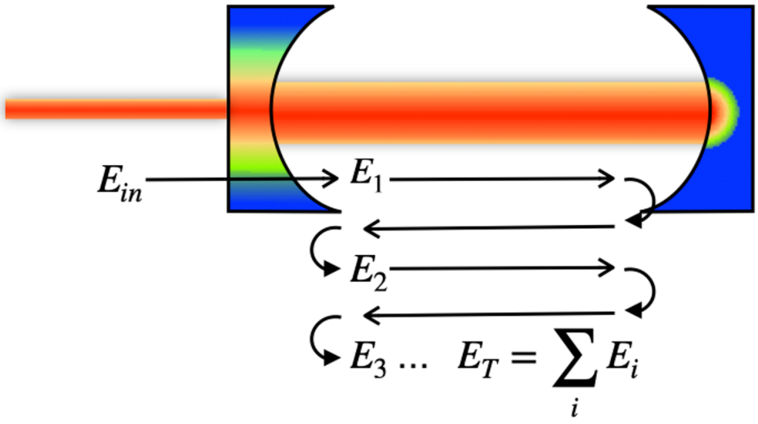

Figure 3.3: Schematisation of the process of calculating the circulating field as the sum of the fields resulting from mirror reflection and propagation in cavity.

3.1.2 Design cavity analysis and loss assessment

The mirrors chosen for the photodetachment cavity are one-inch fused silica mirrors with 80% clear aperture (CA), 6.35 mm thickness and 2 metre radius of curvature. The high reflectivity coating has a transmission of 78 ppm (parts per million) with very low absorption losses of about 0.15 ppm. The anti-reflective (AR) coating has a transmission coefficient of about 0.999 and an absorption of about 200 ppm. The cavity mirrors are the same.

As mentioned at the beginning of the chapter, the mirrors were selected with these specific characteristics to achieve a circulating power on the order of 200 kW and ensure a sufficiently large beam waist. This allows for a substantial interaction cross-section between the atomic beam and the light. The cavity spacer is an assembly of ultra-high vacuum compatible tubes that separate the mirrors over a length of approximately 2.04 m. For the simulation, a field with a Gaussian profile with a wavelength of 1550 nm, an input power of 15 W, a waist at the mirrors of approximately 1.05 mm and a wavefront radius of curvature of about 1.4 m is defined

Table 3.1: Powers relative to the cavity under design conditions

Parameter	**Value**
Power in the input beam	15 W
Circulating power	197.5 kW
Transmitted power	14.93 W
Reflected power	0.009 W

outside the cavity. Both the waist and radius of curvature wavefront were optimised by finding values that maximise cavity coupling and circulating power. Running the code to calculate the circulating power under the conditions just described yields the results listed in table 3.1.

The results indicate that the cavity is capable of achieving a power close enough to the required value as per the design. The achieved coupling is almost 100%, which is a highly optimistic condition. However, as mentioned, the plan is to increase the input power to around 30 W to attain this circulating power even with a lower coupling efficiency. Figure 3.4 shows the input, circulating, reflected and transmitted fields. Since there is near-perfect matching in the design condition, the circular symmetry of the reflected field may represent higher-order modes suppressed by the cavity while the other fields are Gaussian shaped. In this simulation, the etalon effect has also been taken into account, considering that the reflection from the AR and HR surfaces creates a cavity within the mirror itself. Under conditions of destructive interference, the etalon effect can decrease field transmission and increase losses. Within the code, a number of iterations for the etalon effect can be defined, reaching steady-state conditions with about 4 iterations. Among the causes that can increase this effect is the fact that mirrors have a relatively large radius of curvature, which for a CA of one inch results in an almost flat profile for both surfaces. In the absence of compensation for the etalon effect, the power transmitted through the input mirror, and consequently the circulating power, depends on the thickness of the mirror and can oscillate significantly with variations in thickness smaller than the laser wavelength. The circulating power reported in table 3.1 was obtained by adjusting the mirror thickness to minimize the etalon effect, thereby emulating an optimal compensation of the effect. Further details on this point will be provided at the end of this section (see Figure 3.12).

We can now address the issue of positioning the Ps^- acceleration and focusing system shown in Figure 1.3 with respect to the laser beam. Note that from now on we will assume that the atoms move primarily along the z-axis and that the gravity acceleration is antiparallel to the y-axis. As can be seen from the Figure 1.3, the closest obstruction to the laser beam is the 0 V grid. If this overlaps even peripherally with the laser beam, there is a risk of loss of cavity power. The obstruction is modelled as an asymmetrical rectangular aperture (on one side only) whose distance

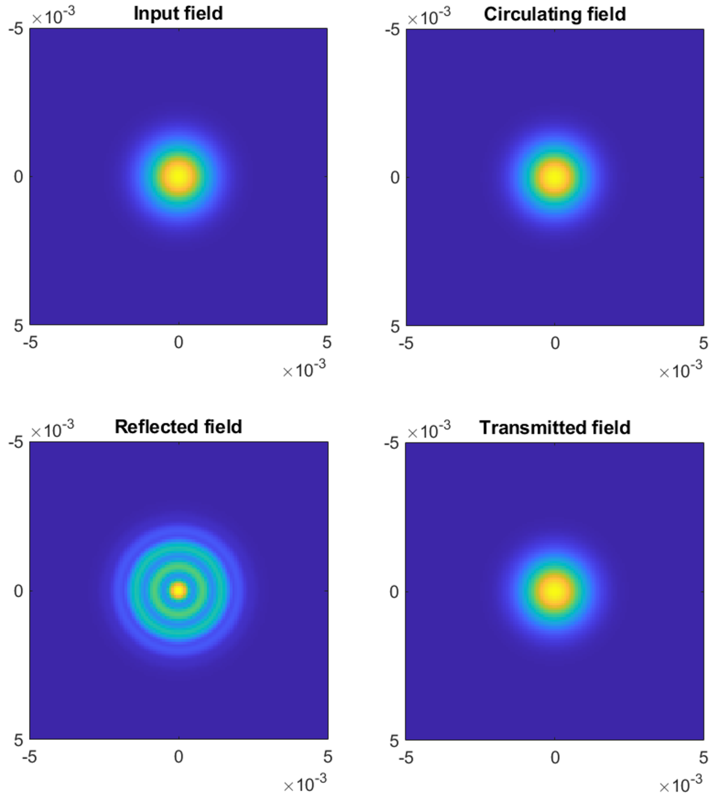

Figure 3.4: Profiles of the cavity electric fields under design conditions. The grid captures an area of $1 \times 1\,\mathrm{cm}^2$ and the resolution is approximately 0.08 mm.

from the centre of the beam, Δz_o, is the quantity to be optimised. A diagram of the model is shown in Figure 3.5.
This obstruction can be incorporated into OSCAR as a mask covering the mirror's HR coating. Basically, it is a matter of multiplying the matrix that defines the profile of the mirror by a matrix of equal size having null values where the obstruction is. This modifies the equation 3.9 as follows:

$$\mathbf{E}_f(y,z) = \mathbf{A}(y,z)\mathbf{E}_i(y,z)\exp\{-j|\mathbf{k}|\Delta\mathrm{OPL}(y,z)\} \tag{3.10}$$

where A is the aperture matrix. Note that this method does not take into account effects that may arise from the interaction of the beam with objects in the cavity, such as reflections or diffractions, which we nevertheless consider negligible in this analysis. However, the model is pessimistic because it assumes the grid is near the mirror, where the laser diameter is larger, whereas in reality it is near the waist. We will disregard this issue for the sake of an even more conservative estimate. We aim to determine the minimum Δz_o with $0 < \Delta z_o \leq \mathrm{CA}/2$ that allows achieving the design circulating power indicated in 3.1. Therefore, we can simulate under design conditions but by setting Δz_o as a parameter. Figure 3.6a illustrates the round trip

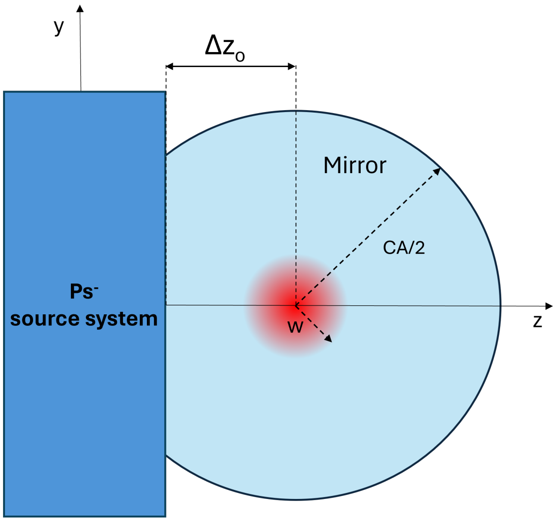

Figure 3.5: Schematisation of the cavity obstruction generated by the acceleration and focusing sytem. The atoms move towards the z-axis and the cavity is along the x-axis. The blue circle is one of the two mirrors and the red circle represents a section of the laser. Δz_o is the distance between the obstruction and the centre of the laser that is to be optimised.

losses and circulating power as a function of Δz_o while 3.6b shows the profiles of the fields within the cavity with their respective circulating powers for different values of Δz_o.

For low values of Δz_o the obstruction destroys the circulating beam causing losses to increase and the circulating power to decrease drastically. For $\Delta z_\mathrm{o} \leq 2w_0$ the shading of the obstruction becomes visible and the beam profile shows fringes attributable to asymmetrical propagation in the cavity. The analysis shows that the circulating power returns to its design value for $\Delta z_\mathrm{o} > 2.5$ mm, which has been therefore chosen as the design distance.

Under these conditions, from the last acceleration electrode to the center of the laser beam, the Ps$^-$ beam is approximately halved. To grasp the importance of optimizing this distance, consider that if we had chosen a conservative condition where $\Delta z_\mathrm{o} = \mathrm{CA} \simeq 20$ mm, the resulting beam would have been only about 1% of that exiting the acceleration and focusing system.

3.1.3 Thermo-elastic and thermo-optic effects

The thermal effects felt by an optical medium result from a temperature change that causes a difference in optical path. The most prominent for our interests are the thermal expansion (thermo-elastic effect) and the change of the refraction index (thermo-optic effect):

$$\Delta\mathrm{OPL}(\mathbf{r}) = \Delta n(\mathbf{r}) \cdot l + n \cdot \Delta l(\mathbf{r}) \tag{3.11}$$

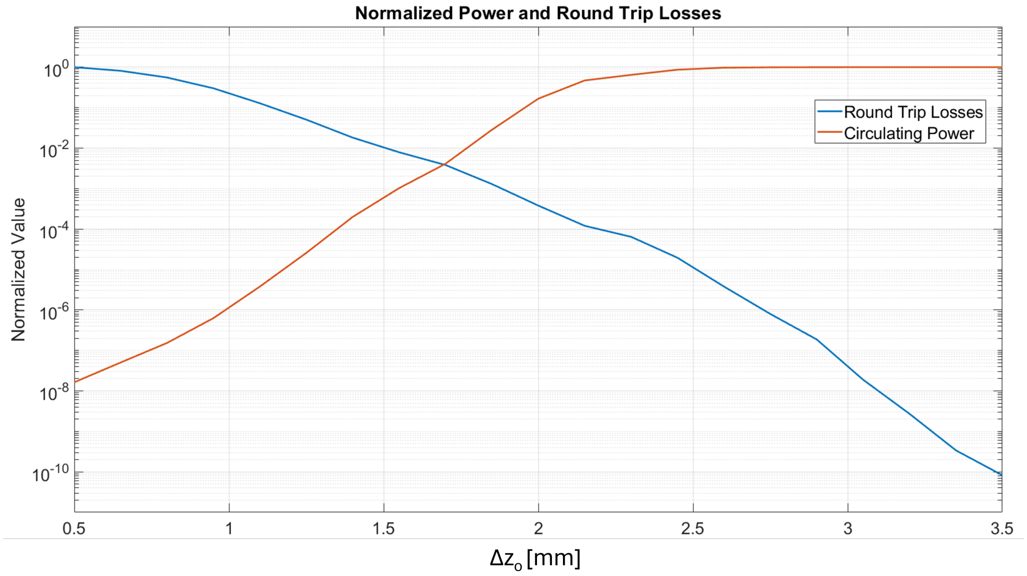

(a) Round trip losses and circulating power as a function of the distance between the cavity obstruction and the centre of the laser beam. The quantities are normalised to their maximum value.

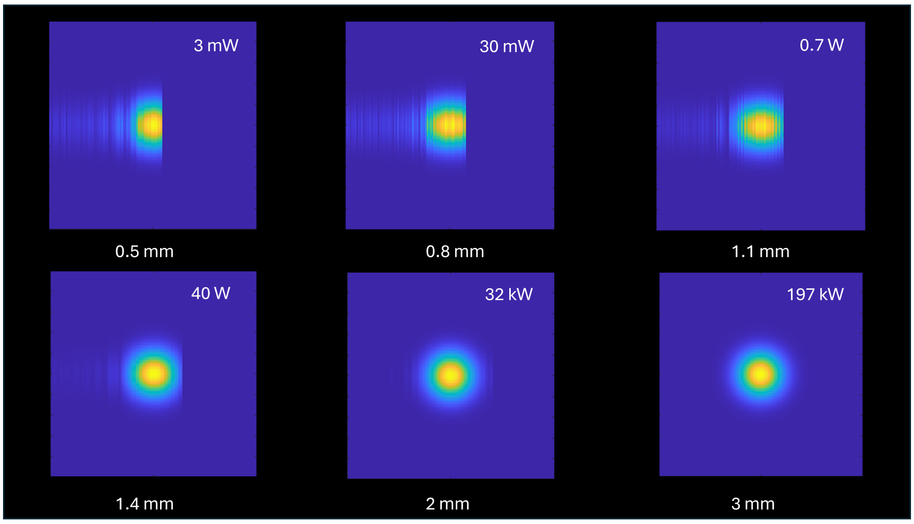

(b) Normalized circulating field profiles and circulating powers as a function of different values of Δz_{o}.

Figure 3.6: Evaluation of cavity losses for different Ps^{-} focussing system positions.

with l thickness of the medium. In the equation 3.11 we have neglected the variation of the refractive index due to possible stresses in the material (photoelastic effect) since it is generally less than the thermo-optic effect for various optical materials [101].

The thermo-elastic effect is a fundamental phenomenon encountered in materials science and engineering, particularly in the realm of high-power laser systems. As these systems operate under demanding conditions, often generating intense beams of coherent light, they are inherently susceptible to variations in temperature that induce mechanical stresses within their components. Understanding and characterizing the thermo-elastic behavior of these components is crucial for ensuring the reliability, performance, and longevity of high-power laser systems. By accurately predicting the thermal-induced stresses and strains, robust optical systems can be designed to withstand the constraints of high-power laser operation [102].

At its core, the thermo-elastic effect describes the mechanical response of materials to changes in temperature. When subjected to thermal gradients, materials change their dimensions due to thermal expansion or contraction, leading to the development of internal stresses. This phenomenon arises from the interplay between the material's thermal properties, condensed in the coefficient of thermal expansion, and its mechanical properties, expressed by its modulus of elasticity.

Mathematically, the thermo-elastic effect can be described by fundamental equations that govern the relationship between temperature, stress, and strain in a material. One such equation is Hooke's law, which relates stress to strain through the material's elastic modulus.

Additionally, the strain experienced by a material due to thermal expansion (ε_{th}) can be expressed as:

$$\varepsilon_{th} = \alpha \cdot \Delta T \tag{3.12}$$

Where α is the coefficient of thermal expansion and ΔT is the change in temperature.

In the context of high-power laser systems, the thermo-elastic effect manifests itself in various ways. For example, the optical components within the laser cavity, such as mirrors and lenses, experience thermal loading from the intense laser beams. This thermal loading induces mechanical stresses within the optical elements, potentially leading to deformation or even breakage if not properly managed.

Thermo-optic effect is a fundamental phenomenon influencing the performance of optical devices like mirrors and lenses under temperature variations. It is often not negligible in high-power laser systems [103, 104].

The thermo-optic effect manifests as a change in the refractive index of an optical material in response to temperature variations: $\Delta n = n(T_1) - n(T_0)$. This change affects light propagation through the material, altering optical properties such as phase velocity and refractive angle. Particularly in high-power lasers, refractive index variations can lead to unwanted phenomena like laser beam distortion, optical resonator instability and unwanted couplings with higher-order modes [105–108]. The refractive index change is proportional to the temperature difference ΔT through the coefficient $\beta = \frac{dn}{dT}$:

$$\Delta n(\mathbf{r}) = \beta \cdot \Delta T(\mathbf{r}) \tag{3.13}$$

β is the thermo-optic coefficient that varies depending on the material considered.

There are various analytical models for evaluating thermo-elastic and thermo-optic effects on optical components. Typically, in a high-power cavity, the HR coating absorbs and heats up due to exposure to the circulating power, while also heating the substrate through conduction. The substrate, subject to a temperature gradient, acts as a lens and distorts the wavefront (thermal lensing). Furthermore, its expansion affects the coating, altering the mirror's radius of curvature. Additionally, the absorption of the transmitted beam through the substrate may also be non-negligible, specifically when the optic is extended longitudinally. Although the behavior of the HR coating and the substrate are interconnected, their effects are often considered separately.

The thermo-optic effect given by the mirror substrate is defined by the equation 3.13, which needs a definition of $\Delta T(\mathbf{r})$ to be used. A simple analytical model [101, 109] defines the temperature variation along the mirror profile in the case of a mirror of infinite size with radial heat flow and hit by a Gaussian beam as:

$$\Delta T(\mathbf{r}) = |T(\mathbf{r}) - T_0(\mathbf{r})| = \frac{\alpha' P_{\text{ab}}}{4\pi\kappa_{\text{th}}} \sum_{l=0}^{\infty} \left[\frac{(-1)^l (2r^2/w^2)^l}{l l!} \right] \tag{3.14}$$

Here, $T_0(\mathbf{r})$ is the temperature of the mirror at rest, α' represents the substrate's thermal expansion coefficient per unit length, P_{ab} denotes the absorbed power, κ_{th} is the thermal conductivity and w is the waist at the mirror. The power absorbed by the substrate is the power transmitted through the mirrors times the absorption coefficient: $P_{\text{ab}} = A_{\text{sub}} P_{\text{t}}$.

The thermo-optic effect results in a change in the focal length of the optical component, which can be seen as a change in an effective radius of curvature that is, at first order, given by:

$$\frac{1}{R'_{\text{ofC}}} \simeq \frac{1}{R_{\text{ofC}}} - \frac{\beta P_{\text{ab}}}{2\pi\kappa_{\text{th}} w^2} \tag{3.15}$$

Given that our setup primarily involves the interaction of the laser with reflective optics, except for transmission through a mirror (pseudo output coupler), we expect the total optical path length difference (ΔOPL) to be dominated by the thermo-elastic effect. This effect, resulting from the substrate heating caused by power absorption in the mirror coatings and substrate, leads to a sag variation given by

[105]:

$$\Delta s \simeq \frac{\alpha P_{\mathrm{ab}}}{4\pi\kappa_{\mathrm{th}}} \tag{3.16}$$

where α represents the substrate's thermal expansion coefficient. A diagram of this deformation is shown in Figure 3.7. Note that the thermo-optic effect has a role only in the transmission of the field through the first mirror (it is present in both mirrors, but the first one defines the cavity field) while the thermo-elastic effect is relevant for both mirrors of the cavity. The absorbed power is the sum of the power absorbed by the coating and the substrate: $P_{\mathrm{ab}} = A_c P_{\mathrm{c}} + A_{\mathrm{sub}} P_{\mathrm{t}}$, where A_c is the absorption coefficients of the coating and P_{c} represent the circulating and power. Δs induces a variation in the radius of curvature according to the relation:

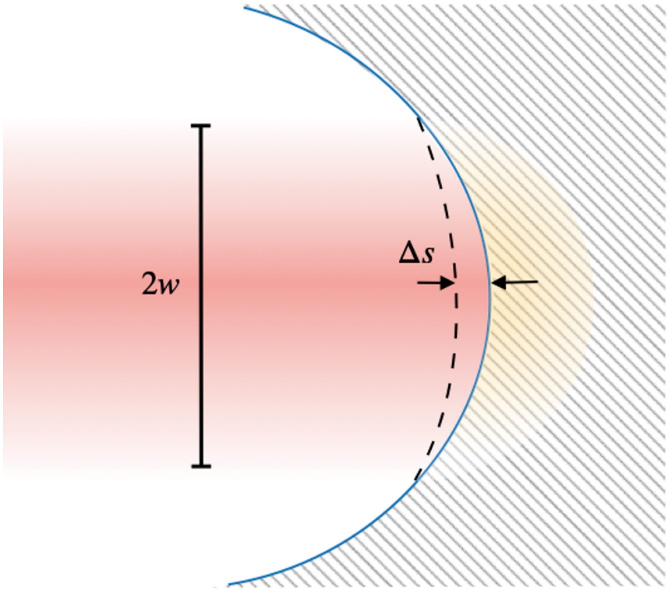

Figure 3.7: Variation of the sagitta Δs due to thermal expansion of the mirror hit by a high-power laser beam.

$$\frac{1}{R'_{\mathrm{ofC}}} \simeq \frac{1}{R_{\mathrm{ofC}}} - \frac{2\Delta s}{w^2} = \frac{1}{R_{\mathrm{ofC}}} - \frac{\alpha P_{\mathrm{ab}}}{2\pi\kappa_{\mathrm{th}} w^2} \tag{3.17}$$

With this model, however, we see the mirror as a large system that responds uniformly to thermal stimulation. Nevertheless, we are also interested in determining local deformations also taking into account possible longitudinal heat flows to the mirror.

In the subsequent part of this section, we focus on the impact of the thermo-elastic and thermo-optic effects on the mirrors of the photodetachment cavity. Our goal is to emulate realistic optics to estimate the actual circulating power and eventually design strategies to mitigate thermal effects. Unlike the analytical models mentioned earlier, the aim is to determine the temperature profile $\Delta T(\mathbf{r})$ and deformation Δs

through simulations to be used in Equation 3.11, considering that Δs corresponds to a profile modification $\Delta l(\mathbf{r})$ of the spherical mirrors. Comparing equations 3.17 and 3.15, we observe their similarity, prompting us to consider the perturbations from both effects as an equivalent deformation applicable to the mirror profile. This deformation will induce an optical path length difference as per equation 3.11, altering the field according to equation 3.9.

3.1.4 Estimation of thermal effects on photodetachment cavity

OSCAR lacks the capability to compute the mirrors temperature and shape changes that stems from the laser action. Therefore, other software tools are required to determine these quantities. In this analysis, I followed a procedure similar to the one outlined by OSCAR's creator, Jérôme Degallaix, in the package manual and in his doctoral thesis [110], from which I replicated certain results to validate the approach of my analyses.

The procedure involves coupling OSCAR with finite element analysis software, such as Ansys, to determine the thermal distribution and deformation to be incorporated as modifications to the mirror refractive index and profile in OSCAR.

The FEM operates on the principle of discretization, where complex structures are divided into smaller, simpler elements that can be analyzed individually. These elements are connected at discrete points called nodes, forming a mesh that represents the entire geometry of the system.

In FEM, each element is characterized by a set of mathematical equations that describe its behavior under various conditions, such as mechanical loading, thermal gradients, or fluid flow. These equations are typically derived from fundamental principles of physics, such as equilibrium equations, constitutive relations, and conservation laws. The behavior of the entire system is then determined by solving these equations iteratively for each element in the mesh. By applying appropriate boundary conditions and material properties, FEM simulations can accurately predict the response of the system to external stimuli.

Assuming moderately impactful deformations, I decided to follow the subsequent iterative method:

1. Determine the nominal circulating power $P_{\mathrm{c},0}$ with $\Delta T(\mathbf{r}), \Delta l(\mathbf{r}) = 0$.
2. Use $P_{\mathrm{c},0}$ to determine the maximum temperature variation $\Delta T_0(\mathbf{r})$ of the mirror and consequently the maximum deformation $\Delta l_0(\mathbf{r})$.
3. Determine the new circulating power $P_{\mathrm{c},1}$ with the deformed hot mirrors.
4. Repeat the process until $P_{\mathrm{c},n} \simeq P_{\mathrm{c},(n-1)}$.

This procedure is designed to address the fact that circulating power and deformations are two correlated variables, and it would be necessary to determine them simultaneously.
The first step for FEM simulation is to define a material. As anticipated, the mirrors are made of low-absorption SiO_2 and its optical, thermal and mechanical characteristics are listed in the table 3.2. Apart from the absorption coefficients, these values were not provided by the company but retrieved from the literature.

Parameter	**Value**	**Unit**
Coating absorption coefficient (A_c)	0.15	ppm
Substrate absorption coefficient (A_{sub})	1	ppm
Substrate thermal expansion coefficient (α)	0.5	$10^{-6}\,K^{-1}$
Thermo-optic coefficient (β)	10	$10^{-6}\,K^{-1}$
Thermal conductivity (κ_{th})	1.38	$W\,m^{-1}\,K^{-1}$
Specific heat (C)	740	$J\,kg^{-1}\,K^{-1}$
Refraction index (n)	1.44	-
Density (ρ)	2200	$kg\,m^{-3}$
Young modulus (E)	73	GPa
Poisson ratio	0.16	-

Table 3.2: Fused Silica parameters at 20°C used in the Ansys-OSCAR simulation to estimate thermal effects. The values come from various sources (Ansys materials database - Granta - and Ref. [110, 111]); A_c and A_{sub} are given on the datasheets of the mirrors.

The chosen geometry is a flat disk with a diameter of one inch: the idea is to evaluate the deformation in the absence of curvature and import it into the actual profile of the curved mirrors. To achieve better resolution with acceptable computational cost, the mirror was divided into two concentric cylinders, and a finer mesh was applied to the central cylinder, which is struck by the laser beam. In Figure 3.8a, the meshed geometry of the mirror is shown. The elements in the central region have a minimum size of 50 µm, while in the peripheral disk, the minimum size is 0.5 mm. The mesh is prismatic and the minimum element quality is about 75% while the average is about 98%.

To estimate the temperature variation, a steady-state thermal analysis was conducted starting from the solid at room temperature of 20°C, assuming radiation from the surfaces to the external environment. Two thermal loads were applied: one representing the internal generation within the mirror, which accounts for the transmitted and partially absorbed beam, and a surface flux representing the thermal power transferred by the intracavity beam.
Both loads were introduced using Ansys Parametric Design Language (APDL) and defined with Gaussian shapes centered on the optical axis: $q(r) = q_0 e^{-\frac{2r^2}{w^2}}$. The amplitude of the applied load in the FEM model, q_0, is calculated with the integral

for a hypothetical mirror of infinite radius

$$P_{\mathrm{ab}} = 2\pi q_0 \int_0^{\infty} e^{-\frac{2r^2}{w^2}}\, r\, dr = \frac{q_0 \pi w^2}{2} \tag{3.18}$$

which allows us to define the load as a function of radius as:

$$q(r) = \frac{2P_{\mathrm{ab}}}{\pi w^2} e^{-\frac{2r^2}{w^2}} \tag{3.19}$$

This load is fine for the heat flow over the HR coating but for the load representing

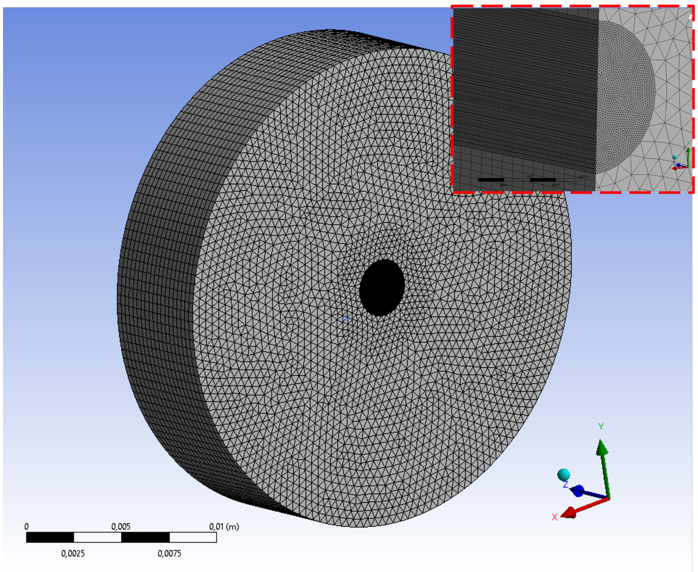

(a) Mirror mesh. The zoom shows the denser mesh near the spot.

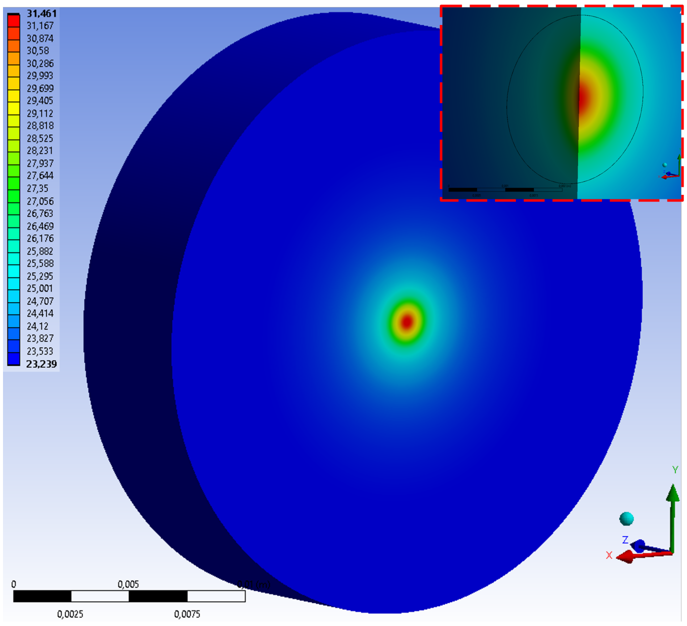

(b) Temperature profile caused by optical power absorption.

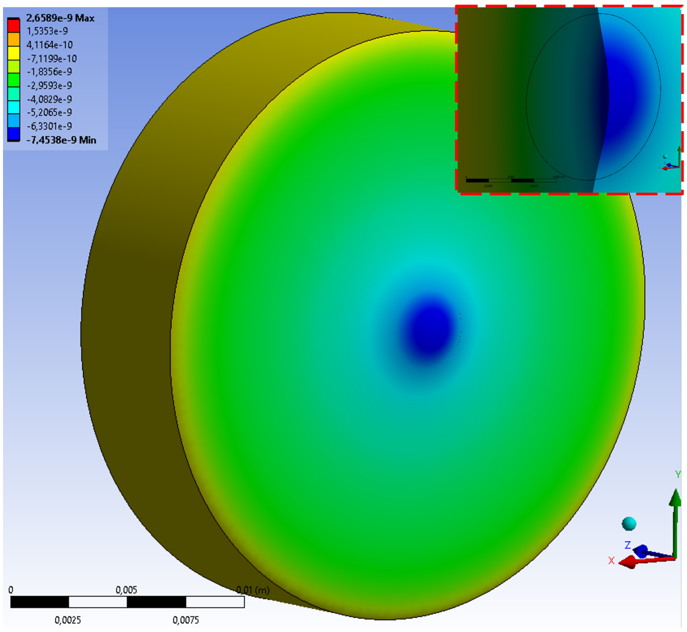

(c) Deformation in axial direction due to mirror heating. The values are negative because the displacement of the nodes is along the negative direction of the z-axis but show an expansion of the mirror.

Figure 3.8: Mesh, temperature profile and mirror deformation resulting from FEM simulation with Ansys. The zoomed-in portion shows the central part of the mirror, which is hit by the laser beam, in section. The circle in the zoom of figures b) and c) delimits the area with a denser mesh. The mirror face shown is the one directed towards the inside of the cavity.

the power transmitted through the mirror, which is modelled as heat generation within the mirror volume, q(r) must be divided by the thickness of the mirror.

In Figure 3.8b, the temperature profile obtained is depicted: as expected, the greatest temperature difference occurs at the HR coating, reaching a peak of approximately 8°C; the heating caused by the power absorbed in the substrate is negligible.

The analysis of thermally induced deformation was performed using the static structural module of Ansys, considering the displacement of nodes along the cavity axis. As boundary conditions, a fixed circular constraint was applied around the mirror, representing a support capable of uniformly enveloping the mirror.

It is worth noting that this system geometry justifies the inclusion of the Poisson's ratio among the key parameters governing its thermoelastic deformation. Indeed, the Poisson's ratio describes how a material, when stretched or compressed in one direction, contracts or expands in the perpendicular directions. In thermoelasticity, which combines mechanical and thermal effects, this ratio is essential for understanding how a material responds when subjected to both temperature changes and external loads. If a material is constrained or restricted in certain directions, thermal expansion in one direction may induce deformations in other directions, governed

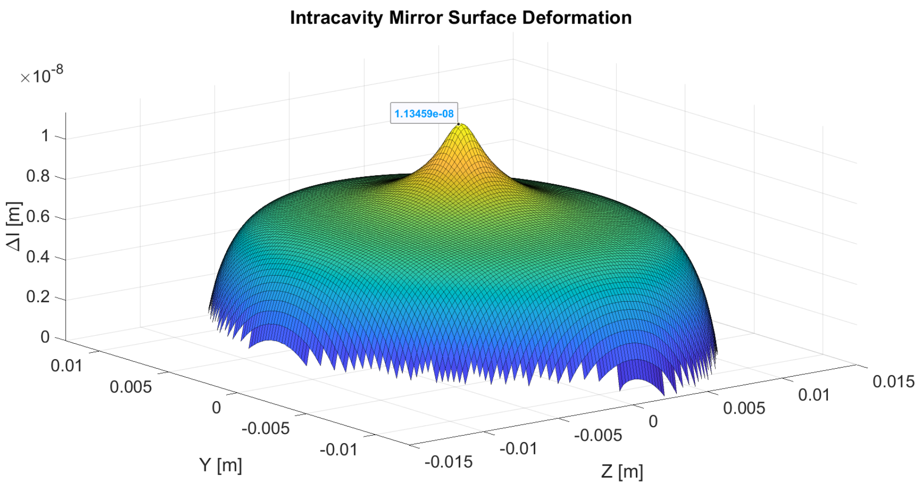

(a) Axial deformation of the mirror surface inside the cavity.

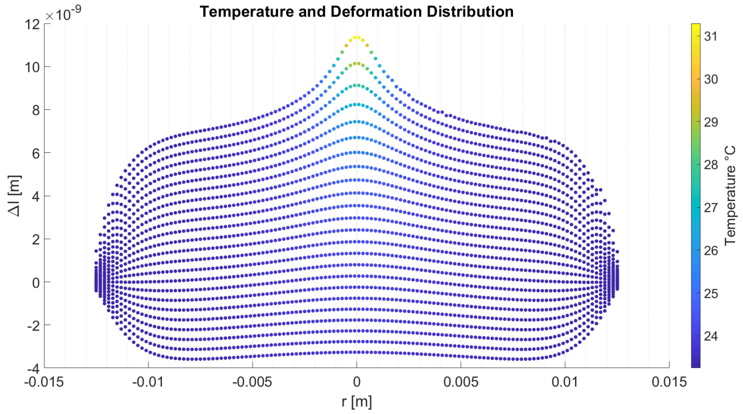

(b) Axial deformation and temperature profile of the mirror. Each curve represents a different layer of the mirror: the highest layer is the one that faces the inside of the optical cavity.

Figure 3.9: Deformation profiles and mirror temperature in cavity with maximum circulating power.

by Poisson's ratio.

In Figure 3.8c, the obtained results are presented: there is an expansion affecting the entire mirror, with a peak occurring at the location of the highest power absorbed by the coating.

These results were imported into MATLAB, interpolated and extrapolated to match the grid used in OSCAR. The results are shown in Figure 3.9.

The deformation, ideally having circular symmetry, has a peak of about 11 nm and involves the entire surface of the mirror. In Figure 3.9b the deformation and temperature profiles for different radial sections of the mirror are shown. Note that in these figures, the deformation is applied to a flat mirror, as it would be imperceptible with a curved mirror. Although the deformation is several orders of magnitude lower than the sag of the entire mirror (on the order of 30 μm for a mirror with a radius of 2 m), this can be relevant when considering the sag defined

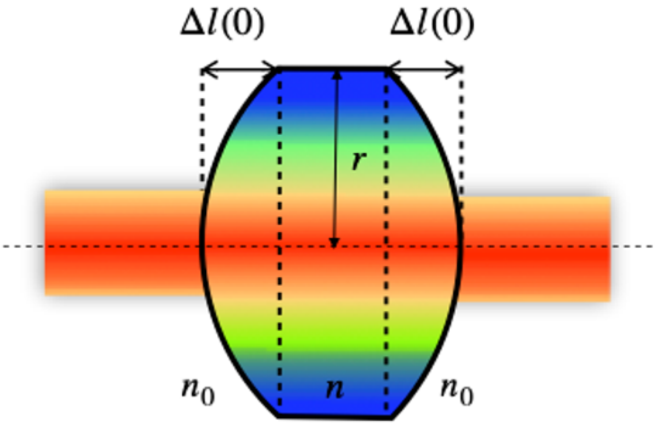

Figure 3.10: Representation of the model used to evaluate the thermo-elastic effect starting from a flat mirror. The beam passing through the mirror encounters the deformed region, experiencing a change in refractive index during the length of the deformation, for both sides of the mirror.

by the laser waist (as in the Figure 3.7), which in this case is approximately 0.6 μm. Given the inverse proportionality between waist and radius of curvature, the problem of deformation may become more important for large radii of curvature. We can define the cumulative optical path difference resulting from thermo-elastic and thermo-optic effects experienced by the transmitted field through the mirror, based on the discretized form of equation 3.11:

$$\Delta\mathrm{OPL_t}(y,z) = \beta \int_0^l \Delta T(x,y,z)dx + (n-n_0)\Delta l_{\mathrm{tot}}(y,z) \tag{3.20}$$

with n and n_0 being the refractive indices of the mirror and air, respectively. The second term in the equation arises from the fact that when the field approaches the mirror, it encounters its profile earlier and leaves it later compared to the case of a cold mirror by an amount equal to Δl. This can be better understood by looking at Figure 3.10, where the cold mirror is schematized with two flat surfaces for simplicity. Looking at the Figure 3.11a, it can be seen that the maximum $\Delta\mathrm{OPL_t}$ is of the order of 0.1 μm and is zero at the centre, where the temperature is maximum, and negative in the rest of the mirror where the temperature decreases with the radius.
In Figure 3.11b the contributions of the thermo-optic and thermo-elastic effect to ΔOPL of the equation 3.20 are shown separately: it can be seen that the thermo-optic effect is dominant and is about one order of magnitude higher then the thermo-elastic effect; this happens due to the relatively high ratio β/k_{th} of the fused silica [110].
Once in the cavity, the field only interacts with the HR surfaces of the mirrors deformed by the thermo-elastic effect. Assuming they are deformed in the same

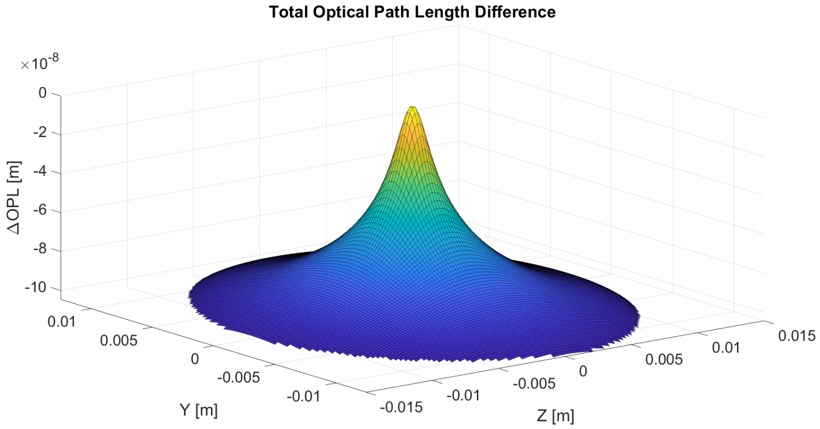

(a) Total optical path difference for a field passing through the heated mirror.

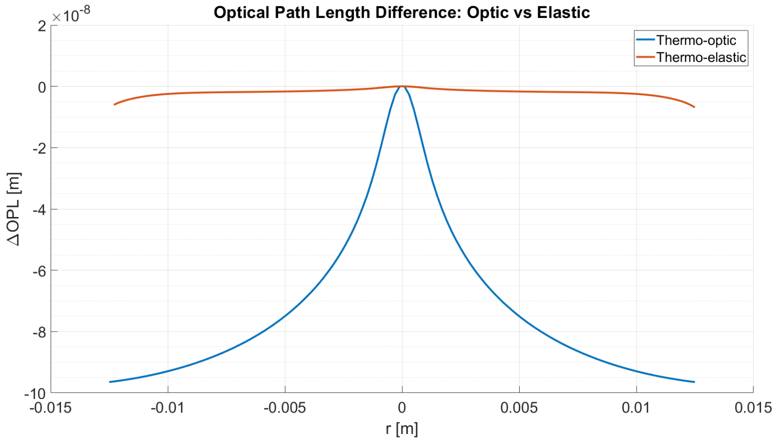

(b) Contributions of thermo-optic and thermo-elastic effects presented separately and as a function of radial coordinate.

Figure 3.11: Optical path difference of cavity mirrors for photodetachment.

way, the optical path difference of the circulating field is given by:

$$\Delta \mathrm{OPL}_{\mathrm{r}}(y, z) = 2\Delta l(y, z) \tag{3.21}$$

By modifying the cold mirror profile defined in OSCAR with the deformation and optical path difference obtained, the powers shown in table 3.3 are obtained. While the coupling obtained is slightly worse than in the cold cavity as expected, the circulating power is slightly higher than the design value (see Table 3.1). In Figure 3.12, the circulating powers are shown as a function of the variation in mirror thickness relative to the laser wavelength. By slightly varying the mirror thickness, we can observe how the circulating power contrast caused by etalon changes for both the cold and hot cavities. The etalon effect is generally stronger when the mirrors are two parallel flat surfaces; thus, one hypothesis for this behaviour is that deformations reduce the differences between the HR and AR surfaces of the mirror. This hypothesis accords with the fact that inside the cavity, where the cold mirror is

Table 3.3: Powers relative to the heated cavity

Parameter	**Value**
Power in the input beam	15 W
Circulating power	197.9 kW
Transmitted power	14.89 W
Reflected power	0.05 W

concave, there is greater deformation due to intracavity power. The values reported in Tables 3.3 and 3.1 correspond to the condition of maximum power for the cold cavity.
We will not delve deeply into the reasons of these power values since our interest lies in the qualitative but important result: $P_{\mathrm{c},1} \simeq P_{\mathrm{c},0}$. This concludes our analysis, validating the operational power as the design power, which is approximately 198 kW.

However, if needed, various strategies have can be applied to counterbalance the thermal effect. Among the main ones are the heating ring, the compensation plate and the CO_2 laser projectors [110–117]. The ring heater is a thermal compensation system employed to counteract the alteration in the curvature radius caused by laser heating on the optic's surface. It is part of a set of thermal compensation systems integrated into the detectors to mitigate aberrations. The ring radiatively heats the outer edge of each test mass, thereby reducing the temperature gradient within them. By applying additional heat at the periphery, the radial profile of absorption is flattened, counterbalancing the centrally concentrated beam heating and alleviating the radial component of the thermal gradient. However, this adjustment leads to a rise in the mean temperature of the optic. In scenarios involving high optical power, adaptive compensation can be achieved by regulating the electrical power supplied to one or more heating elements positioned around the optic's perimeter. Compensation plates (CP) are vital components of a thermal compensation system and consist of optical plates (often made of fused silica) that the beam passes through before entering the high-power optical cavity. The CPs aim to deform the laser beam wavefront to compensate for the distortion created by the optical effect of the cavity's output coupler. CPs require active heating, typically achieved through ring heaters (RH) or other means such as CO_2 laser projectors. These projectors emit laser beams with wavelengths in a high-absorption region of the optical material used, with the intention of heating the CPs in a circular area around the impact zone of the main Gaussian beam. The shape of the projector beams can be achieved using axicon lenses, which can be combined to create multiple concentric circles.

While these strategies are commonly employed in large-scale, high-power systems such as gravitational wave detectors, they could be scaled down and adapted for a more compact system like the one described in this work. If necessary, this could

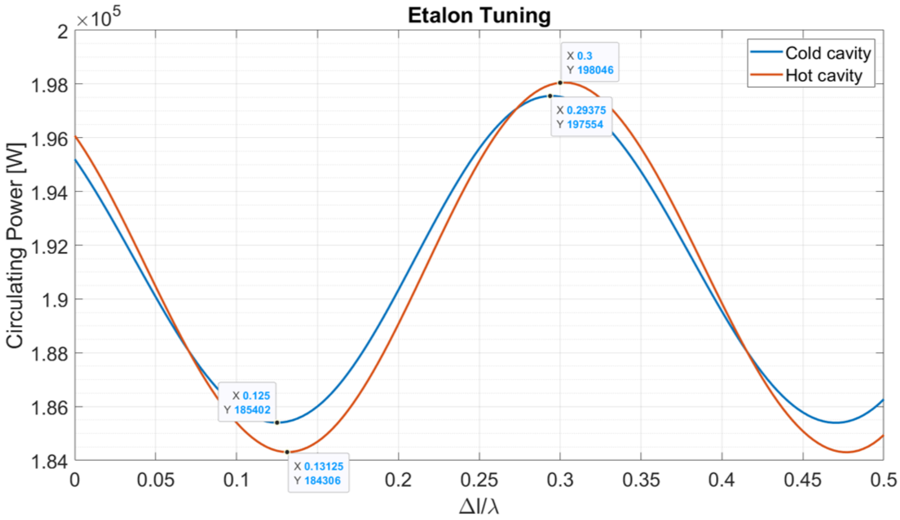

Figure 3.12: Circulating power as a function of a small change in mirror thickness: the hot cavity has a higher contrast probably because the asymmetry of the mirror surfaces could be reduced by thermal effect, slightly increasing the etalon effect.

represent a future development of the experimental work that we will describe in Section 3.3.

3.2 Photodetachment process simulation

We aim to estimate the photodetachment probability and its effects on the atomic beam kinematics starting from an uncollimated beam. The position and velocity distributions have been estimated by the research group responsible for the focusing apparatus and are reported in [49]. The article provides estimates of the Ps^- distributions for two different converter temperatures, 10 K and 300 K. In this study, we will only consider the condition at 300 K, which has a more detrimental effect on the beam. The resulting spatial and angular distributions are Gaussian with zero mean (centred at the focal point of the laser beam) and standard deviation of approximately 0.2 mm and 5 mrad for both y and x. The angle are defined as $\theta_y = \arctan(v_y/v_z)$, $\theta_x = \arctan(v_x/v_z)$, with $v_{x,y,z}$ initial velocity components of the ions. Also v_z has a Gaussian distribution with a mean about 6×10^6 m/s and a standard deviation of about 5×10^3 m/s.
To estimate the probability of a Ps^- ion undergoing photodetachment, we start by modifying equation 3.1, which defines the photodetachment probability. Specifically, we can modify the expression of the laser intensity by considering the average intensity between two points, P_1 and P_2, as $I(t) = \int_{P_1}^{P_2} I(s,t)ds/\overline{P_1P_2}$, and express the probability as follows:

$$P_{\text{pd}} = 1 - \exp\left(-\frac{\lambda\sigma}{hc\overline{P_1P_2}}\int_{t_1}^{t_2}\int_{P_1}^{P_2} I(s,t)\,dsdt\right) \tag{3.22}$$

In this equation, the intensity and the time-space intervals of the laser-ion interaction remain to be defined, varying for each ion based on its position and velocity.

A standing wave in a cavity is a solution of the Helmholtz equation. Each solution of the equation represents a different mode of the cavity. We are interested in the fundamental mode (TEM_{00}), which has a Gaussian shape and concentrates all the power of the laser beam into a single central spot.
A standing wave is also the superposition of two traveling waves in the cavity, which we assume to be two TEM_{00} modes propagating in opposite directions, one parallel to x and the other antiparallel to x.
The electric field of the waves is given by $E_{1,2}(x,y,z,t) = E_{1,2}(x,y,z)e^{-i\omega t}$, where $E_{1,2}(x,y,z)$ is expressed as:

$$E_{1,2}(x,y,z) = \hat{e}E_0\frac{w_0}{w(x)}e^{\frac{-r^2}{w(x)^2}}e^{\mp i\left(kx+\frac{kr^2}{2R(x)}-\phi(x)\right)}$$

Here, $\hat{e}$ represents the polarization vector of the field, w_0 is the nominal waist at the focal point, $w(x) = w_0\sqrt{1+\left(\frac{x-X}{x_R}\right)^2}$, x_R is the Rayleigh length, $r = (y-Y)^2 + (z-Z)^2$, and X,Y and Z are the coordinates of the beam center (focal point), $R(x)$ is the radius of curvature of the wavefront, and $\phi(x)$ represents the Gouy phase. The spatial parity of w, R, and ϕ was exploited in the definition of the two fields. Calculating the total field $E_\mathrm{T} = E_1 + E_2$ and considering that $I = \epsilon_0 c|E_\mathrm{T}|^2/2$ we obtain:

$$I(r,t) = 2\hat{e}I_0\left(\frac{w_0}{w(x)}\right)^2 e^{\frac{-2r^2}{w(x)^2}}\left[1+\cos\left(2kx+\frac{kr^2}{R(x)}-2\phi(x)\right)\right] \tag{3.23}$$

with $I_0 = \epsilon_0 c E_0^2/2$. From the definition of the Rayleigh length in vacuum, $x_R = \frac{\pi w_0^2}{\lambda}$, and considering the region of our interest (within about half a millimetre of the waist) we can make the following reasonable approximations: $w(x) \simeq w_0$, $R(x) \simeq \infty$, $\phi(x) \simeq 0$. The intensity to be applied in the equation 3.22 then becomes:

$$I(x,y,z) = 4I_0 e^{\frac{-2r^2}{w_0^2}}\cos^2(kx) \tag{3.24}$$

The spatial and temporal integration limits clearly depend on the chosen geometries and the dimensionality of the region where the photodetachment probability is to be estimated. This section aims to describe the algorithm to be applied subsequently to Monte Carlo simulations. For better clarity, we will divide the algorithm into two successive models. Both models assume that Ps^- ions move along trajectories that can be well represented by straight lines. In the first model, the possibility that an ion may undergo photodetachment before the end of its trajectory will not be considered. Instead, the photodetachment probability accumulated along its path

through the laser, which can be schematized as an infinite cylinder, will be calculated. In the second model, the photodetachment probability will be calculated in small independent cubic regions, allowing a Monte Carlo model to also determine the random position where photodetachment occurs. Note that if we want to determine the shape of the beam immediately after the photodetachment, it is necessary to trace all the trajectories of the Ps atoms, which means to determine the position where the photodetachment occurred. This analysis becomes necessary when integrating different systems such as photodetachment, Ps excitation and interferometer, and geometric and kinematic factors become non-negligible. Although we will only apply it to photodetachament here, the aim behind this model is to set up a front-to-end simulation of the entire experiment.
Regardless of the chosen geometry, the idea is to integrate the intensity along the trajectory followed by the ion within the selected spatial region and divide the result by the length of the ion's path within that region. This yields the average value of the intensity with which the Ps^- interacted along its path. This average value is then inserted into formula 3.22 to obtain the photodetachment probability. Formally, the integral is therefore a line integral along the ion's trajectory, bounded by the points of intersection between it and the selected spatial region.

3.2.1 3-D model with cylindrical spatial integration region

In this model, we estimate the photodetachment probability that an ion accumulates while traversing the entire outer cylinder with a radius of $w_0' = 2.5$ mm, defined by the distance between the source exit electrode and the center of the laser (see Section 3.1.2). The spatial integration limits are the entry and exit points (P_1 and P_2) of the ion from this cylinder, i.e., the points of intersection between the Ps^- trajectory and the cylinder. Since the intensity is not time-dependent (see equation 3.24), its integral over time is simply a multiplication by the time interval Δt that the ion spends inside the cylinder: $\Delta t = \overline{P_1P_2}/|\mathbf{v}|$. Reasonably considering the trajectory of each ion as a straight line from the point $P_0 = (x_0, y_0, 0)$ with respect to a reference system centred on the acceleration grid, to determine the intersection points between the trajectory and the laser cylinder we need to solve the cylinder equation $(y' - Y)^2 + (z - Z)^2 = w_0'^2$, where the generic spatial coordinates of an ion have been parameterised in z: $(x, y, z) \to (x', y', z) = (x_0 + m_x z, y_0 + m_y z, z)$ with m_x and m_y angular coefficients of the line along the x and y axes. The solution of the equation allows us to obtain the $z_{1,2}$ coordinates of the intersection points P_1

and P_2:

$$\begin{gathered}z_{1,2}=\frac{m_y(Y-y_0)+Z\pm\sqrt{(m_y^2+1)w_0'^2-(m_yZ-Y+y_0)^2}}{m_y^2+1}\\P_1=(x_0+m_xz_1,y_0+m_yz_1,z_1)\\P_2=(x_0+m_xz_2,y_0+m_yz_2,z_2)\end{gathered}\tag{3.25}$$

To be able to use these results, it is also necessary to parameterise the intensity function, which becomes:

$$I(x',y',z)=4I_0\exp\left\{-2\frac{(y_0+m_yz-Y)^2+(z-Z)^2}{w_0^2}\right\}\cos^2\left[k(x_0+m_xz)\right]\tag{3.26}$$

In order to integrate this function, one must take care to multiply it by the square root of the sum of the square of the derivatives in z of the new coordinates:

$$\begin{aligned}\int I(s)ds&=\int_{z_1}^{z_2}I(x',y',z)\sqrt{\left(\frac{dx'}{dz}\right)^2+\left(\frac{dy'}{dz}\right)^2+1}\,dz\\&=\int_{z_1}^{z_2}I(x',y',z)\sqrt{m_x^2+m_y^2+1}\,dz\end{aligned}\tag{3.27}$$

This integral has to be estimated for any trajectory. Note that the equation 3.27 is valid for any geometry in the chosen integration region. However, when moving from one geometry to another, it is necessary to modify the equation 3.25 to determine the coordinates of the two extremes of spatial integration. If, on the other hand, you wish to change the shape of the trajectories (e.g. if you insert electrodes that accelerate ions), you only need to change the functions x' and y'. As previously mentioned, the temporal integration involves multiplying the intensity by a time interval Δt defined by the intersection points P_1 and P_2. However, since the Ps$^-$ ion has a finite lifetime and a velocity distribution with nonzero dispersion, it may happen that the ion dies before reaching the laser cylinder, or inside it, or that its trajectory does not intersect the cylinder (see Figure 3.13). Upon exiting the converter, each ion is assigned a lifetime randomly sampled from a negative exponential distribution with the mean lifetime as the time constant. If the trajectory does not intersect the cylinder, Equation 3.25 has no real solutions, and the ion in question is assigned a zero photodetachment probability.For all other trajectories, it is necessary to verify that the distance traveled after the exit electrode and before dying, $\Delta s_{\max}$, is greater than the distance between P_1 or P_2 and the electrode:

a) If $\Delta s_{\max} < P_1$, the ion dies before reaching the laser and automatically has a null photodetachment probability.

b) If $P_1 \leq \Delta s_{\max} < P_2$, the ion dies inside the laser.

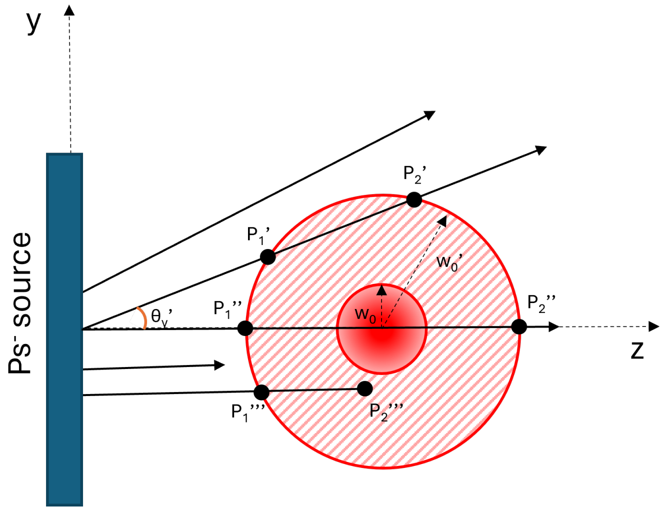

Figure 3.13: Possible intersections between the Ps^- ions trajectories and the computational domain, delimited by the cylinder of radius w_0'. For a more general and clear representation, w_0' in this figure does not coincide with Δz_o of section 3.1.2

c) If $\Delta s_{\max} > P_2$, the ion surpasses the entire cylinder, and its photodetachment probability is maximum relative to its trajectory.

In case b) it is necessary to recalculate the second integration extremum P_2' since $\overline{P_1P_2'} < \overline{P_1P_2}$. The equation to be used to determine the new coordinate z_2, valid in the case of cylindrical geometry, is:

$$z_2 = \frac{|\mathbf{v}|(\tau_\mathrm{r} - t_1)}{\sqrt{m_x^2 + m_y^2 + 1}} + z_1 \tag{3.28}$$

where τ_r is the residual lifetime the ion has when it reaches the exit electrode, and t_1 is the time it takes to reach the first point of intersection with the cylinder, $t_1 = \overline{P_0P_1}/|\mathbf{v}|$. Then, as before, to obtain the new x- and y-coordinates of P_2' just replace z_2 in x' and y'. As for the time integration of case b), the new integration interval is $\Delta t' = \tau_\mathrm{r} - t_1 = \overline{P_1P_2'}/|\mathbf{v}|$.

We define the total cumulative photodetachment probability, $P_{\mathrm{pd,Tot}}$, as the probability that an ion accumulates along its entire path inside the laser assuming that its lifetime is greater than the time it takes to traverse the entire cylinder. Since in this model the region chosen for integration coincides with the laser cylinder, $P_{\mathrm{pd,Tot}}$ can be calculated with the equation 3.22. We will use the average of the total cumulative photodetachment probabilities of the ions, $\bar{P}_{\mathrm{pd,Tot}}$, to estimate the photodetachment probability of the system by Monte Carlo simulation. Another indicator is the average photodetachment probability, $P_{\mathrm{pd,m}}$, calculated as the ratio of the number of ions photodetaching to the total number of ions entering the laser. where the number or photodetached ion is estimated by comparing $P_{\mathrm{pd,Tot}}$ with a random number ranging from 0 to 1. It is expected that for a specific trajectory,

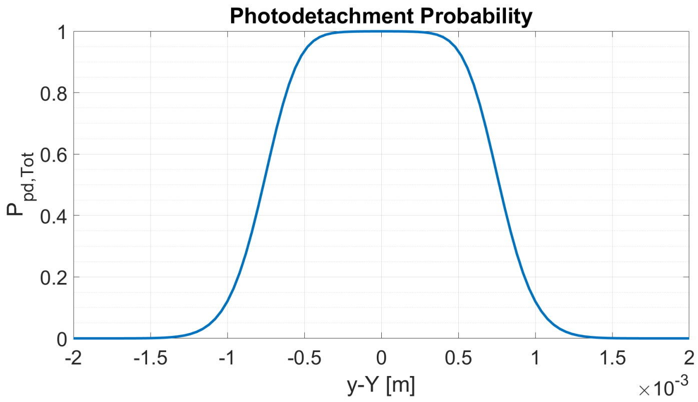

(a) Probability of an ion passing through the laser beam at different distances from the optical axis.

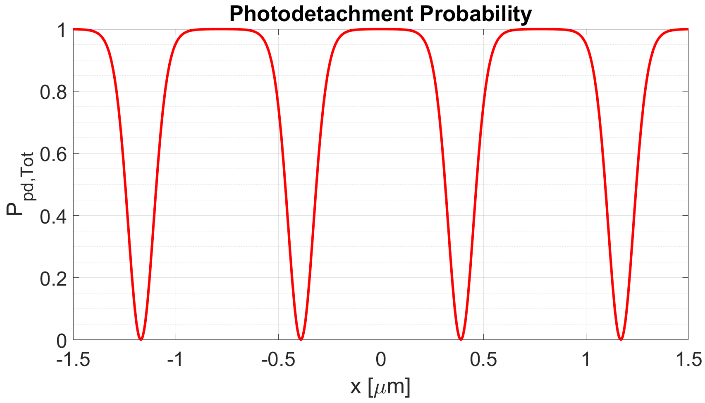

(b) Probability of an ion passing through the laser beam at different positions along the optical axis.

Figure 3.14: Behaviour of the accumulated photodetachment probability along a transverse plane and a longitudinal plane with respect to the optical axis.

$P_{\text{pd,m}}$ tends to $\bar{P}_{\text{pd,Tot}}$ for a sufficiently large number of ions traveling through that trajectory.

By setting the angular coefficients to 0 and by varying the x_0 or y_0 co-ordinate, it is possible to probe $P_{\text{pd,Tot}}$ along the x- and y-direction respectively and obtain the graphs in Figure 3.14a and 3.14b.

The trend in Figure 3.14a has a Gaussian-like shape and is instead obtained by dissecting the laser cylinder in the yz plane. The trend of the graph in Figure 3.14b is clearly due to the function $\cos^2(kx)$ modulating the probability along the laser axis. Note that the peak probability is higher compared to the estimated circulating power required in Equation 3.2 because here the intensity corresponds to the stationary cavity defined by Equation 3.24, which yields $I = 4I_0$ for r and x equal to zero. These results were obtained by imposing a life time of Ps$^-$ much greater than the time required to travel the entire cylinder, and do not take into account any distribution (initial positions, angular coefficients and velocities) for which we refer to the Monte Carlo simulation. The maximum total probability that can be accumulated by an ion if it moves with an energy of 200 eV and interacts with the circulating power in table 3.1 is approximately 99%.

3.2.2 3-D model with cubic spatial mesh

This 3D model essentially involves determining the photodetachment probability within cubic regions of space intersected by the trajectories of each ion. The idea is to define the intersection points between the ion trajectory and the k-th cube to obtain the spatial and temporal integration limits and apply Equation 3.27. It should be noted that in the general case, where at least one of the angular coefficients m_x and m_y is nonzero, the trajectory segment delimited by the intersection points is different in each cube. This implies that the intersection points, and thus the integral in Equation 3.27 and the time interval to be inserted in Equation 3.22, need to be calculated for each cube.

We can address this issue with an iterative algorithm that determines the second intersection point of the k-th interaction ($\mathrm{P}_{2,k}$) based on the angular coefficients and the first intersection point ($\mathrm{P}_{1,k}$) of each ion. In the subsequent interaction, the second intersection point becomes the first: $\mathrm{P}_{1,k+1}$=$\mathrm{P}_{2,k}$ (see Figure 3.15). Iterations continue until at least one of the following events occurs:

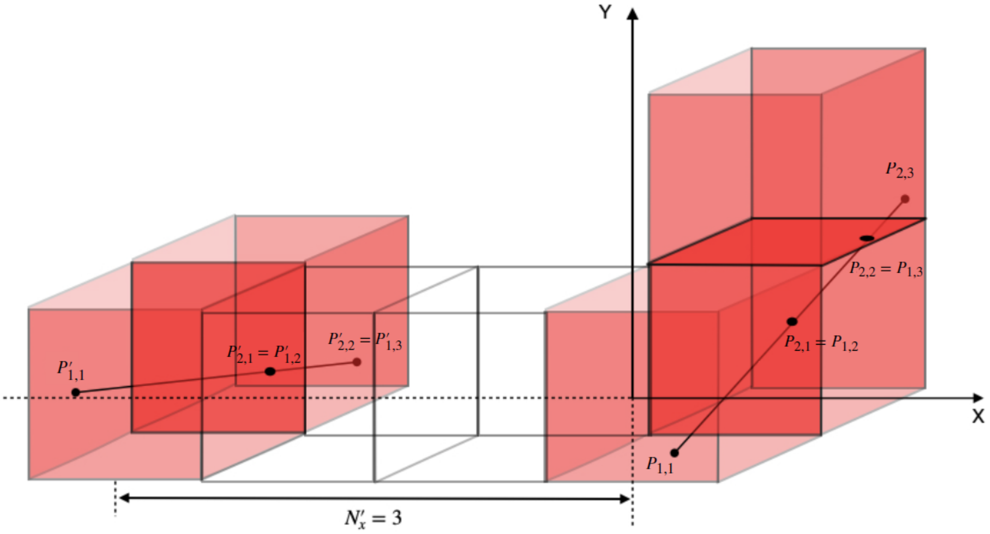

Figure 3.15: Schematic representation of the cubic geometry model. The trajectories of two ions are depicted by two straight lines originating from points $P_{1,1}$ and $P'_{1,1}$. Unlike $P_{1,1}$, point $P'_{1,1}$ is not located within the cube that includes the origin of the axes; therefore, the corresponding initial value of the coefficient N_x is not zero (equal to 3 in the example shown in the figure).

a) The ion undergoes photodetachment;

b) The elapsed time, Δt_{tot}, exceeds the residual lifetime τ_{r};

c) The ion surpasses the laser beam and reaches the end of the computational domain.

The extremes of spatial integration are defined by the points of intersection between a line and one of the faces of the k-th cube. Given therefore the angular coefficients of the line and the point $P_{1,k}$, one must determine which face of the cube is closest to $P_{1,k}$ along the ion's trajectory. This problem is solved by determining which of the following expressions returns the smallest positive value:

$$\left[\frac{\pm l_\mathrm{c}/2 - x_{1,k}}{m_x}, \frac{\pm l_\mathrm{c}/2 - y_{1,k}}{m_y}, \frac{l_\mathrm{c}}{2} - z_{1,k}\right] \tag{3.29}$$

with $x_{1,k}$, $y_{1,k}$, $z_{1,k}$ the coordinates of the k-th cube's first point of intersection and l_c the length of the sides of the cube. If the minimum positive is one of the first two expressions, the trajectory intersects one of the two faces of the cube parallel to the yz plane. If the it is one of the third and fourth expressions, the trajectory intersects one of the two faces of the cube parallel to the xz plane. If the last expression returns the lower value, the trajectory intersects the second face of the cube parallel to the xy plane. However, assuming that $P_{1,1}$ is centred with respect to the first cube in the x- and y-axes, these expressions are only valid for the first iteration, and to generalise them it is necessary to introduce correction factors to take into account the fact that the distance the ion must travel in each direction to intersect a face of the cube is in general different in each iteration:

$$\left[\frac{\pm l_\mathrm{c}(N_x+1) - x_{1,k}}{m_x}, \frac{\pm l_\mathrm{c}(N_y+1) - y_{1,k}}{m_y}, l_\mathrm{c}(N_z+1) - z_{1,k}\right] \tag{3.30}$$

where N_x, N_y, N_z are the number of times a face parallel to the yz, xz or xy plane is intersected respectively. For the algorithm to work correctly, one of N_x, N_y, N_z must be incremented at each iteration after determining which face is intersected by the ion. Since the coordinates $x_{1,k}$ and $y_{1,k}$ of the initial point $P_{1,1}$ are not necessarily zero, the initial values of N_x and N_y may not be 0. Therefore, it is necessary to compute the two correction factors before entering the first interaction (see Figure 3.15). The expressions 3.30 also allow determining the coordinates of the second intersection point $P_{2,k}$ at each interaction. Specifically, the coordinate $z_{2,k}$ is defined by the expression that yields the smaller positive value, except for the expression corresponding to the face parallel to the xy-plane, which must be multiplied by the cosine of the angle between the dominant direction and the z-axis:

$$z_{2,k} = \min_{\mathbb{R}^+} \begin{bmatrix} \frac{\pm l_\mathrm{c}(N_x+1) - x_{1,k}}{m_x}\cos(\theta_x) + z_{1,k} \\ \frac{\pm l_\mathrm{c}(N_y+1) - y_{1,k}}{m_y}\cos(\theta_y) + z_{1,k} \\ l_\mathrm{c}(N_z+1) \end{bmatrix} \tag{3.31}$$

with $\theta_{x,y} = \arctan(m_{x,y})$. The second intersection point is defined by $[x_{2,k}, y_{2,k}, z_{2,k}] =$

$[x_{1,k} + m_x(z_{2,k} - z_{1,k}), y_{1,k} + m_y(z_{2,k} - z_{1,k}), z_{2,k}]$ and in the subsequent interaction we have $P_{1,(k+1)} = P_{2,k}$. Similarly to the previous method, $\Delta t_k = \overline{P_{1,k}P_{2,k}}/|\mathbf{v}|$ e $\Delta t_{\text{tot}} = \sum_{k=1}^{K} \Delta t_k$.

Equation 3.22 is used in this model to compute the photodetachment probability in a single cube, but it does not yield either the average probability, $P_{\text{ph,m}}$, or the total cumulative photodetachment probability, $P_{\text{pd,Tot}}$. As mentioned earlier, one way to obtain $P_{\text{ph,m}}$ is by evaluating the ratio of the number of ions undergoing photodetachment to the total number of ions entering the laser. It is possible to identify the cube where an ion undergoes photodetachment by comparing a randomly generated number with the photodetachment probability in that cube. This will be used to evaluate the beam kinetics in the Monte Carlo simulation and the photodetachment probability with annihilation. Since $P_{\text{ph,m}}$ tends towards $\bar{P}_{\text{ph,Tot}}$ for a large number of ions, it is preferable to use the total probability for estimating the system's photodetachment probability in order to reduce computational time. This option is valid provided that conditions a) and b) from Section 3.2 are neglected (each ion must pass through the laser completely). In this model, the total photodetachment probability of an ion is defined by:

$$P_{\text{ph,Tot}} = 1 - \exp\left\{ -\frac{\lambda\sigma}{hc} \sum_{k=1}^{K} \left[\frac{\Delta t_k}{(z_{2,k} - z_{1,k})} \int_{z_{2,k}}^{z_{1,k}} I \, dz \right] \right\} \tag{3.32}$$

where the integral is computed in each cube using Equation 3.27. By averaging $P_{ph,Tot}$ over all ions, one obtains $\bar{P}_{\text{ph,Tot}}$. It should be noted that the sum of the probabilities of all cubes intersected by an ion's trajectory does not correspond to the total photodetachment probability of the ion, as generally:

$$\sum_{k=1}^{K} \left[1 - \exp\left\{ -\frac{\lambda\sigma}{hc} \frac{\Delta t_k}{(z_{2,k} - z_{1,k})} \int_{z_{2,k}}^{z_{1,k}} I \, dz \right\} \right] \neq P_{\text{ph,Tot}}$$

with K being the number of cubes intersected by the ion's trajectory. The equality is valid for $K = 1$, which means integrating the intensity over a single large cube with a side length equal to the difference between the z coordinates of the two intersection points between the ion's trajectory and the laser cylinder (which is essentially the previous cylindrical geometry model). This multiple cubic geometry method yields the same results as the cylindrical geometry one, and by setting the algorithm as in Section 3.2.1, the same trend as in the Figure 3.14 is obtained.

3.2.3 Monte Carlo simulation

Applying the model described in section 3.2.2 and the distributions presented in section 3.2 ($\mu_{x,y} = 0$, $\sigma_{x,y} \simeq 0.2\,\text{mm}$, $\mu_{\theta_{x,y}} = 0$, $\sigma_{\theta_{x,y}} \simeq 5\,\text{mrad}$, $\mu_{v_z} = 6 \times 10^6\,\text{m/s}$, $\sigma_{v_z} \simeq 5 \times 10^3\,\text{m/s}$), we obtain an average total cumulative probability in the absence of annihilation $\bar{P}_{\mathrm{pd,Tot}} \simeq 95\%$. Annihilation from the last acceleration grid affects about 50% and the resulting average photodetachment probability is $P_{\mathrm{pd,m}} \simeq 47\%$ on a sample of about 6×10^5 ions. A qualitative image of the Monte Carlo simulation is shown in the Figure 3.16.

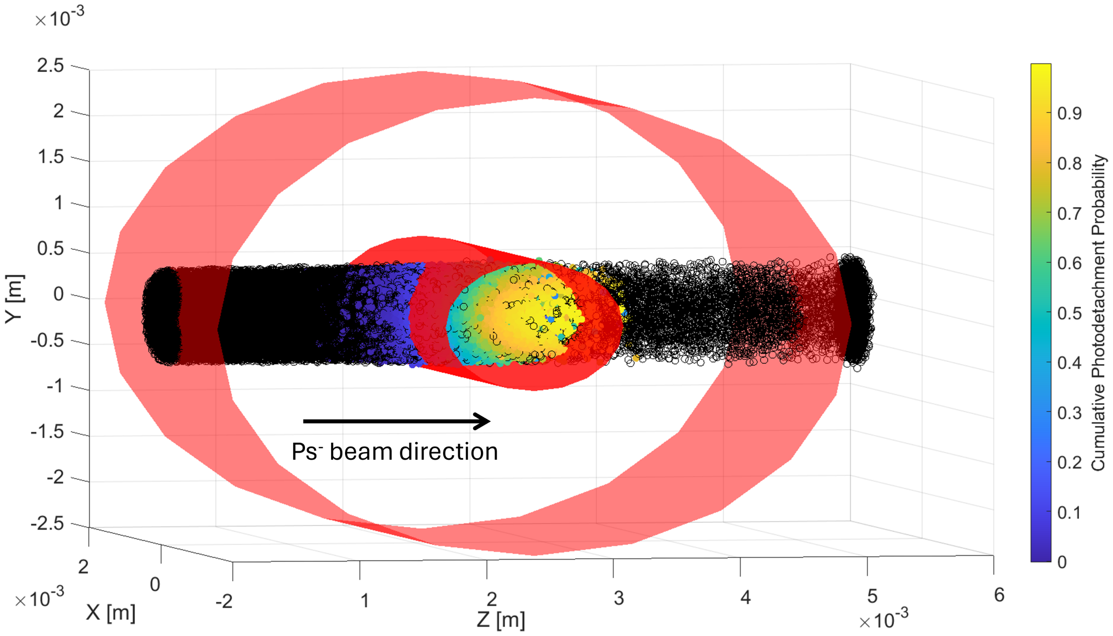

Figure 3.16: 3D representation of the Monte Carlo simulation of the Ps^- photodetachent. The cylinder with the larger diameter delimits the effective mirror area while the smaller cylinder, which has a radius equal to the waist w_0, represents the laser beam. The coloured spheres represent the ions that have photodetached and the colour encodes the accumulated photodetachment probability until the process occurs. The empty spheres represent the ions annihilated without photodetachment.

Ps^- is excited by absorbing a photon and de-excited by losing an electron. Part of the energy of the absorbed photon is used to break the bond with the electron (threshold energy $E_{\mathrm{th}} = 0.326$ eV), while the remaining part is distributed between the electron and the Ps. This process considers both the recoil due to photon absorption and the recoil from electron separation. The magnitude of the Ps velocity change due to the first recoil is given by $\Delta v_{\mathrm{ex}} = \frac{\hbar k}{3m_e}$, where m_e is the electron mass. The Ps recoil from the separation of two bodies depends on the amount of residual energy after bond breaking and thus on the wavelength of the incident photon: $\Delta v_{\mathrm{det}} = \sqrt{\frac{E_{\mathrm{pd}} - E_{\mathrm{Th}}}{3m_e}}$, where $E_{\mathrm{pd}} = hc/\lambda$.

For the wavelength considered so far for photodetachement (1560 nm), we have $E_{\mathrm{pd}} \simeq 0.8$ eV and thus $\Delta v_{\mathrm{det}} \simeq 1.66 \times 10^5$ m/s and $\Delta v_{\mathrm{ex}} \simeq 155$ m/s. The angular variations due to recoil and absorption are therefore approximately 28 mrad and 0.03 mrad, respectively. Comparing these values to the initial distribution ($\sigma_\theta \simeq 5$ mrad), we observe that the effect of absorption is negligible, while recoil can be destructive.

A crucial point is that the probability of emission is not isotropic but depends on the laser electric field polarization direction: the detached electron is emitted along a direction rotated by an angle α to the direction of the electric field. α follows a $\cos^2$ distribution so the most likely direction will be along the electric field [118]. This result stems from the theory of Photoelectron Angular Distributions (PAD), which defines patterns of electron emission distributions following photodetachment events based on the electronic structure of the atom under consideration. This theory, which can also be treated semiclassically, defines a general emission distribution considering cases where the atomic reference frame and the laboratory frame are different (unpolarized atom), and where the angles are the Euler angles describing the mutual rotation of the two systems:

$$I(\theta_s, \phi_s) = \int_0^{2\pi} d\phi \int_0^{\pi} \sin(\theta)\, d\theta \int_0^{2\pi} P_{\text{pd}}(\phi, \theta, \gamma) f(\theta_m, \phi_m) d\gamma \tag{3.33}$$

In this equation, f represents the final angular distribution of the photoelectrons in the atom/molecule frame, where (θ_m, ϕ_m) are the polar and azimuthal angles with respect to the z-axis. $I(\theta_s, \phi_s)$ denotes the photoelectron angular distribution pattern in the stationary/laboratory frame, where (θ_s, ϕ_s) are the polar and azimuthal angles relative to the direction of the electric field.

A given molecular orientation, characterized by the angles (ϕ, θ, γ), contributes to the laboratory frame distribution $I(\theta_s, \phi_s)$ through the term $P_{\text{pd}}(\phi, \theta, \gamma) f(\theta_m, \phi_m)$. To obtain the complete photoelectron distribution pattern, one must integrate over all possible orientations (ϕ, θ, γ).

Here, the photodetachment probability has a different meaning from that discussed so far and is related to the transition amplitude and then to the projection of the atomic dipole moment along the direction of the laser's electric field:

$$P_{\text{pd}}(\phi, \theta, \gamma) \propto |\mu \cdot \mathbf{E}|^2 \propto \cos^2(\theta) = \frac{2P_2(\cos\theta) + 1}{3} \tag{3.34}$$

with $P_2(\cos\theta)$ Legendre's polynomial of degree 2. This probability is therefore maximum when dipole moment and electric field are aligned ($\theta = 0$). By expressing $f(\theta_{\text{m}}, \phi_{\text{m}})$ as a series of spherical harmonics, it is possible to show [119] that the angular distribution of the emitted photoelectrons takes on the following expression:

$$I(\theta_{\text{s}}) = \frac{\sigma_{\text{pd}}}{4\pi}[1 + \beta P_2(\cos\theta_{\text{s}})] \tag{3.35}$$

where σ_{pd} is the spherical surface integral of f and represents the total cross-section for production of photoelectrons from an unpolarized target (in the dipole approximation) by 100% linearly polarized light. β is the symmetry parameter and is a kind of angular mean of the distribution pattern and ranges from -1 to 2. For an asymmetry parameter of $\beta = 2$, the ejected photoelectrons will have a $\cos^2$ distribution (photoelectrons ejected preferentially in the direction- and anti-direction of the photon polarization vector). For an asymmetry parameter of $\beta = 1$, the ejected photoelectrons will have a $\sin^2$ distribution (photoelectrons ejected preferentially in the directions perpendicular to the photon polarization vector). For an asymmetry parameter of $\beta = 0$, the ejected photoelectrons will have an isotropic (spherical) distribution. In general, β also depends on the energy of the incident photon. During the composition of this thesis, an article has been published demonstrating that the photodetachment of Ps^- also follows a distribution in accordance with PADs, particularly exhibiting a behavior very similar to that of the H^- ion [120]. In the photodetachment process, Ps^- loses an electron from the s orbital, resulting in a p-wave continuum electron and the residual Ps. Following the theory of Cooper and Zare [118], the corresponding value of β is 2, regardless of the incident photon energy, and in Ref. [120], it is shown that this value is in agreement with experimental data.

As discussed in Chapter 4, the interferometer is highly sensitive to angular distributions transverse to the atomic beam (x and y directions) and fairly robust to velocity variations along the atom propagation direction. A possible strategy to minimize the detrimental effects of photodetachment is therefore to use a linearly polarized laser beam with the electric field aligned along the direction of propagation of the atomic beam obtained by means of a half waveplate. Assuming the atomic beam is fully polarized along the direction of the field, we can simulate the photodetachment kinematics by randomly sampling the angles α and ξ from a $\cos^2$ distribution in $[-\pi/2, \pi/2]$ and a uniform distribution between 0 and 2π respectively (see the inset in Figure 3.17. The velocity change distribution caused by recoil for the three velocity components is depicted in Figure 3.17: each point represents a random extraction of the angles α and ξ. At each point in the figure corresponds a vector $\Delta\mathbf{v} = [\Delta v_x, \Delta v_y, \Delta v_z]$, and by aligning the electric field along the z-axis, a higher probability of recoil along z is observed, resulting in a greater concentration of points in the regions of the sphere with high Δv_z. The effect of recoil in the aforementioned configuration has been integrated into the model described in Section 3.2.2 by adding the velocity change due to recoil to the velocity of the atomic beam.

In Figure 3.18a, the simulation results regarding the distributions of angles θ_x and θ_y before (blue curve) and after (red curve) photodetachment at 1560 nm are presented, starting from the atomic beam distributions described earlier: the standard deviation of the distribution increases from 5 mrad to approximately 11 mrad. No distinction was made between θ_x and θ_y since the only difference between the two angles could arise from recoil given by Δv_{ex}, which remains negligible. The same analysis was conducted on the velocity distribution in the propagation direction, which is the most penalized by the chosen configuration. It can be observed (Figure 3.18b) that the energy spread of the beam after photodetachment at 1560 nm is

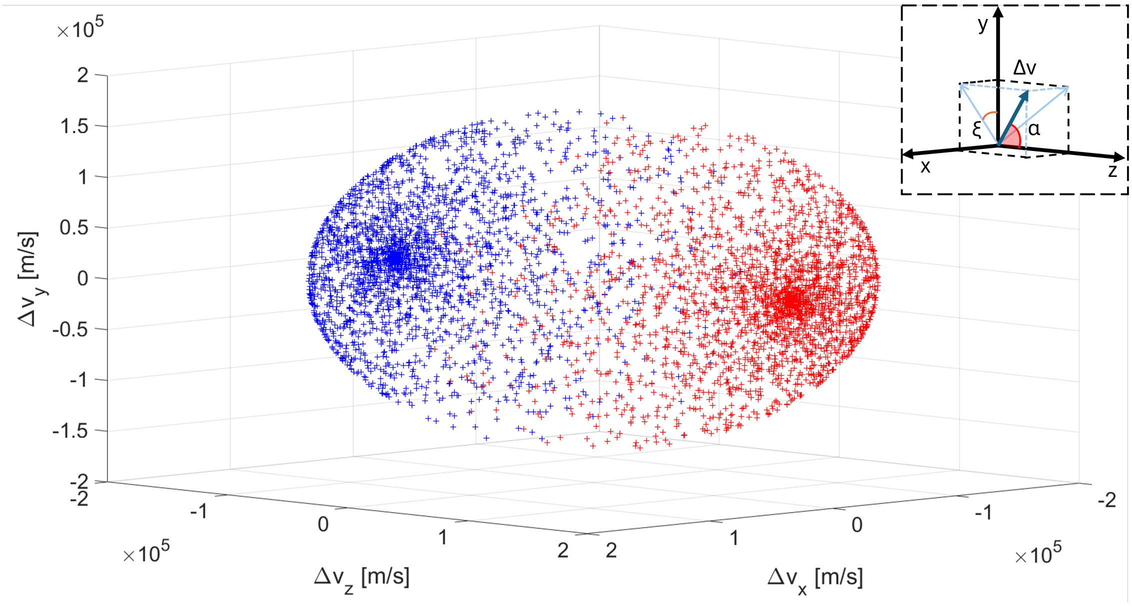

Figure 3.17: Recoil distribution caused by photodetachment. Each point in this 3-D image represents a random extraction of the angles α and ξ according to the distributions described in the text. The inset depicts the reference frame used to describe the angles: $[\Delta v_x, \Delta v_y, \Delta v_z] = \Delta v \cdot [\sin(\xi)\sin(\alpha), \cos(\xi)\sin(\alpha), \cos(\alpha)]$.

approximately ±11 eV, about an order of magnitude larger than the starting beam. As described above, the recoil amount following electron detachment is proportional to the difference between the energy of the incident photon and the photodetachment threshold. Another strategy to reduce the destructive effect of the process is therefore to use light with wavelengths close to the threshold. In Figure 3.18, the distributions obtained with a 3600 nm laser are shown in green. The results indicate that with this light, it would be possible to maintain the angular deviation almost unchanged and reduce the energy spread to approximately ±2 eV.

However, there is an important consideration to be made: the cross-section at 3600 nm is approximately an order of magnitude lower than that at 1560 nm, requiring an optical power of about 2 MW. This power could be achieved with a pulsed system [121], but an accurate design would be necessary to efficiently interface and synchronize the Ps^- beam production system with the photodetachment stage.

We now inquire how much the initial distributions of the atomic beam affect those of the photodetached beam. Figure 3.19 shows the ratio of the input and output beam angular divergences, σ_i/σ_f, with respect to the input divergence, for both considered wavelengths. It is observed that the input beam influences less than 50% when it has less than about 1 mrad and 5 mrad for 3600 nm and 1560 nm, respectively. These results suggest two things: in order to benefit from a 3600 nm pulsed system, it is necessary to have a focusing system capable of achieving a divergence below 1 mrad; it is not useful to try to reduce the angular divergence of the Ps^- beam below 5 mrad when performing photodetachment at 1560 nm, but

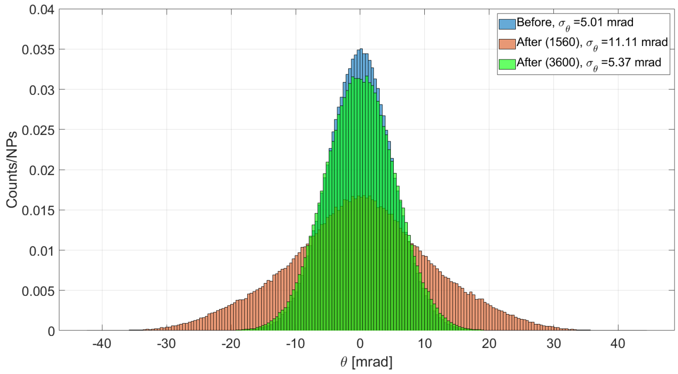

(a) Angular distributions of the atomic beam before and after photodetachment with light at 1560 and 3600 nm.

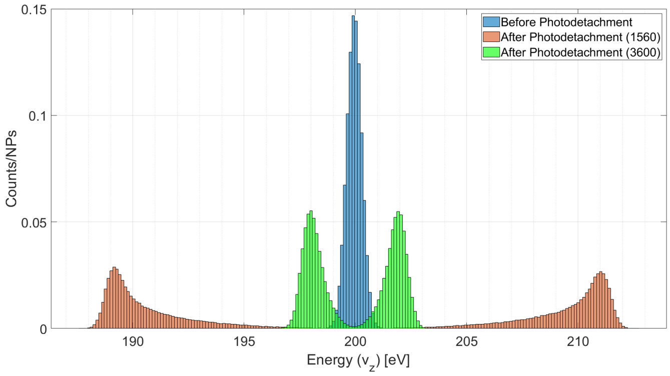

(b) Kinetic energy distributions of the atomic beam before and after photodetachment with light at 1560 and 3600 nm.

Figure 3.18: Monte Carlo simulation results for beam kinematics analysis.

rather it is preferable to prioritize atomic flux. Given that there are still several technical aspects to be designed for an experimental setup that involves an atomic source suitable for a high-power pulsed laser system at 3600 nm and for the reasons mentioned at the beginning this chapter, a continuous-wave laser system at 1560 nm has been chosen for Ps^- photodetachment. In the next paragraph, we will discuss its experimental implementation.

3.3 Experimental setup, realization and results

As previously discussed in Chapters 1 and 3, the original experimental setup utilizes ^{22}Na as the positron source to produce a beam of Ps^-. This source has been subsequently replaced by a LINAC, which is currently under construction, to ensure a significantly higher atomic flux. While awaiting the realization of this second approach, the project has set intermediate objectives to sequentially test the stages of the experiment.

For example, Figure 3.20a illustrates a setup aimed at testing the production, acceleration, and focusing stages, as well as the photodetachment stage. The schematic

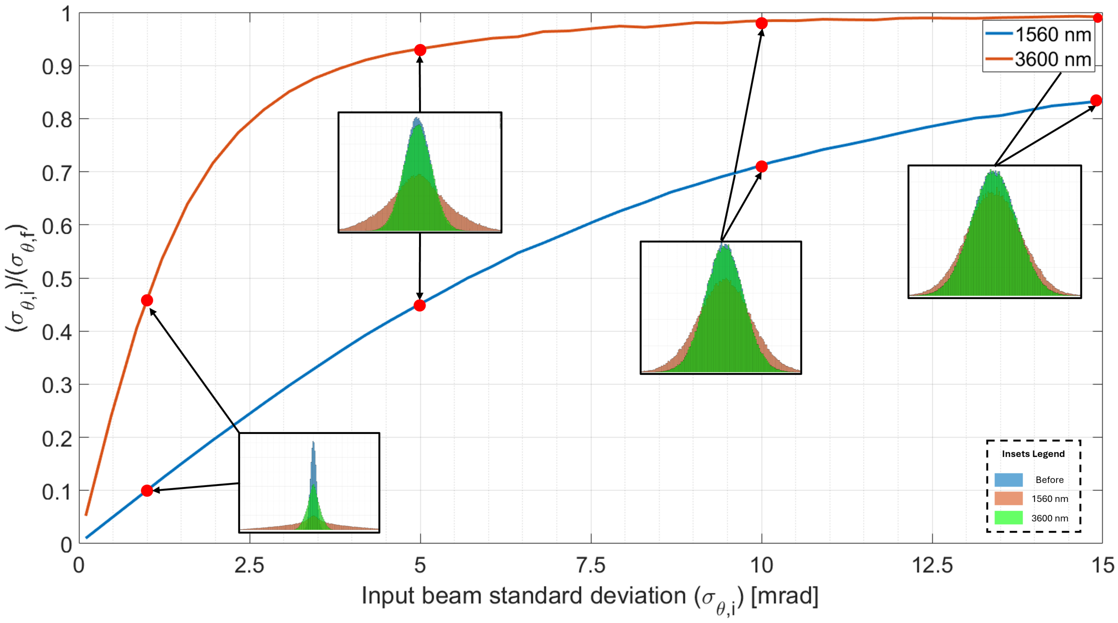

Figure 3.19: The ratio between the input and output angular standard deviation of the atomic beam for two different laser wavelengths is depicted. At 3600 nm, the contribution of the photodetachment recoil affects the beam distribution nearly as much as the initial distribution, already for approximately 1 mrad. At 1560 nm photodetachment dominates up to just over 5 mrad. Insets in the figure illustrate distributions for various values of $\sigma_{\theta,i}$.

also includes a material grating interferometer, similar to the setup shown in Figure 1.2a, which would measure an interferometric signal of Ps. The atomic beam exiting the converter intersects with the laser in the green-colored area at a 30° angle and then proceeds toward the interferometer. This inclination is designed to shield the detector at the end of the interferometer from residues originating from the atomic source. The cavity spacer is highlighted in yellow, while the mirror chambers are depicted in gray on the sides. These chambers are mounted on Z-motors to ensure vertical alignment. The component of primary interest is the photodetachment cavity, whose characteristics will remain unchanged in the final experimental setup. Figure 3.20b shows the cavity chambers and the mirror mounts installed on rotational stages that ensure alignment in the x-y and y-z planes. The cavity chamber consist of a 5-way aluminium setup utilizing CF60 crosses and a CF130 sealing the assembly. This configuration can accommodate the laser input through kodial glass viewport, the cavity spacer between the mirrors, vacuum pump connection, and UHV electrical feedthroughs. The chosen piezo stage (SR-5714CS from Smaract) are electrically controlled from outside the cavity, offers compatibility with vacuum levels up to 10^{-11} mbar, allowing for precise alignment after the entire system has been placed in ultra-high vacuum.

Since the experiment is being developed in different laboratories before integrating the various stages, a test cavity has been designed. This test cavity is very

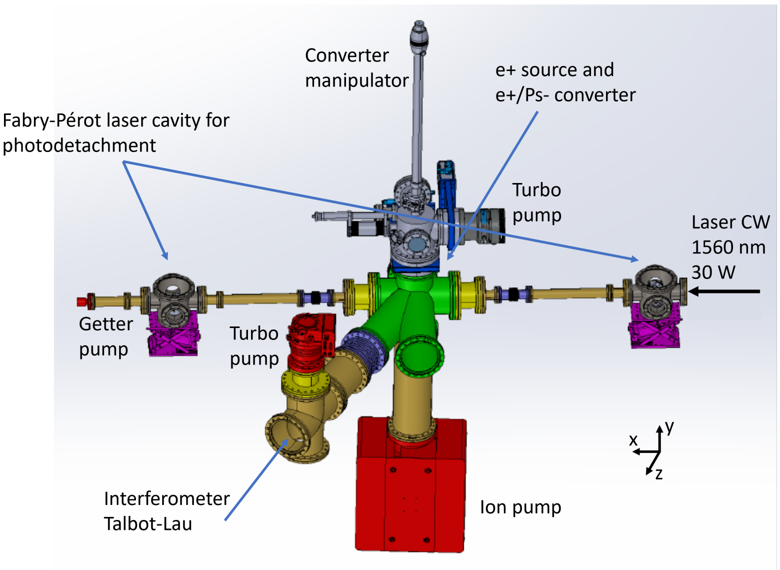

(a) Intermediate phase experimental setup designed to test the photodetachment stage and obtain an interferometric signal of Ps. The atomic beam exiting the converter intersects with the laser in the green-colored area at a 30° angle and then proceeds towards the interferometer. The positron source is also located in the green area, few millimeters from the laser beam. The cavity spacer is highlighted in yellow, while the mirror chambers are depicted in gray on the sides. These chambers are mounted on Z-motors to ensure vertical alignment.

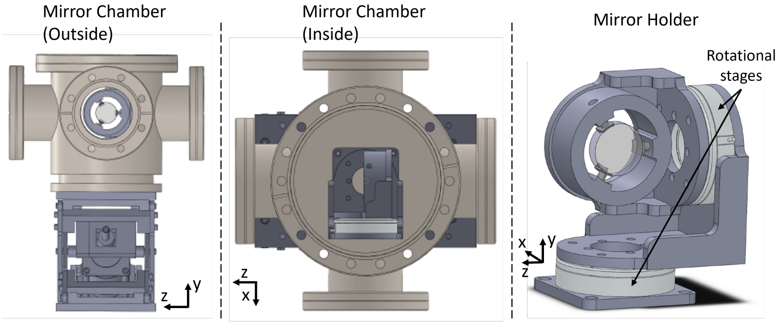

(b) Drawings of the mirror chambers positioned on Z-motors and the mirror mounts equipped with electric motors rotating around the y and z axes.

Figure 3.20: CAD drawings depicting the photodetachment cavity and its interface with the rest of the experimental setup during an intermediate phase of the experiment. This phase aims to test the various stages and measure an interferometric signal from Ps. The characteristics of the cavity will remain unchanged in the final phase of the experiment

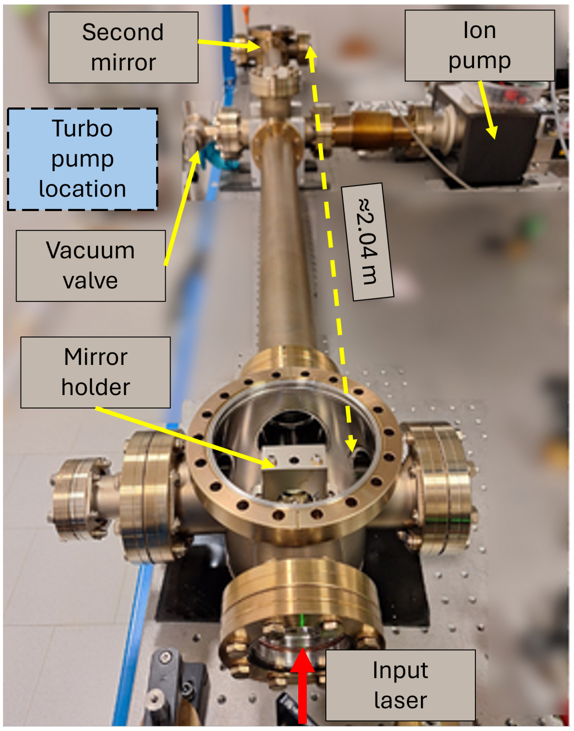

Figure 3.21: Photograph of the experimental apparatus tested during this thesis research. The photo is taken from one side of the cavity, near one of the two mirrors, and shows the viewport through which the input laser passes, a mirror holder in an open chamber separated from the cavity spacer by approximately 2.04 meters to the other chamber. It also displays an ion pump and the vacuum valve that seals the circuit for the turbo pump, which is not shown in this photo.

similar to the one shown in Figure 3.20a, with the key difference being that the central cross is a simple 5-way model with perpendicular branches. These branches are intended to accommodate an ion pump, a getter/turbo pump, the arms of the cavity spacer, and an inlet for potential testing with the Ps beam without the interferometer (which does not require a 30° inclination). A picture of this setup is shown 3.21.

Preliminarily, due to laboratory availability constraints, the mirror mounts and rotational stages have been replaced with fixed mounts compatible with UHV (9814-8-Ni-K-V Newport). In this configuration, Z-motors are not necessary, and the vertical alignment is ensured by the mirrors outside the cavity. While awaiting the arrival of the rotational stages and with the goal of characterizing the cavity in the absence of potential thermal effects, the following project plan has been implemented:

1. Test the cavity at low input power in air with fixed mounts.
2. Test the cavity at low input power in vacuum with fixed mounts.
3. Test the cavity at high input power in vacuum with mobile mounts.
4. Test the cavity at high input power with a temperature compensation system

(if needed).

The transition from the first to the second step involves only closing and evacuating the apparatus (assuming the bellows sufficiently decouple the pump vibrations), while step 3) requires realigning the cavity in vacuum. In this thesis, we will touch upon the preliminary results of point 1), which has the goals of testing the locking of the laser to the cavity using the Pound-Drever-Hall (PDH) technique [122, 123], verifying the coupling efficiency obtained and estimating the finesse of the cavity.

Given that the cavity is approximately two meters long, it is impossible to simultaneously adjust by hand both its mirrors and those of the external optical circuit. Additionally, over a length of two meters, parallax error makes centering the optical axis in the cavity more challenging. To facilitate this process, the affinity between the reflection characteristics of IR-coated (E04 and C-coating [124]) mirrors and the green wavelength was exploited. A preliminary alignment of the cavity was performed using visible light at 532 nm, following the scheme shown in Figure 3.22a. The beam splitter, compatible with 532 nm, and the entire green light circuit were removed after the preliminary alignment, which was secured using two diaphragms (vertical dashed lines in the figure).

3.3.1 Laser characterization

The IR diode used is a RIO-PLANEX butterfly package external cavity diode laser, emitting fiber-coupled light at around 1560 nm with a maximum power of approximately 10 mW. It includes an internal temperature control actuator. The diode is mounted on a Thorlabs LM14S2 mount, compatible with a Bias-T for high-frequency modulation. Before being used for the photodetachment cavity, the laser was characterized by analyzing its beat note with an NP Photonics Rock Source laser using a spectrum analyzer (see Figure 3.23). Both lasers have a specified linewidth of less than 15 kHz, while their beat note shows a linewidth of about 156 kHz. This broadening, typically due to thermal and current drifts, is sufficiently narrow to allow for locking between the laser and the cavity.

To scan the cavity, the laser current was modulated with a ramp-shaped signal (referred to in this discussion as the sweep) having a frequency of $\nu_{\mathrm{sw}} = 6$ Hz and a user-adjustable peak-to-peak amplitude $V_{\mathrm{sw,pp}}$ ranging from 0 to 1 V. The sweep signal is input to the laser driver, which uses a commercial Koheron DRV200 board with an input voltage to output current ratio, $\left(\frac{\Delta I}{\Delta V}\right)_{\mathrm{K}}$, of 1 mA/V (according to the datasheet). During the beat note measurement, the frequency response of the laser was studied by varying the laser driver's current, and it was found that the frequency change per mA is approximately $\left(\frac{\Delta \nu}{\Delta I}\right)_{\mathrm{las}} = 300$ MHz/mA. This implies

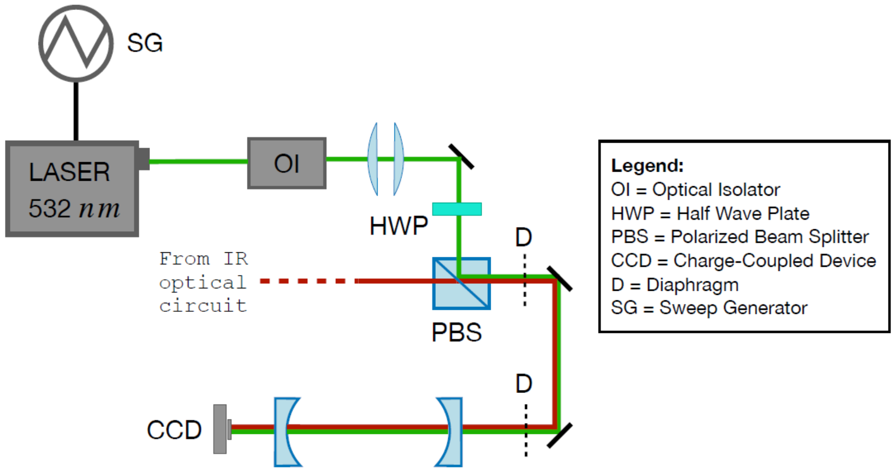

(a) Pre-alignment Circuit for the Cavity: The shared part of the circuit took advantage of the high reflectivity of the IR mirrors even at green wavelengths. After pre-alignment, the green laser circuit has been removed.

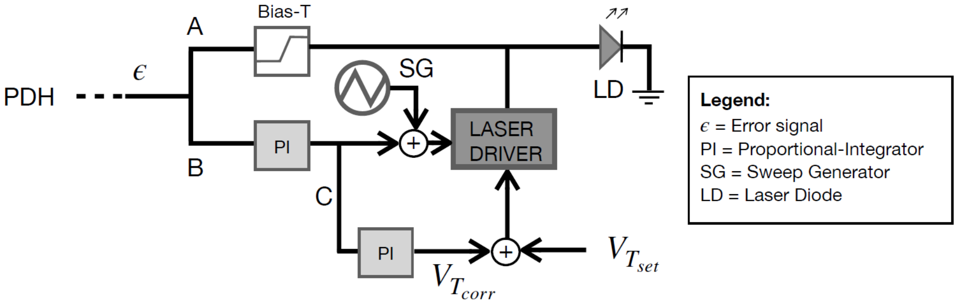

(b) Feedback System for Laser Locking to the Cavity via PDH: Paths A, B, and C divide the error signal into high, medium/low, and low frequencies. Path C, designed for finer low-frequency control, adjusts the set point of the laser diode's temperature and has not been implemented at this stage of the work.

Figure 3.22: Optical and electronic circuits for pre-alignment and locking of cavity and laser.

that the laser can move with a scan rate given by

$$\dot{\nu} = V_{\text{sw,pp}} \left(\frac{\Delta I}{\Delta V}\right)_{\text{K}} \left(\frac{\Delta \nu}{\Delta I}\right)_{\text{las}} \frac{1}{\nu_{\text{sw}}} \in [0, 50]\,\text{MHz/s} \tag{3.36}$$

For the case study application, a sweep range of less than 100 MHz is generally used, corresponding to a scan rate of less than 17 MHz/s. It is important to note, however, that these values do not account for thermal and current drifts of the free-running laser, which set a lower limit on the scanning rate greater than 0. This is the main reason why a technique to lock the laser to the cavity is necessary to probe the cavity resonance accurately.

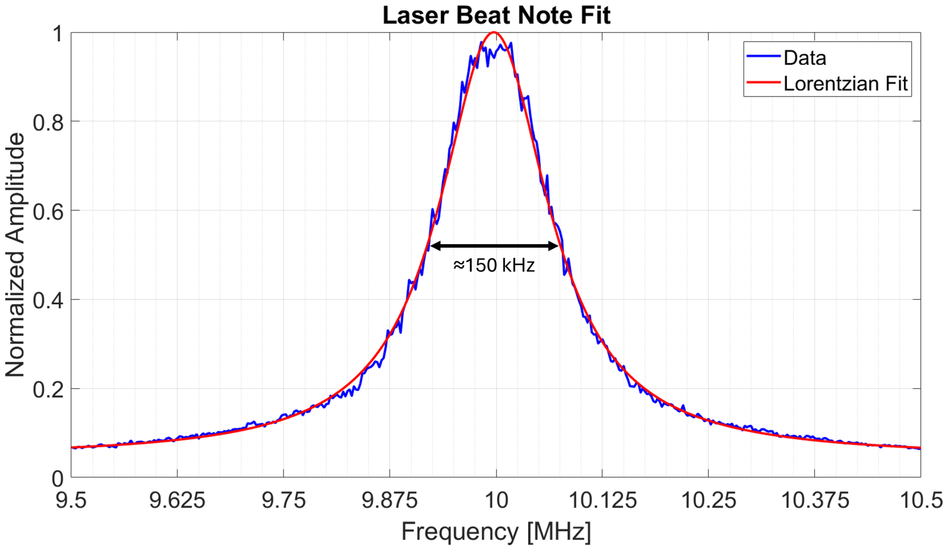

Figure 3.23: Spectrum of the beat note between the laser used for the photodetachment cavity and another laser with a similar wavelength of approximately 1560 nm. Both lasers have a linewidth below 15 kHz, but due to various noise sources, the beat note exhibits an FWHM of approximately 150 kHz over a scan duration of about 20 ms on the spectrum analyzer having resolution bandwidth equal to 10 kHz.

3.3.2 PDH locking setup

In the realm of laser frequency control, the mentioned Pound-Drever-Hall (PDH) technique [122,123] is widely used to stabilize the laser frequency relative to an optical cavity. This technique involves generating an error signal that is used to correct the laser frequency, keeping it in resonance with the cavity.

The transmission signal of the optical cavity is obtained by monitoring the power of the light that passes through the cavity. When the laser frequency is exactly resonant with one of the cavity's resonant frequencies, the transmission is at its maximum. Off-resonance, the transmission decreases rapidly due to the high finesse of the cavity. This behavior clearly identifies the resonance points and allows measurement of the cavity's response to laser frequency modulation.

The PDH error signal is generated by phase modulating the laser beam before it enters the optical cavity. This creates two sidebands around the laser's carrier frequency. The light reflected from the cavity is then detected by a high-frequency photodiode, and its signal is mixed with the original modulation signal. The product of this mixing, after low-pass filtering, provides a signal containing information about the frequency error between the laser and the cavity.

As mentioned, the cavity is composed of mirrors on fixed mounts, thus lacking piezoelectrics for adjustment. Consequently, the error signal generated by the PDH for feedback control will be utilized by the only available actuators in the system: the current and temperature of the diode. The proposed feedback control scheme is illustrated in Figure 3.22b. The error signal is split and directed towards the Bias-T (path A) and a PI controller (path B). The Bias-T essentially acts as a high-pass filter connected directly to the anode of the diode configured as cathode ground. The path through the PI controller is then split again to form a line directly to the driver, along with a ramp for cavity scanning, and a line to adjust the diode's temperature setting (path C). The latter path, intended to compensate for the cavity's slow drift, has not yet been implemented as it a slower correction compared to the others. However, it will be implemented for high-power tests. For the current discussion, the temperature setting is fixed.

Although path B processes the entire signal, it also acts as a low-pass filter with a cutoff frequency on the order of MHz. Therefore, paths A and B can be understood as a division of high and middle/low frequencies, both influencing the diode current.

The electro-optical setup utilized for PDH is depicted in Figure 3.24. Light emitted by the diode crosses an isolator (IO-G-1550 Thorlabs) and the iXblue MPX-LN-0.1 fiber electro-optic modulator (EOM), before transitioning into free space and passing through a 1:1 telescope with a movable lens for cavity mode matching. Subsequently, the beam passes through a half-waveplate (HWP) and a polarizing beam splitter (PBS) before being injected into the cavity. The transmission through the cavity and the end mirror is detected by a Thorlabs PDA10CS2 photodiode made of InGaAs, amplified with switchable gain, typically set to either 0 or 10 dB to utilize the higher bandwidths, which are 13 and 1.7 MHz, respectively.

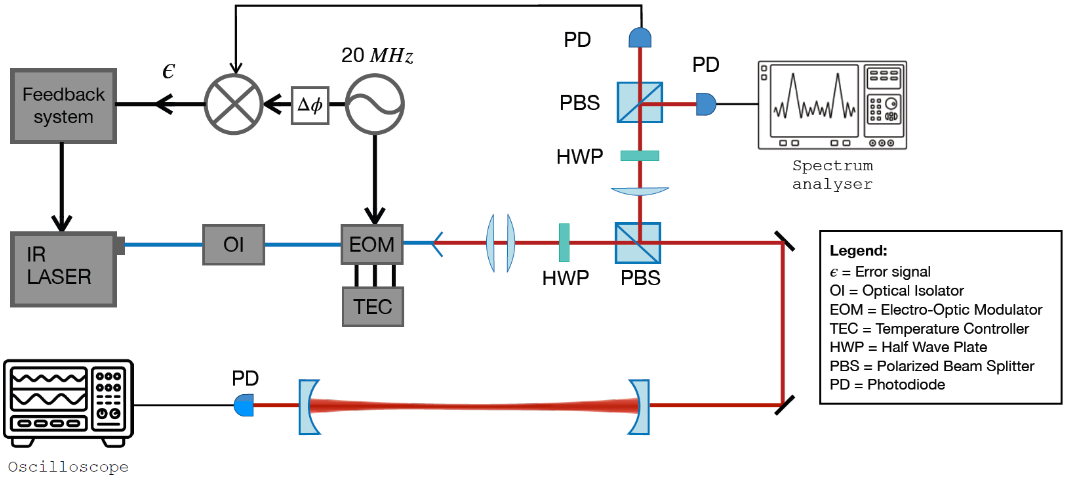

Figure 3.24: Electro-optical circuit for laser-cavity locking using the Pound-Drever-Hall technique. The feedback system is illustrated in Figure 3.22b.

The light reflected from the cavity is directed by the PBS towards another pair of HWP-PBS to split the beam between two photodiodes able to work at 20 MHz. Before this final waveplate, a lens focuses the beam onto the photodiodes.

Note that in this setup there are no quarter-waveplates before the cavity to ensure linear polarization, as explained in section 3.2.3.

The initial error signal obtained exhibited pronounced sinusoidal-like distortions, hindering proper locking. Following a thorough circuit analysis, it was determined that this issue stemmed from residual amplitude modulation (RAM).

3.3.3 RAM monitoring and compensation

RAM is a phenomenon that arises during optical phase modulation, and results in an unintended amplitude modulation.

Some of the main sources of RAM are etalon effects in optical components and imperfections in the EOM used to impose phase modulation on a laser beam.

The etalon effect is caused by the finite reflectivity of the optical medium, which allows some light to circulate within the crystal, creating a multipass light field. This circulating light field experiences a frequency-dependent phase shift and amplitude modulation.

EOM imperfections can stem from the misalignment of the input beam polarization with respect to the crystal axes, and etalon effects within the crystal due to imperfect angle-cut end facets. When a random polarized laser beam passes through the EOM, the birefringence can lead to different phase shifts for orthogonal polarization components, effectively rotating the polarization and converting some of the phase modulation into amplitude modulation when a subsequent interaction with polarizing optics occurs.

The presence of RAM introduces systematic and drifting frequency offsets in the error signal used for laser frequency stabilization. This offset can degrade the stability and accuracy of the frequency lock, leading to erroneous measurements and reduced sensitivity in several applications.

After observing the distortion in the error signal, the optical circuit was analyzed at multiple points using a spectrum analyzer, yielding the results shown in Figure 3.25a. This spectrum was acquired with a 10 MHz modulation, and the peaks indicate amplitude modulation at the modulation frequency and its higher harmonics. This observation can be understood by considering the expression of the modulated electric field after passing through the EOM and impinging on the cavity:

$$E_{\mathrm{i}} = E_0' e^{i(\omega t + \beta \sin{(\Omega t)})} \tag{3.37}$$

With ω denoting the laser frequency, β the modulation depth, and Ω the modulation frequency. With no RAM, the field amplitude remains constant, $\mathrm{E'}_0 = \mathrm{E}_0$, and at the first order of the series expansion, one obtains the typical expression of the phase modulated field [122]:

$$E_{\mathrm{pm}} = E_0[1 + i\beta \sin(\Omega t)]e^{i\omega t} = E_0 \left[e^{i\omega t} + \frac{\beta}{2}(e^{i(\omega+\Omega)t} - e^{i(\omega-\Omega)t}) \right] \tag{3.38}$$

If we consider RAM, modulation also affects the amplitude of the field, taking the form $E_0' = E_0(1 + \gamma \sin(\Omega t + \phi))$, where γ represents the RAM modulation depth, and ϕ is the phase difference between the RAM modulation and the desired modulation of the EOM. Equation 3.37 transforms into:

$$\begin{aligned} E_{\mathrm{i}} =& E_{\mathrm{pm}} + \frac{i\gamma}{2}\left[e^{i(\Omega i+\phi)} - e^{-i(\Omega i+\phi)}\right] E_{\mathrm{pm}} \\ =& E_{\mathrm{pm}} + \frac{iE_0\gamma}{2}\left[e^{i[(\omega+\Omega)t+\phi]} - e^{i[(\omega-\Omega)t+\phi]}\right] \\ +& \frac{iE_0\beta\gamma}{4}\left[e^{i[(\omega+2\Omega)t+\phi]} + e^{i[(\omega-2\Omega)t-\phi]} - \left(e^{i[\omega t+\phi]} + e^{i[\omega t-\phi]}\right)\right] \end{aligned} \tag{3.39}$$

RAM introduces terms that oscillate at twice the modulation frequency. When detecting the field, the measured quantity is the power, given by $|E_{\mathrm{i}}|^2 = E_{\mathrm{i}} \cdot E_{\mathrm{i}}^*$ which clearly contains terms oscillating at multiples of Ω. However, the terms with frequencies that are multiples of Ω are not relevant, as they are filtered out by a low-pass filter at the output of the mixer in the PDH circuit.

A strong dependence of the peak amplitudes in Figure 3.25a on the EOM temperature was observed, corroborating studies in the literature on this topic [125,126]: temperature drifts affect the orientation of the crystal due to the thermal expansion of the mounting material and of the crystal which expands, directly modulating its static birefringence. By maintaining a stable temperature, the thermal effects within the EOM were minimized, leading to a substantial reduction in the unwanted amplitude modulation and enhancing the overall stability of the frequency lock. This justifies the presence of the temperature control and the spectrum analyzer in Figure 3.24. Figure 3.25b shows the spectrum obtained with temperature stabilization: it demonstrates a reduction in the modulation depth by more than an order of magnitude, making the RAM negligible.

A potential etalon effect caused by the mirrors and viewports was also considered. After disassembling and studying their effect on the spectrum of transmitted and reflected light, both individually and combined, it was concluded that their impact on RAM is negligible. To make sure there were no similar effects, the PBS after the first HWP was replaced by a piece of glass placed at 45° to the beam passing through it.

3.3.4 Transmission, error signal and locking

The following sections will use some figures of merit from the theory of optical resonators, which will not be dealt with exhaustively and for which reference is made to the literature [127–130].

Mathematically, the incident phase modulate beam is the one showed in equation 3.38 which is characterized by the modulation sidebands at frequencies $\omega \pm \Omega$. When the laser frequency is near the cavity resonance, the reflected light shows phase and

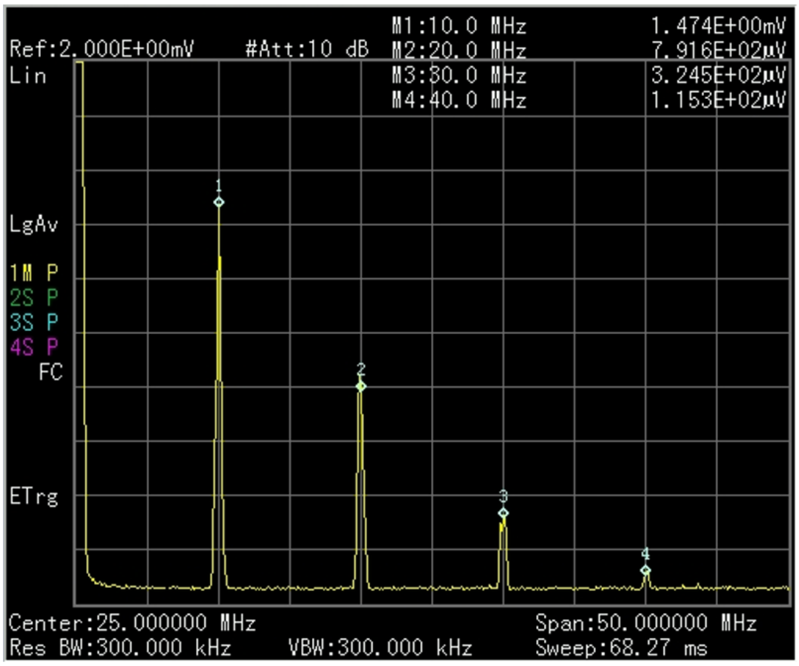

(a) Uncompensated RAM: the markers indicate values ranging from about 1.5 mV to hundreds μV for the first four upper harmonics of the modulation frequency.

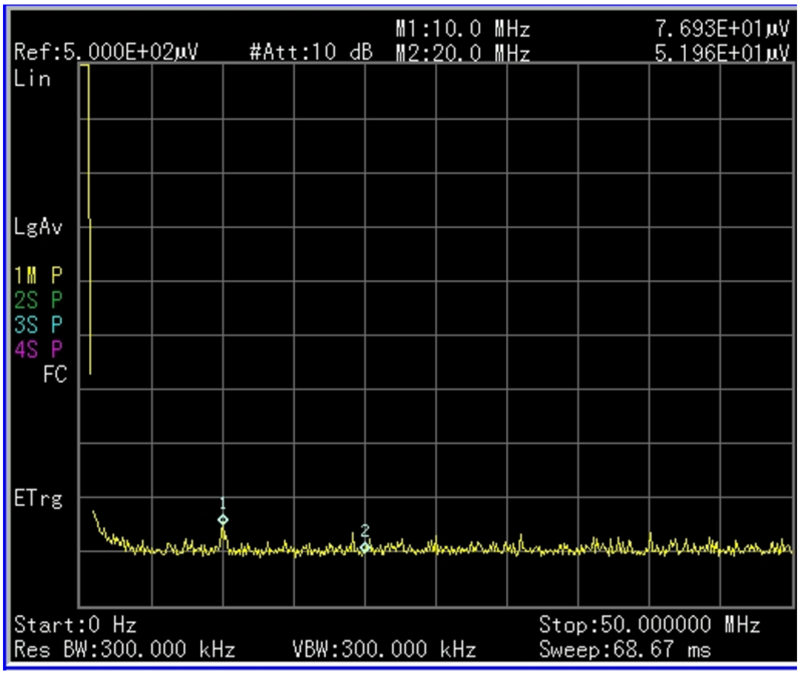

(b) Compensated RAM: amplitude modulation peaks are reduced significantly by holding the EOM at a specific fixed temperature.

Figure 3.25: Spectrum of the power beam along the optical circuit. Peaks indicate residual amplitude modulation before (a) and after (b) temperature stabilisation of the EOM operating at a modulation frequency of 10 MHz.

amplitude variations that, once demodulated, provide the error signal.
For high-frequency modulation, where the modulation frequency is much greater than the the cavity full width at half maximum (FWHM) linewidth, $\Omega \gg \Delta\nu_{\text{FWHM}}$, the error signal can be expressed by considering that Ω is sufficiently high to cause the sidebands to be entirely reflected by the optical cavity. Under this condition, and near the cavity resonance, the error signal ϵ is given by:

$$\epsilon = -2\sqrt{P_i P_s}\,\text{Im}\{r(\omega)\}\sin(\Omega t) \tag{3.40}$$

where P_i is the power of the incident field, P_s is the power of the sidebands, and $r(\omega)$ is the reflection coefficient of the cavity.
In the high-finesse limit and for $\Delta\omega < \Delta\nu_{\text{FWHM}}$, the reflection coefficient can be approximated as $r \simeq \frac{i}{\pi}\frac{\Delta\omega}{\Delta\nu_{\text{FWHM}}}$, with $\Delta\omega$ representing the detuning from resonance. This gives an error signal:

$$\epsilon \propto \sqrt{P_i P_s}\frac{\Delta\omega}{\Delta\nu_{\text{FWHM}}} \tag{3.41}$$

The linearity of this signal allows us to apply control theory techniques to correct the laser frequency, keeping it locked to the cavity resonance [122].
The analysis of the transmission and error signals in a PDH system is crucial for stabilizing the laser frequency and an accurate characterization of these signals allows precise frequency control.

Figure 3.26a displays a screenshot of the acquisitions related to the laser scanning through the cavity. From top to bottom, it shows the sweep profile, the error signal, and the laser transmission. The sweep covers a range of approximately two longitudinal modes of the cavity so that two peaks in the transmission signal are visible. In this data acquisitions the modulation was at 20 MHz.
The violet curve shows the typical shape of the error signal, which consists of a peak that changes from positive to negative values near the resonance, where it goes to zero. For each cavity mode, the error signal exhibits two additional peaks corresponding to the modulation sidebands. These peaks also become visible in the transmission signal by increasing the modulation depth of the EOM beyond the chosen operating value (approximately 250 mV with $V_\pi = 1.5$ V).
The free spectral range of the cavity was measured by increasing the modulation frequency until an overlap of the sideband peaks with the cavity resonance peak was observed. The corresponding frequency value was then read from the signal generator, resulting in $\Delta\nu_{\text{FSR}} \simeq 74.2$ MHz.

Figure 3.26b highlights the transmission peak of a longitudinal mode of the cavity, resolved over a time interval of about 250 μs with an unlocked laser.
The small side peaks are a typical profile that accompanies Lorentzian transmission when the scan rate $\dot{\nu}$ is much greater than $\Delta\nu_{\text{FWHM}}$. This effect is easily observed in high-finesse Fabry-Pérot cavities, which have a small $\Delta\nu_{\text{FWHM}}$. In Ref. [131],

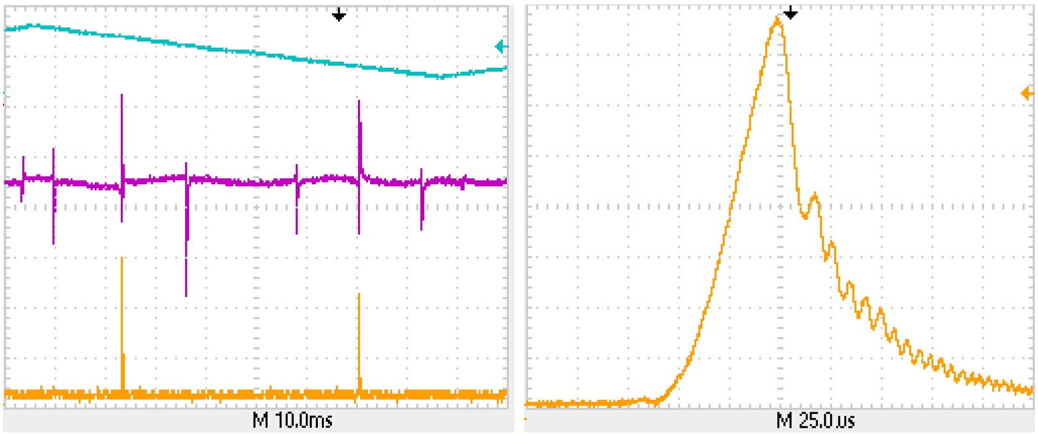

(a) From top to bottom: sweep, error signal, and transmission. The sweep scans over two longitudinal modes of the cavity.

(b) Transmission peak of a longitudinal mode of the cavity acquired during the cavity scan with unlocked laser.

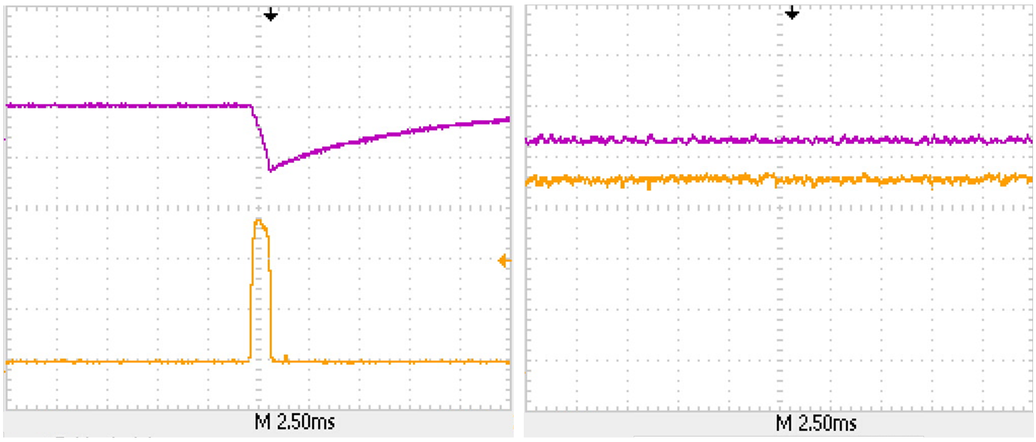

(c) Transmission and error signal with fast feedback (on the diode Bias-T) and slow feedback with integrator.

(d) Transmission and error signal during laser locking to the cavity.

Figure 3.26: Acquisitions and analysis of the sweep (light blue curve), laser transmission through the cavity (yellow curve), and error signal (purple curve). Figures depict screenshots of the acquired signals under different feedback and sweep configurations. The setup used for the acquisitions is depicted in Figure 3.24.

a model is proposed that describes the temporal response of a Fabry-Pérot cavity field to changes in cavity length and the frequency of the incident laser field. This model can be used to fit the scan rate or estimate other parameters such as the finesse [132].

The coupling efficiency has been estimated by measuring the ratio of the power transmitted by the cavity to the incident power and the result is approximately 40% of coupling efficiency. This estimate was made under the assumption of perfect mode matching (a reasonable assumption considering that the only peak attributable to a mode other than TEM00 had an amplitude of approximately 1% of the fundamental mode). Typically, good coupling efficiency exceeds 50%, and the lower value obtained here may be attributed to additional losses within the cavity. A detailed discussion of this issue is provided in the following section.

In Figure 3.26c, the transmission and error signal obtained with fast feedback (on the diode Bias-T) and slow feedback with an integrator are depicted. When the laser and cavity are connected to a well-tuned feedback system, the transmission peak tends to broaden. This occurs because the laser remains in resonance for a certain interval, thereby maximizing transmission during that period.

Figure 3.26d illustrates the transmission and error signal during laser locking to the cavity where the error signal cancels due to the action of the feedback system while the transmission is maximum.

3.3.5 Finesse estimation by CRDS

The finesse of an optical resonator, $\mathcal{F}$, is defined as the ratio between the free spectral range, $\Delta\nu_{\mathrm{FSR}}$, and the full-width half-maximum (FWHM) linewidth of the resonant longitudinal modes, $\Delta\nu_{\mathrm{FWHM}}$, which arises due to the imperfect reflectivity of the mirrors:

$$\mathcal{F} = \frac{\Delta\nu_{\mathrm{FSR}}}{\Delta\nu_{\mathrm{FWHM}}} \tag{3.42}$$

where $\Delta\nu_{\mathrm{FSR}} = \frac{c}{2L}$, with L being the length of the cavity. Given that the FSR is the frequency distance between the longitudinal cavity modes, the finesse can be interpreted as the frequency resolution of the Airy function shaped intensity peaks transmitted through the cavity: the higher the finesse, the more distinguishable the peaks are because they are well-spaced in frequency relative to their linewidth.

The finesse depends on the reflectivity of the mirrors, and as highlighted in Ref. [133], for low reflectivity values, the Lorentzian shape is no longer adequate to describe the transmission, which becomes a combination of longitudinal modes. Given that the nominal finesse (from the datasheet) of our cavity is high (40000), under the operational conditions described in the previous section, we assume it remains sufficiently high (mirror power reflectivity $\mathrm{R}_1 = \mathrm{R}_2 = \mathrm{R}$ greater than 0.85). Thus, we refer to the characteristics of a single longitudinal mode, for which the following holds:

$$\mathcal{F} = \frac{\pi\sqrt{R}}{1-R} \simeq \frac{2\pi}{-\ln(R^2)} \tag{3.43}$$

Now, consider the number of photons present in the cavity, ϕ. After j round trips, starting from ϕ_0, the number of photons, following an exponential decay, will be:

$$\phi(t_j) = e^{-t_j/\tau_c}\phi_0 \tag{3.44}$$

where $t_j = 2jL/c$ is the time it takes for light to complete j round trips, and τ_c is the photon lifetime. Assuming that the only power losses within the cavity are due to transmission through the mirrors, the intensity after j round trips is defined as:

$$I(t_j) = R^{2j}I_0 \tag{3.45}$$

By comparing the last two equations and using equations 3.43 and 3.42, we obtain:

$$\tau_c = \frac{-2l}{c\ln(R^2)} = \frac{\mathcal{F}}{2\pi\Delta\nu_{\mathrm{FSR}}} = \frac{1}{2\pi\Delta\nu_{\mathrm{FWHM}}} \tag{3.46}$$

Even though the losses occur solely at the mirrors, in this approximation, the photon lifetime is seen as a distributed loss within the cavity, similar to what happens when light is absorbed by a non-transparent medium. The specifications of the cavity show a finesse $\tilde{\mathcal{F}}$ =41000 and a photon lifetime $\tilde{\tau}_c = 4.2\,\mu$s for a cavity length of about 10 cm. We will now deal with estimating the finesse in our case study.

To estimate the finesse of an optical cavity, different methods can be employed depending on the circumstances and available resources. One of the most direct methods involves examining the transmission peak width of the optical cavity using an oscilloscope while sweeping the laser current (as shown in Figure 3.26b) to measure the width of the transmission peak in the time domain (Δt). The frequency width can then be estimated using $\Delta\nu_{\mathrm{FWHM}} = \dot{\nu} \cdot \Delta t$, and consequently, the finesse can be calculated using equation 3.42. However, this method requires a precise estimate of both Δt and $\dot{\nu}$, which in turn requires an accurate estimation of all the terms in equation 3.36, potentially complicating the process. In fact, one has to ensure that the scan rate is slow enough to allow photons to accumulate in the cavity. In our setup, this constraint can be estimated by considering the cavity frequency linewidth $\Delta\tilde{\nu}_{\mathrm{FWHM}}$ resulting from the specifications, which is about 1.8 kHz. Assuming we divide this linewidth into 100 samples, the required scan rate would be on the order of few MHz. At such scan rates, the free-running laser may already be dominated by thermal and current drifts, which could also cause $\dot{\nu}$ to be non-constant, thereby making the measurement less precise.

As previously mentioned, another method to estimate the finesse is to fit the transmission profile shown in Figure 3.26b with the function defined in [131]. However, finding the experimental conditions to achieve an accurate fit can be challenging. The method we will use, known as Cavity Ring-Down Spectroscopy (CRDS), offers an effective alternative for determining finesse without relying on the laser scan rate.

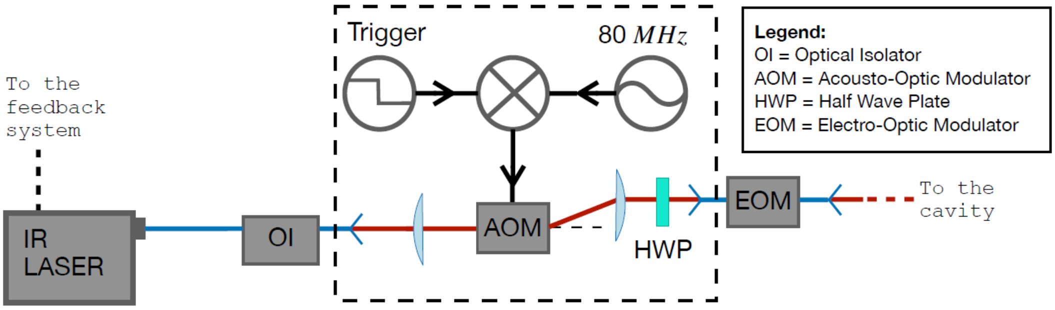

Figure 3.27: Setup employed for finesse measurement using Cavity Ring Down Spectroscopy technique. The dashed box encloses the additional setup compared to that in Figure 3.24, which includes an AOM activated by a trigger and a sinusoidal signal at 80 MHz mixed in.

In this method, the laser is first locked into the cavity for a much longer time than $\tilde{\tau}_c$ and once the light source is turned off, the optical field inside the cavity decays freely. The measured decay time (τ_c) of the optical field, acquired with a photodiode, is directly related to the finesse of the cavity according to equation 3.46.
A setup similar to that shown in Figure 3.24 was used, but with some modifications: between the fiber isolator and the EOM, a line incorporating the G&H 3080-1912 acousto-optic modulator (AOM), lenses for focusing into the AOM with 200 mm focal length, and a HWP to match the EOM polarization was added (see Figure 3.27). The AOM is used in this case due to its rapid response to the applied RF field, allowing the beam directed into the cavity to be turned on and off quickly. By aligning the fiber connected to the EOM with a diffraction mode of the crystal and rapidly turning off the AOM modulation signal, it is possible to switch off the cavity input fast enough not to disturb the free decay of the field in the cavity. The rapid switching of the RF signal is achieved by connecting the AOM to the output of a mixer with a signal at 80 MHz at the LO input and a DC input signal of a few volts that can be manually turned off. The mixer is a DMM-2-250 double balanced mixer which allows a DC IF input. Figure 3.28 shows the CRDS signal with a negative exponential fit. The fit reveals a photon lifetime of approximately 30 μs which, for an $\Delta\nu_{\mathrm{FSR}}$ of about 74.2 MHz, this corresponds to a finesse of approximately 14000. This value is about 35% of the expected finesse, and this discrepancy could be attributed to air absorption. We can estimate this effect by considering an additional loss mechanism in the cavity due to air absorption, which modifies equation 3.45 as follows:

$$\frac{I(t_j)}{I_0} = R^{2j} e^{-\alpha_{\mathrm{air}} 2Lj} = e^{-t_j/\tau_c} \tag{3.47}$$

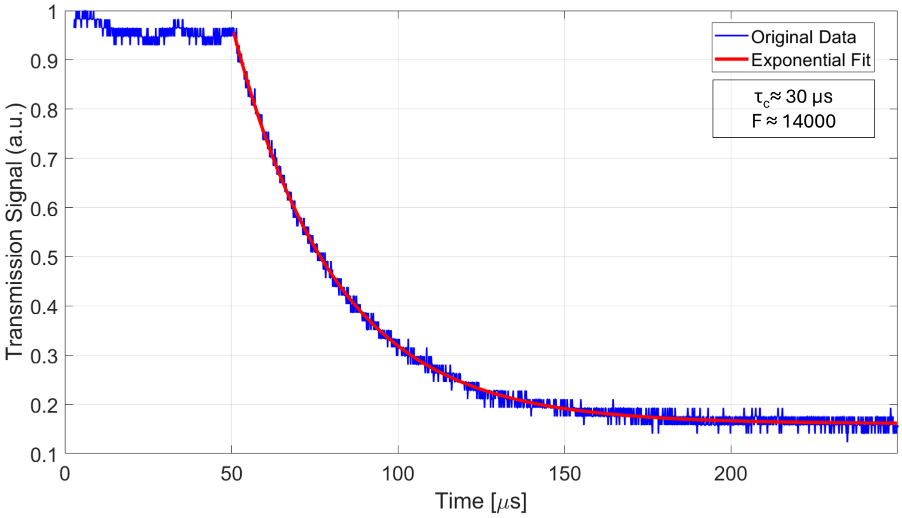

Figure 3.28: Cavity Ring Down Spectroscopy results: the blue curve represents the transmission signal through the cavity, which decays exponentially from its locked state with a decay rate of $1/\tau_c$ after the trigger signal is received. The red curve is the exponential fit that was used to extract the value of τ_c.

where α_{air} is the air absorption coefficient per unit length. Solving for α_{air} and considering equation 3.46, we get:

$$\alpha_{\text{air}} = \frac{1}{2L}\left(\frac{2\pi}{\mathcal{F}} + \ln\left(R^2\right)\right) \tag{3.48}$$

Assuming the mirrors have the listed reflectivity ($R = 1 - 78 \times 10^{-6}$) and using the finesse measured via CRDS, we find $\alpha_{\text{air}} \simeq 71\,\text{ppm/m} = 0.71\,\text{ppm/cm}$. This is consistent with the order of magnitude for light absorption at 1560 nm in air, primarily due to water vapor [134, 135].

In the next stages of the experiment, which involve evacuating the system, it is espected to achieve finesse values closer to the design specifications. To this end, before use, the cavity has been baked to test the vacuum integrity of the system, reaching a pressure below 1×10^{-10} mbar.

Chapter 4

SPLMT interferometer to measure the effect of gravity on positronium

The aim of the design activity behind the LMT interferometer proposed in this thesis is to find an improvement with respect to other types of interferometers based on high-order Bragg processes [136], Raman-Nath standing-wave interactions [137] or adiabatic transfer [138, 139] that impose too restrictive constraints on the velocity spread of the atomic beam or are unable to populate higher-lying momentum states. Conventional light-pulse atom interferometry uses two-photon interactions. However, some challenging applications, such as ultralight dark matter searches [140, 141] and gravitational wave detection [142–147], prefer the use of single photon transitions. Multiple pulses LMT-enhanced interferometry is an active research field and new configurations based on single photon transitions have been recently implemented on atomic clocks [148] and as a method to reach the required sensitivity improving the rejection of laser noise [149]. Indeed, this kind of interferometer can be particularly convenient because it allows the use of phase noise suppression techniques [150] such as the one discussed in this thesis.

Equation 1.2 shows that the quantities to be maximized to obtain a large signal are k_{eff} and T. Since Ps is unstable, designing an interferometer with too high T would lead to a severe reduction of the beam population. For this reason, maximizing k_{eff} by designing a LMT interferometer is the most convenient strategy. Moreover, the need to avoid a rapid annihilation of the Ps leads us to consider one of the excited $n = 2$ Ps states, precisely the 2^3S state, which has an annihilation lifetime of 1.14 μs and a radiative lifetime of 0.2 s. This state therefore guarantees a much higher survival probability of the Ps atoms with respect to the ground (0.142 μs lifetime) ortho-positronium state. We can exploit this long living Ps state by designing an interferometer resonant with the 2^3S_1-3^3P_2 transition, as already mentioned (see Figure 1.1 for energy level scheme of Ps, transitions and lifetimes).

We now turn to how to choose k_{eff} and T. Before proceeding, it is essential to define the meanings of these two quantities and how they depend on the chosen interferometric configuration. In Ref. [151], some results of this thesis work are reported, and an LMT interferometer exploiting single-photon transitions (SPLMT) is proposed, as illustrated in Figure 4.1. This type of interferometer retains the same macroscopic structure as a basic Mach-Zehnder interferometer shown in Figure 2.1, but the action of the beam splitter and mirrors is attributed to a set of pulses rather than a single pulse.

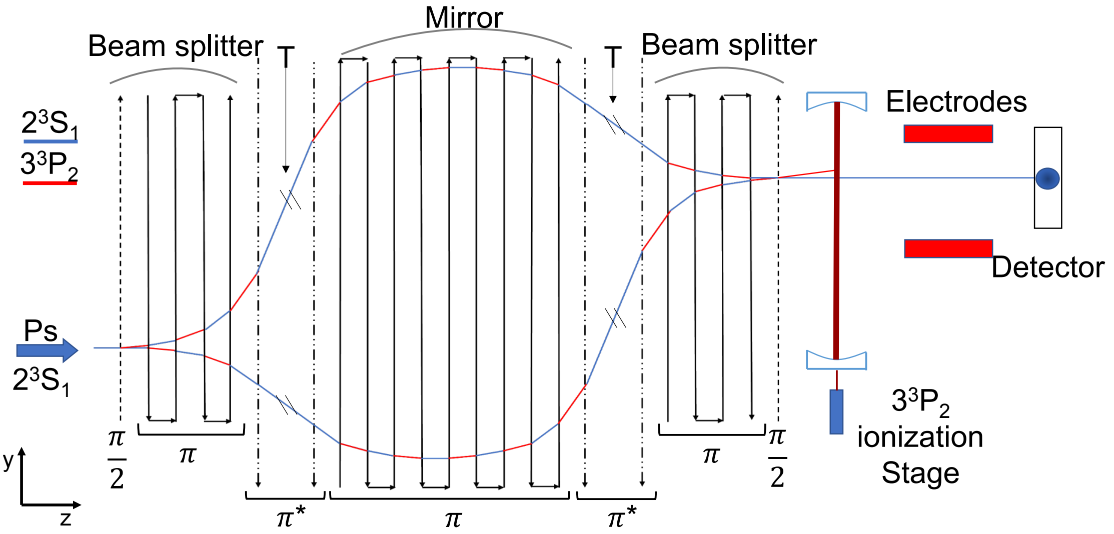

Figure 4.1: Scheme of the light pulse interferometer with positronium. The Ps beam entering the apparatus propagates according to a laser-driven Mach-Zehnder scheme, in order to acquire a phase induced by the gravitational field. In the scheme, $\pi/2$ pulses act as beam splitters, π-pulses interchange the $n = 2$ states (in blue) with the $n = 3$ states in red, while slightly detuned π^*-pulses only act to suppress $n = 3$ states during the propagation. The gravitational deformations of the two interferometer branches have not been represented for simplicity.

Unlike the typical representation of interferometer diagrams, the Figure 4.1 does not refer to the space-time axis (co-ordinate along the axis of gravity versus time) but is fully spatial: this is due to the fact that Ps has a non negligible speed along the z direction and the design of this interferometer involves spatially separated laser pulses operating in a continuous regime which works well with both continuous and pulsed atomic beams. The working principle of this type of interferometer has been presented in Ref. [148].

First, let's note that the sequence of single-photon excitations for each type of pulse is done using the same beam, which is reflected and redirected towards the atomic beam. This implies that each interaction between atom and light occurs with an opposite wave vector and a different internal state. This expands the concept represented in Figure 2.2, creating a dual image: an atom in the ground state that interacts with a downward-propagating pulse gets excited, acquiring a downward recoil momentum, while an atom in an excited state that interacts with a downward-propagating pulse gets de-excited, acquiring an upward recoil momentum. By alternating beams propagating in opposite directions, it is possible to separate the wavefunctions, acting like a Bragg interferometer but with separated beams instead of overlapped ones.

After the first group of pulses, composed of a $\pi/2$-pulse and N_{bs} π-pulses, which act as a beam splitter, there is a π^*-pulse that plays the crucial role of bringing both branches of the interferometer to the $n = 2$ state. In this region (interrogation), the atomic wavefunctions must propagate for a time T long enough to accumulate a significant phase shift for the measurement. The lifetime of the $n = 3$ state is too short to allow particles in one of the two arms to propagate for a time equal to T without annihilating, so we need to exploit the $n = 2$ state in both branches.

After the first interrogation, a set of π-pulses acts as mirrors and precedes two more π^*-pulses needed to prepare the second part of the interrogation. At the end of the interferometer, the second beam splitter function is performed again by π and $\pi/2$ pulses, used to recombine the wavefunctions.

By setting the Rabi frequency of the π^*-pulse as

$$\Omega_{\text{eg}} = \frac{(N_{\text{bs}} + 1)\hbar k^2}{m\sqrt{3}} \tag{4.1}$$

it is possible to make it act as a π-pulse on one of the two arms of the interferometer and as a 2π-pulse on the other [148].

For the correct operation of the π^*-pulse, it is necessary that the Ps transition probability is zero for a given value of the atom momentum, which can be obtained by a suitable shaping of the laser spatial profile, in the form of a square pulse. This can be implemented by means of top-hat shaping lenses [152]; given the intensity of the flat-top laser beam in the form $I(r) = I_0 e^{-2(r/w)^l}$, where w is the beam waist and $l > 2$, the simulations have shown that the value $l = 6$ would be adequate for an efficient π^*-pulse [153,154]. π and $\pi/2$ pulses have the same wavelength of 1312 nm, while π^*-pulses are slightly detuned from the transition to work at the maximum transition probability for the $n = 3$ states: $\omega_{\pi^*} = \omega_{\text{L}} + \frac{\hbar(N_{\text{bs}}+1)^2k^2}{2m}$.

Having a set of pulses instead of a single one creates a difference with the definition of T from Chapter 2, which can be more or less pronounced depending on the operational parameters of the interferometer. Indeed, we can always consider T as the interrogation time interval (the interval during which most of the gravity-induced phase shift occurs), but the preceding time interval, necessary to traverse the beam splitter, can no longer be considered negligible and can significantly impact the decay of the atomic beam. This time interval clearly depends on the arrangement and shape of the pulses and is given by:

$$\Delta t_{\mathrm{bs}} = \frac{2\Delta z_{\pi/2} + 2N_{\mathrm{bs}}\Delta z_{\pi} + 2\Delta z_{\pi*}}{v_z} \tag{4.2}$$

where Δz is a length grater than (and proportional to) the waist of the pulses, N_{bs} is the number of π-pulses in the beam splitter, and v_z is the velocity of the atoms along the z direction. In the equation, we have considered a distance between the centers of the pulses equal to $2\Delta z$.
To close the paths, the entire interferometer can be related to the number of π-pulses chosen in the splitter. Assuming that the pulses are alternated and that $\pi/2$-pulses propagate upward and π^*-pulses propagate downward, the number of π-pulses needed in the mirror to close the circuit is $N_{\mathrm{mir}} = 2N_{\mathrm{bs}} + 1$. The time to traverse the mirror from π^* to π^* is therefore

$$\Delta t_{\mathrm{mir}} = \frac{(2N_{\mathrm{bs}} + 1)2\Delta z_{\pi} + 4\Delta z_{\pi*}}{v_z} \tag{4.3}$$

In this configuration, we define the effective wave vector as the sum of the momenta transferred to the wavefunction of the upper branch minus those of the lower branch at the beginning of the interrogation region, i.e., after the beam splitter:

$$\begin{aligned} k_{\mathrm{eff}} &= \frac{\Delta p(t_{\mathrm{bs}})}{\hbar} = \sum_i^{\mathrm{top,BS}} \frac{p_{\mathrm{r},i}}{\hbar} - \sum_i^{\mathrm{bot,BS}} \frac{p_{\mathrm{r},i}}{\hbar} \\ &= k_{\pi/2} + N_{\mathrm{bs}}k_{\pi} + k_{\pi*} - (-N_{\mathrm{bs}}k_{\pi}) = 2(N_{\mathrm{bs}} + 1)k \end{aligned} \tag{4.4}$$

where the signs account for the different effects on different internal states and it is assumed that $k = k_{\pi/2} = k_{\pi} \simeq k_{\pi*}$.

From the quantities presented so far, several fundamental parameters emerge in the design of the interferometer: the effective wave vector, directly linked to the number of pulses in the beam splitter N_{bs}, and the propagation time T, which is related to the velocity of the atomic beam v_z. Additionally, there is the propagation time through the entire interferometer, which depends on both N_{bs} and v_z:

$$\Delta t_{\mathrm{SPLMT}} = 2\Delta t_{\mathrm{bs}} + 2T + \Delta t_{\mathrm{mir}} = \frac{2\Delta z_{\mathrm{p}}(4N_{\mathrm{bs}} + 7)}{v_z} + \frac{\Delta z_{\mathrm{T}}}{v_z} \tag{4.5}$$

where we have assumed $\Delta z_{\mathrm{p}} = \Delta z_{\pi/2} = \Delta z_{\pi} \simeq \Delta z_{\pi^*}$ and Δz_{T} is the interrogation space. In reality, Δz_{π^*} is greater than $\Delta z_{\pi/2}$ and Δz_{π}, but this does not affect the substance of the discussion.

One way to optimize the interferometer is to minimize its sensitivity, defined as the minimum detectable value of gravitational acceleration, which is given by [21]:

$$\Delta g = \frac{1}{C\sqrt{N_{\mathrm{Ps}}}k_{\mathrm{eff}}T^2} \tag{4.6}$$

where C is the contrast of the interferometer and N_{Ps} is the number of atoms detected downstream of the interferometer.
This formula already reveals the most critical aspect of the experiment: to measure gravitational acceleration with good precision, we need a high-flux source of positronium atoms.
The number of atoms reaching the detector decreases due to annihilation and decay throughout the various stages of the experiment:

- Exiting the $\mathrm{e}^+/\mathrm{Ps}^-$ converter and propagating to the photodetachment cavity
- Propagating to (state $n = 1$) and beyond the UV-microwave excitation (state $n = 2$)
- Propagating through the interferometer (states $n = 2$ and $n = 3$)

Considering that atoms spend the same amount of propagation time through the beam splitters and mirrors in states $n = 2$ and $n = 3$, we can estimate the behavior of the number of detected atoms as:

$$\frac{N_{\mathrm{Ps}}}{N_0} \propto \exp\left(\frac{-\Delta z_{\mathrm{pd}}}{v_z \tau_{\mathrm{Ps}^-}}\right) \exp\left(\frac{-\Delta z_{\mathrm{ecc}}}{v_z \tau_{n=1}}\right) \exp\left(\frac{-\Delta z_{\mathrm{I}}}{2 v_z}\left[\frac{1}{\tau_{\mathrm{g}}} + \frac{1}{\tau_{\mathrm{e}}}\right]\right) \exp\left(\frac{-\Delta z_{\mathrm{T}}}{v_z \tau_{\mathrm{g}}}\right) \tag{4.7}$$

where Δz_{pd} and Δz_{ecc} are the propagation distances to reach the photodetachment and microwave cavities respectively, $\Delta z_{\mathrm{I}} = 2\Delta z_{\mathrm{p}}(4N_{\mathrm{bs}} + 7)$, and g and e denote the states with $n = 2$ and $n = 3$ respectively. In the equation, we have ignored the less probable decay channel $n = 3 \rightarrow n = 1$ (see Figure 1.1). To optimize the interferometer, one could substitute equations 4.7 and 4.4 into equation 4.6 and calculate:

$$\nabla_{N_{\mathrm{bs}}, v_z}(\Delta g) = \left(\frac{\partial(\Delta g)}{\partial N_{\mathrm{bs}}}, \frac{\partial(\Delta g)}{\partial v_z}\right) = 0 \tag{4.8}$$

For a more realistic sensitivity estimate, it is also necessary to consider the dependence of C on N_{bs} and eventually v_z. As we will do in this treatment for the chosen operating conditions, this can be estimated using a Monte Carlo method that includes the velocity and position distributions of the atomic beam.

However, as mentioned, some stages of the experiment, that have not been addressed in this research work, are in the planning stage, and this implies that some constraints may lead to variable values. For this reason, it is preferable for now to follow the approach in Ref. [151], which involves designing an interferometer to provide realistic estimates of operational parameters and achievable results based on available data, choosing experimentally feasible operating regime. We therefore leave the search for the exact optimal point to future development, with the understanding that the following discussion provides a good approximation relative to the current state of the art.

As mentioned, it is preferable to have a high T, but reducing v_z means increasing losses before the interferometer. Therefore, we set the length of the interferometer to a relatively large but experimentally feasible value: $\Delta z_\mathrm{I} + \Delta z_\mathrm{T} \simeq 5$ m.

To achieve a gain in the annihilation of the $n = 3$ state, we require $2\Delta t_\mathrm{bs} + \Delta t_\mathrm{mir} \ll T$. However, this implies a small N_bs, contrary to what is desired. Considering that a very high N_bs would make it experimentally challenging to control the number of pulses, we decide to fix $N_\mathrm{bs} = 4$. Taking into account the interrogation time, annihilation, and de-excitation processes, a suitable energy for the Ps could be 200 eV ($\simeq 6 \times 10^6$ m/s). Under these conditions, we have:

$$k_\mathrm{eff} = 10k,\ T \simeq 0.4\mu s \tag{4.9}$$

To obtain a 10 $\hbar k$ momentum separation between the wavefunctions, the device is composed by 23 pulses as shown in Figure 4.1. Assuming conventional gravity acceleration (9.81 m/s^2) is measured, the gravity-induced phase shift achievable with this interferometer is:

$$\Delta\phi_\mathrm{g} \simeq\ 84\,\mu rad \tag{4.10}$$

As metionend in Chapter 1, after crossing the interferometer, the weakly bound $n = 3$ state is laser-ionized using an Erbium fiber laser at 1560 nm. This ionization allows for the measurement of the number of $n = 2$ Ps atoms alone. The remaining charged particles (electrons and positrons) are removed by a moderate electric field performing a state selective detection which does not require spatial separation of the states. Achieving this separation would necessitate the addition of numerous pulses and extend the interferometer by several meters, leading to a substantial loss of the Ps beam due to annihilation.

Additionally, the interferometer tends to scatter atoms that have not properly interacted with the laser pulses. To improve the signal-to-noise ratio at the detector, a physical mask is used to select the area with the highest signal concentration.

4.1 Other phase shifts and differential measurement

Under the operating conditions described, we can evaluate the effect of the gravitational gradient presented in Section 2.1.1. Specifically, by applying Equation 2.25, we can estimate the perturbations relative to a hypothetical gravitational acceleration g and obtain:

$$\frac{g_1}{g_0} \simeq 1.7 \times 10^{-10}, \quad \frac{g_2}{g_0} \simeq 2 \times 10^{-29} \tag{4.11}$$

where we have considered $\bar{v_0} = v_{r,\mathrm{eff}}/2 \simeq 1.4 \times 10^3$ m/s. These values are far beyond the target sensitivity of this experiment at its current stage and will therefore be

neglected.
Additionally, it is noteworthy that the high recoil velocity is another distinctive feature of working with the Ps atom, which has an extremely low mass compared to typical experiments of this kind.

Applying Equation 2.31, we can evaluate the effect of Earth's rotation on the phase shift of the wavefunctions. Considering the current location of the laboratory (Sesto Fiorentino, Florence, Italy), the latitude to use is $\theta_l = 43°50'07''N$. With $\Omega = 7.29 \times 10^{-5}$ rad/s, $k_{\text{eff}} = 7.6 \times 10^6\ \text{m}^{-1}$, and assuming the propagation direction of the Ps is aligned West-East, we obtain $\Delta\phi_c \simeq 0.88\,\text{mrad}$. This represents the most unfavorable condition, mainly due to the higher velocity spread, as shown in Figure 3.18b.

However, if we align the interferometer perpendicularly to the West-East axis, the phase shift would be dominated by the transverse spread of the beam. Using the values from section 3.2, this would result in $\Delta\phi_c < \Delta\phi_g$, allowing to distinguish the interference fringes. Nonetheless, this phase shift must be carefully characterized and taken into account in the analysis of the measurement.

An atom interferometer is generally subjected to phase shifts that are either independent or dependent of the effective wavevector, some of which have been mentioned in this work. Among the k-independent phase shifts are those related to perturbations of the internal degrees of freedom of the atoms, such as magnetic field gradients and single-photon Stark shifts caused by non-resonant light, as well as laser phase noise.

Another important effect is due to wavefront distortions of the laser pulses, which can introduce phase shifts dependent on the atomic trajectories. Imperfections in the wavefront convolve with the spatial and velocity distribution of the atoms, causing complex phase shifts [155]. Quantifying the phase shifts and phase noise of the interferometer is beyond the scope of this discussion, which instead aims to estimate the contrast and some operational parameters of the system. However, we will briefly discuss a possible method, compatible with the proposed interferometric configuration, to reject certain undesired phase shifts.
To isolate these shifts, measurements can be taken with the effective wavevector oriented upwards and downwards:

$$\begin{cases} \Delta\phi_{\uparrow} = k_{\text{eff}} g T^2 + \Delta\phi_{\text{dep}} + \Delta\phi_{\text{indep}} \\ \Delta\phi_{\downarrow} = -k_{\text{eff}} g T^2 - \Delta\phi_{\text{dep}} + \Delta\phi_{\text{indep}} \end{cases} \tag{4.12}$$

The sum of the measurements allows for the isolation of the phase shifts that are independent of the direction:

$$\Delta\phi_{\text{indep}} = \frac{\Delta\phi_{\uparrow} + \Delta\phi_{\downarrow}}{2} = \frac{\Delta\Phi^+}{2} \tag{4.13}$$

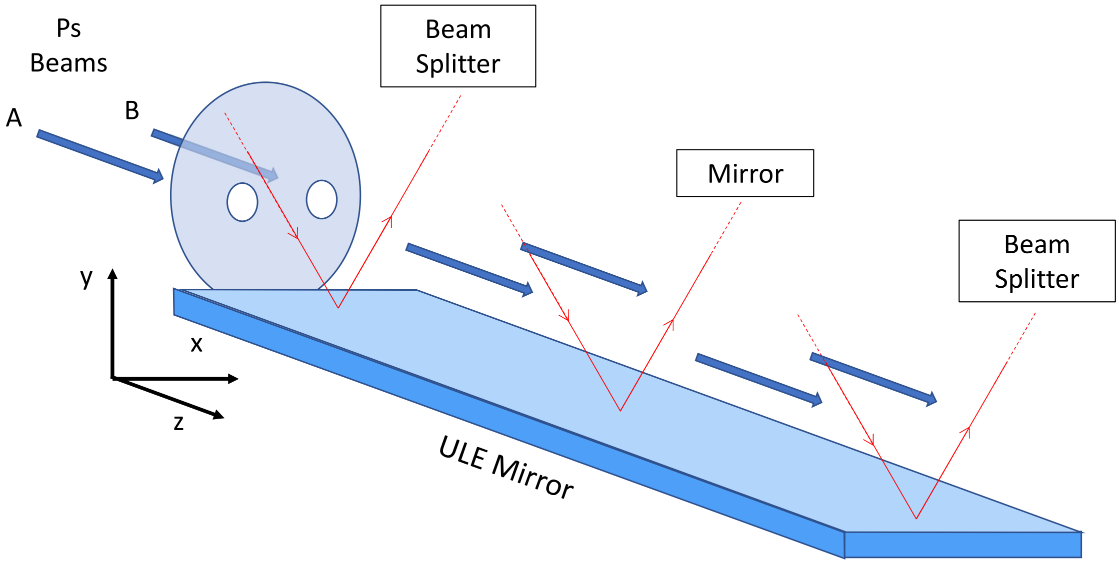

Figure 4.2: Scheme of the differential measurement strategy on the subdivided Ps beam. The laser radiation hits the two beams A and B with opposite momentum to reject the phase noise. For simplicity, only three pulses are shown here, but the strategy is designed for all the 23 pulses of the interferometer.

while the difference allows for the determination of the dependent phase shifts and the calculation of the gravitational acceleration:

$$k_{\text{eff}} g T^2 + \Delta\phi_{\text{dep}} = \frac{\Delta\phi_{\uparrow} - \Delta\phi_{\downarrow}}{2} = \frac{\Delta\Phi^{-}}{2} \tag{4.14}$$

The proposed interferometer has no control over the laser phase noise and would require an accuracy on the positioning of the optical components that could exceed the experimental possibilities. The same problem arises in the reference literature of gravitation with Ps [21,22] where sub-nm accuracy is required in gratings placement. It is proposed to solve the issue by extracting the phase signal with a differential method just mentioned [156,157]: a double measurement can be performed by splitting the Ps beam in two and having the laser pulses hitting the beams from opposite directions, as is shown in Figure 4.2.

This configuration works effectively as a couple of Positronium interferometers, each making use of two identical beam; two independent $n = 2$ population set can therefore be measured during the same data taking, so that the phase can be extracted from the Lissajous plot of the two combined populations, similar to what was done for atomic gravitation in Ref. [156]. As can be seen from the equation 4.14, the additional advantage of this strategy is the doubling of the signal which becomes proportional to $2k_{\text{eff}} g T^2$ [158]. In the proposed configuration the reflection mirror for the double measurement covers the whole length of the interferometer and is suspended by anchors designed to minimize deformations. Given its high spatial extension, the interferometer could be subject to thermal drifts and mechanical stresses, especially on the reflection mirror. It is possible to significantly reduce these effects by making the mirror with ultra-low expansion (ULE) material.

In general, we can separate the k-dependent phase shift into two contributions that depend or do not depend on the interrogation time T:

$$\Delta\phi_{\text{dep}} = \Delta\phi(k_{\text{eff}}, T) + \Delta\phi(k_{\text{eff}}) \tag{4.15}$$

Any interferometer phase shifts that depend on k but not on T (e.g., given by possible deformations of the mirror in the transverse direction) can be reduced by following the described sequence with two different Ps velocities, e.g., 6×10^6 m/s and 1.2×10^7 m/s, obtained by changing the acceleration potentials of the electrodes. When the interferometer is run with twice the Ps speed, the interrogation time scales from T to $T/2$ and by measuring the difference between the two cases of slow and fast beam, one obtains a 1.5 final gain on the signal:

$$\begin{aligned}
&\Delta\Phi_{\text{dd}} = \Delta\Phi^{-}_{\text{Slow}} - \Delta\Phi^{-}_{\text{Fast}} = \\
&2\left[k_{\text{eff}} g T^2 + \Delta\phi(k_{\text{eff}}, T) + \Delta\phi(k_{\text{eff}})\right] - 2[k_{\text{eff}} g \left(\frac{T}{2}\right)^2 + \Delta\phi\left(k_{\text{eff}}, \frac{T}{2}\right) + \Delta\phi(k_{\text{eff}})] \\
&= \frac{3}{2} k_{\text{eff}} g T^2 + 2\left[\Delta\phi(k_{\text{eff}}, T) - \Delta\phi\left(k_{\text{eff}}, \frac{T}{2}\right)\right]
\end{aligned} \tag{4.16}$$

where the substript "dd" stands for double differential. Once the phase shifts of both measurements have been obtained by analyzing the two differential signals, the final value of the phase difference is obtained by simple subtraction.

4.2 SPLMT interferometer simulations

In this section, I will describe the simulation of the interferometer discussed previously, aiming to estimate the contrast and data acquisition times, also called integration times, that are crucial for assessing the feasibility of the experiment. The simulation for estimating the contrast has been performed using the Monte Carlo method within a semiclassical (quantum amplitude probabilities with classical particles) framework for various atomic beam distributions. Additionally, a quantum simulation has been conducted to evaluate the effect of parasitic interferometers, which will be briefly explained in Section 4.2.3.

4.2.1 Amplitude probabilities and simulation setting

The core part of the simulation concerns the interaction between the laser pulses and the atomic wavefunctions defined by

$$|\Psi\rangle = \sum_q c_{\mathrm{g},2q} e^{-i\omega_{\mathrm{g},2q}t} |g, 2q\hbar k\rangle + c_{\mathrm{e},2q+1} e^{-i\omega_{\mathrm{e},2q+1}t} |e, (2q+1)\hbar k\rangle \tag{4.17}$$

where $k = \mathbf{k}_\mathrm{L} \cdot \hat{y}$ and q is a momentum index which allows us to summarize all possible momentum states ($q \in \mathbb{Z}$). As in Chapter 2, the expression $|\alpha, l\rangle$ refers to a generic state, where α indicates the energy level (ground, g, or excited, e, which correspond to $2^3\mathrm{S}_1$ and $3^3\mathrm{P}_2$ respectively) and l is the momentum. For brevity, we omit the initial momentum of the atom, p, in the subscripts and in the kets, which is determined by the atomic beam velocity distribution at the interferometer entrance. Thus, $\omega_{\alpha,l}$ is defined as:

$$\omega_{\alpha,l} = \omega_\alpha + \frac{(p + l\hbar k)^2}{2\hbar m} \tag{4.18}$$

Since in the center-of-mass reference frame the initial Ps state is $|g, 0\rangle$, l is even for ground states and odd for excited states. In general, the summation over q is infinite, but only the states having q between $-(N-1)$ to $N-1$ will be populated, where N is the number of pulses. The amount of momentum states to be considered for the simulations is therefore $2N$.

The interaction Hamiltonian of the system has a significant difference compared to that of the Bragg interferometer (equation 2.50), specifically that the action of the upward and downward propagating fields is not simultaneous. This means that we need to define two different Hamiltonians for the two propagation directions, which should not be summed but rather considered individually:

$$\begin{aligned} \hat{H}_L^\uparrow &= \frac{\hbar\Omega_{\mathrm{eg}}}{2}\left(e^{i(ky-\omega_\mathrm{L}t-\phi)} + e^{-i(ky-\omega_\mathrm{L}t-\phi)}\right) \\ \hat{H}_L^\downarrow &= \frac{\hbar\Omega_{\mathrm{eg}}}{2}\left(e^{i(-ky-\omega_\mathrm{L}t-\phi)} + e^{-i(-ky-\omega_\mathrm{L}t-\phi)}\right) \end{aligned} \tag{4.19}$$

By solving the Schrödinger equation with $|\Psi\rangle$ and considering that the laser action flips the internal state and changes the momentum states according to equation 2.33 we note that the interaction couples the momentum states pairwise, and this coupling changes sign by ±$\hbar k$ depending on the direction of the Hamiltonian:

$$\begin{aligned} \hat{H}_L^\uparrow &\propto \sum_q \left[e^{-i(\omega_\mathrm{L}t+\phi)} |e, (2q+1)\hbar k\rangle \langle g, 2q\hbar k| + e^{i(\omega_\mathrm{L}t+\phi)} |g, 2q\hbar k\rangle \langle e, (2q+1)\hbar k|\right] \\ \hat{H}_L^\downarrow &\propto \sum_q \left[e^{i(\omega_\mathrm{L}t+\phi)} |g, 2q\hbar k\rangle \langle e, (2q-1)\hbar k| + e^{-i(\omega_\mathrm{L}t+\phi)} |e, (2q-1)\hbar k\rangle \langle g, 2q\hbar k|\right] \end{aligned} \tag{4.20}$$

Furthermore, the solution of the Schrödinger equation yields a system very similar to that in equation 2.38, with the difference being the detunings that vary according to the direction of the laser:

$$\uparrow\colon \begin{cases} i\dot{c}_{\mathrm{e},2q+1} = \frac{\Omega_{\mathrm{eg}}}{2} c_{\mathrm{g},2q} e^{-i(\delta^{\uparrow} t+\phi)} \\ i\dot{c}_{\mathrm{g},2q} = \frac{\Omega^*_{\mathrm{eg}}}{2} c_{\mathrm{e},2q+1} e^{i(\delta^{\uparrow} t+\phi)} \end{cases} \qquad \downarrow\colon \begin{cases} i\dot{c}_{\mathrm{e},2q-1} = \frac{\Omega_{\mathrm{eg}}}{2} c_{\mathrm{g},2q} e^{-i(\delta^{\downarrow} t+\phi)} \\ i\dot{c}_{\mathrm{g},2q} = \frac{\Omega^*_{\mathrm{eg}}}{2} c_{\mathrm{e},2q-1} e^{i(\delta^{\downarrow} t+\phi)} \end{cases} \tag{4.21}$$

where

$$\begin{aligned} \delta^{\uparrow} &= \Delta - \left[\left(2q + \frac{1}{2}\right)\frac{\hbar k^2}{m} + \frac{pk}{m}\right] \\ \delta^{\downarrow} &= \Delta + \left[\left(2q + \frac{1}{2}\right)\frac{\hbar k^2}{m} + \frac{pk}{m}\right] \\ \Delta &= \omega_{\mathrm{L}} - (\omega_{\mathrm{e}} - \omega_{\mathrm{g}}) \end{aligned} \tag{4.22}$$

The systems 4.21 must be calculated alternately (the lasers change direction alternately) for each interaction and for each state and, given the time dependence of the Rabi frequency, the system has to be integrated numerically (e.g. using a 4-th order Runge-Kutta method).
In the expressions for the detunings, the presence of the Doppler effect caused by the initial velocity distribution of the atomic beam is evident, along with the term dependent on q. As the atom progresses along the interferometer, higher momentum states begin to populate (q increases), leading to an increasing detuning that decreases the transition probability. This is the reason for the link between contrast and k_{eff}.

4.2.2 Pulse parameters and efficiencies

As we saw in equation 2.42 (which is valid for square pulses instead of Gaussian pulses but offers general considerations), the probability of transition from one state to another depends on the Rabi frequency (and thus the laser power) and the interaction time. For a fixed atom velocity, this depends on the longitudinal waist of the pulse w_z. One way to make the transition more robust against the Doppler effect is to increase the interaction bandwidth of the pulse ($1/\tau$) by reducing w_z and increasing the beam power. In Figure 4.3a, the transition probability is plotted as a function of the Doppler effect due to the atom's initial velocity for different values of w_z: the curve broadens as w_z decreases. This effect can be understood as the tendency of the atom to misinterpret the pulse frequency when it becomes less distinguishable due to the short interaction time, attributing it also to frequencies near the resonance.

However, simultaneously, we want a larger transverse waist dimension w_x to maximize the interaction region between the pulse and the atomic beam. Therefore, for the interferometer, we chose a cylindrical pulse with $w_x > w_z$. Considering experimental limits on asymmetry beyond which the beam might become too deformed, we selected $w_x = 1.4$ mm and $w_z = 0.16$ mm for the $\pi/2$ and π-pulses, and $w_x = 1.8$ mm and $w_z = 1.13$ mm for the π^*. With these waists, the selected optical pulse powers are lower than 30 W and, if needed, are achievable with coherent combination techniques [159, 160].

Figure 4.3b reports the transition probability from one state to another, given by $|c_\mathrm{g}|^2$ or $|c_\mathrm{e}|^2$, as a function of δ. Since the Ps Doppler shift is included in δ, 4.3 also indicates the robustness of the pulses to Doppler effects: the wider the curves, the more robust the interferometer is. The pulse most sensitive to the Doppler effect is certainly the π^*. Let's define the interferometer efficiency as the product between the $\pi/2$ pulse efficiency and the geometric mean of the mirror efficiencies of the upper and lower branches:

$$\eta = \eta_{\pi/2}\sqrt{\eta_\mathrm{top}\eta_\mathrm{bot}} \tag{4.23}$$

Given that the pulse transition probability after an atom-pulse interaction, $\mathrm{P_t}$, is the square modulus of the probability amplitude of the target atomic state (for instance, e) normalized by the probability amplitude of the starting atomic state (for instance, g), we can define the efficiency of the upper and lower branch as the product of the transition probabilities of all the π and π^*-pulses in the branch:

$$\eta_\mathrm{top} = \prod_\mathrm{top} P_\mathrm{t}^{\pi} P_\mathrm{t}^{\pi^*}, \eta_\mathrm{bot} = \prod_\mathrm{bot} P_\mathrm{t}^{\pi} P_\mathrm{t}^{\pi^*} \tag{4.24}$$

Instead, the efficiency of the splitters is defined by

$$\eta_{\pi/2} = 4\sqrt{(1-P_\mathrm{t,1}^{\pi/2})P_\mathrm{t,1}^{\pi/2}(1-P_\mathrm{t,2}^{\pi/2})P_\mathrm{t,2}^{\pi/2}}, \tag{4.25}$$

where $P_\mathrm{t,1}^{\pi/2}$ and $P_\mathrm{t,2}^{\pi/2}$ are the transition probabilities of the two $\pi/2$ pulses. η_top, η_bot and $\eta_{\pi/2}$ represent the probability of an atom to interact correctly with the pulses in the upper and lower branches and in splitter stages respectively. Note that all probabilities P_t vary along the interferometer due to the Doppler effect resulting from momentum transfer from the pulses to the Ps. This implies that even a perfectly collimated beam cannot achieve unit efficiency unless each pulse is detuned by an amount equal to the recoil frequency, which is a complex experimental condition.

In order to have an estimate of the admissible divergence, the efficiency as a function of Ps entrance angles and coordinates has been studied, and the results are presented in 4.4: the efficiency is almost 0 at about 250 μrad while it is still high for an atom entering the interferometer at 0.25 mm from the centre of the entrance hole. The dependence of efficiency on Ps energy begins to decrease significantly at about 25 eV from the design value (200 eV), and since Ps is expected to have an energy spread of the order of ±10 eV [49, 86, 161, 162] (see also Figure 3.18), which

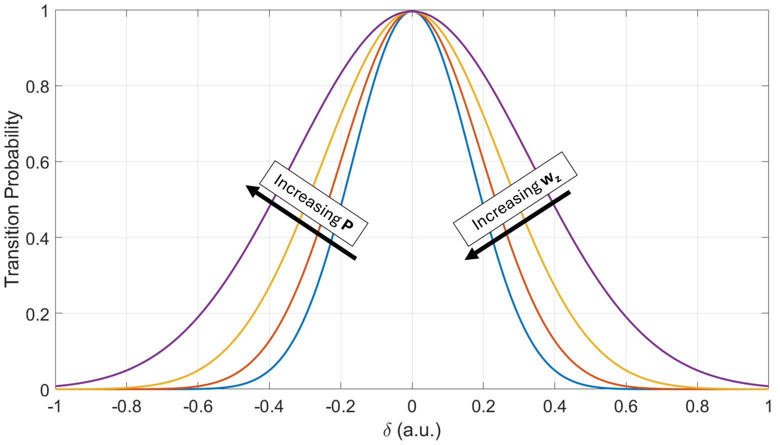

(a) Behavior of transition probability after an interaction with a π-pulse as a function of the detuning due to non null atom velocity, for different values of w_z and power. Decreasing the waist size widens the curves, making the pulses more robust against Doppler effects.

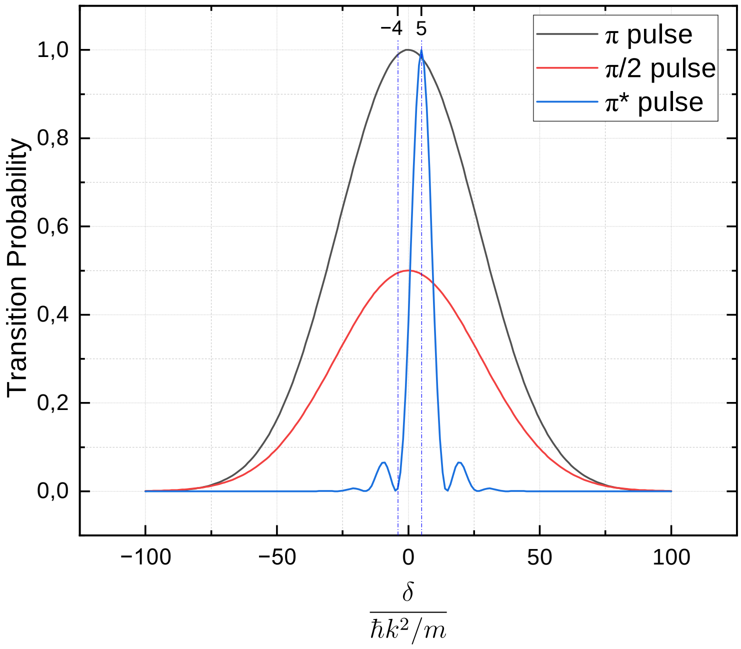

(b) Transition probability between the $n = 2$ and $n = 3$ states as a function of the ratio between the detuning and the recoil frequency. The π^*-pulse detuning is also shown: it acts as a 2π-pulse for the interferometric wavefunction which absorbed 4 photons with negative momentum, giving zero transition probability, and as a π-pulse for the wavefunction which absorbed 5 photons with positive momentum.

Figure 4.3: Transition probabilities for pulses under different operating conditions and for different pulse types.

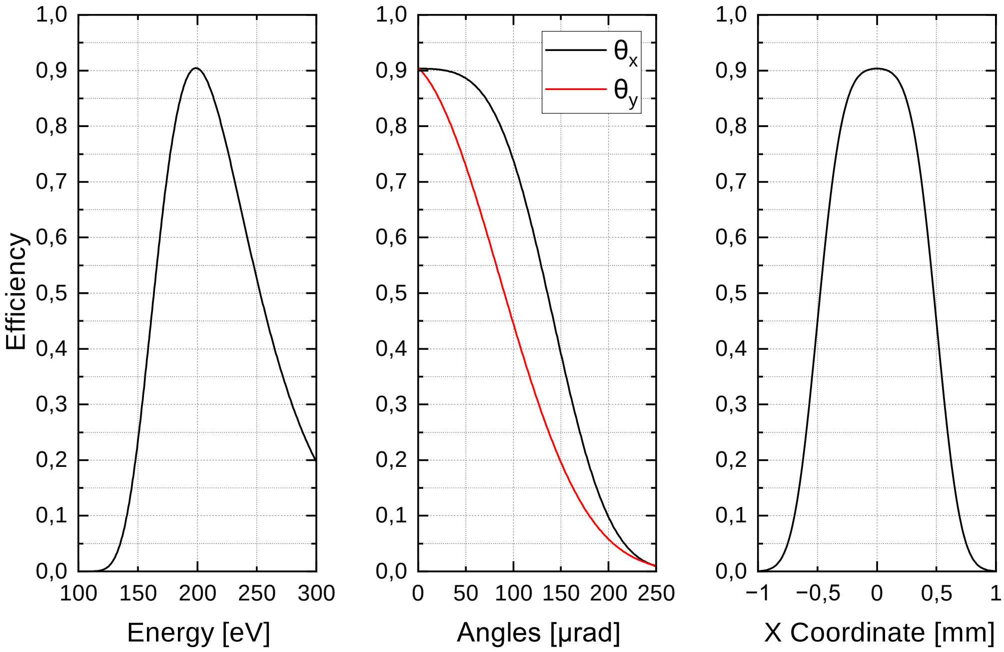

Figure 4.4: Interferometer efficiency as a function of Ps energy, entrance angles and position.

corresponds to a decrease in efficiency of less than 5%, it is not critical in this experiment.

These results explain the choice of aligning the polarization of the laser field for photodetachment along the propagation direction so as to direct the maximum velocity spread on the interferometer axis more robust to the Doppler effect. Moreover, based on these results and by trying different values, an optimal size of the mask to be placed in front of the detector so as to select input angles less than 100 μrad has been found.

4.2.3 Quantum simulation for parasitic interferometers

An atom that crosses the interferometer can be represented by a wavefunction populating two different energy and momentum states after an interaction with a pulse. The two states separate spatially along the propagation thus defining two distinct trajectories. Although this splitting should occur only at the $\pi/2$-pulses, the non-ideality of the beams causes it to happen at every pulse. By applying this process to the entire interferometer, one obtains that the maximum number of trajectories is equal to 2^N, which is about 8 million for the interferometer proposed in this work. The effective number is reduced if we consider that two states recombine when they spatially overlap.

From now on we will call the wavefunction path indicated in Figure 4.1 as "main pattern" and all other paths as "parasitic pattern" or "parasitic trajectories". The

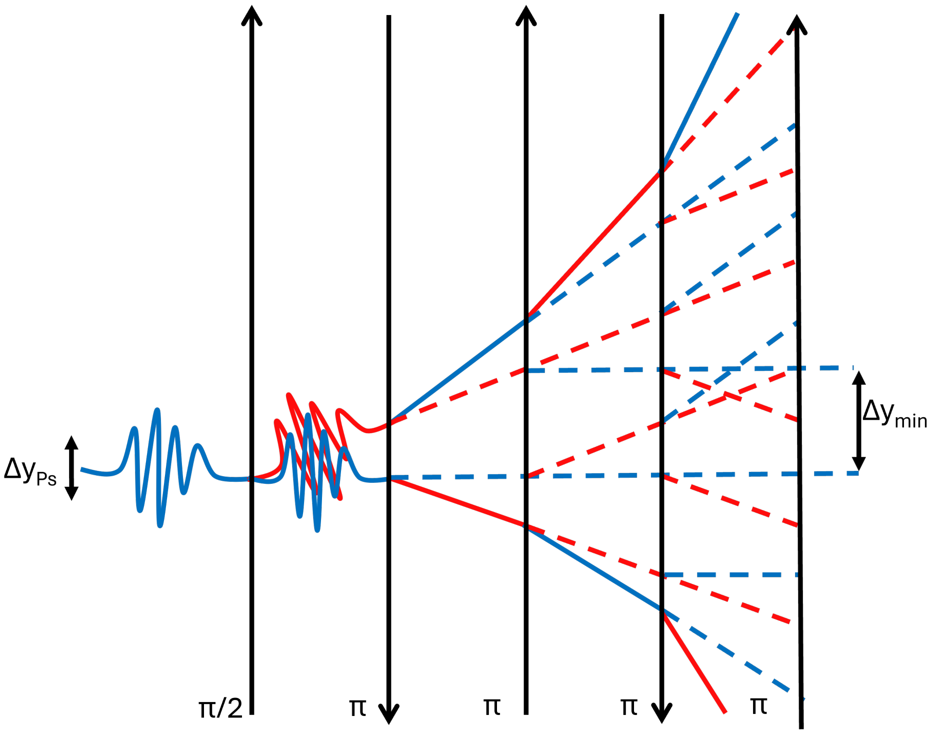

Figure 4.5: Representation parasitic patterns (dashed lines) generation due to the imperfections of the first 5 pulses of the interferometer. Lines with the same color and inclination represent states with the same internal state and momentum propagating along different trajectories. If the coherence length of Ps, Δy_{Ps}, is greater than the minimum separation Δy_{min}, interference occurs between at least two states. Wavefunctions are represented by lines for clarity.

main one corresponds to an ideal atom-pulses interaction pattern, and is the most probable if the interferometer is well sized. On the other hand, the parasitic pattern represents all other trajectories arising from losses in the single interactions. The gravitational information is contained only in the main pattern while the parasitic one contributes to the noise. Given the high number of parasitic trajectories, it is not possible to define a priori how many and which of these interfere with each other or with the main pattern, changing its phase and therefore the gravitational information. This issue was studied by a full quantum-mechanical simulation of the interferometer, which independently traces each trajectory and sums up the probability amplitudes in case of spatial superposition inside a pulse (which is in the present case the intersection between the trajectories [163]). We can generally describe the problem in quantum mechanical terms as

$$|\Psi_n\rangle = \hat{O}_n |\Psi_0\rangle \,, \tag{4.26}$$

where Ψ_n and Ψ_0 are the wavefunctions at the beginning of the interferometer and after the n-th pulse, where n ranges from 1 to N. $\hat{O}_n$ is the operator expressing the action of the pulses. Starting with Ps in the ground state with zero momentum (with respect to its center-of-mass) we have $|\Psi_0\rangle = |g, 0\rangle$, while for $|\Psi_n\rangle$:

$$|\Psi_n\rangle = \sum_{q=-Q_n}^{Q_n} \left(c_{n,\mathrm{g},q}(t)\,|g, 2q\hbar k\rangle + c_{n,\mathrm{e},2q+1}(t)\,|e, (2q+1)\hbar k\rangle\right) \tag{4.27}$$

In equation 4.27, $c_{n,\alpha,l}$ is the probability amplitude of the α internal state with momentum l after the n-th pulse and $Q_n = \frac{n-1}{2}$ if n is odd or $Q_n = \frac{n}{2}$ if n is even. Note that each state contains a high number of trajectories: $|\alpha, l\rangle = \sum_{j=1}^{J} c_{\alpha,l,j}\,|\alpha, l, j\rangle$, where j is the trajectory index and J is the total number of trajectories which depends on l (e.g., the states in which more trajectories converge are those with l close to 0). Putting it all together we get

$$|\Psi_n\rangle = \sum_{q=-Q_n}^{Q_n} \left(\sum_{j=1}^{J(2q)} c_{n,\mathrm{g},2q,j}(t)\,|g, 2\hbar k, j\rangle + \sum_{j=1}^{J(2q+1)} c_{n,\mathrm{e},2q+1,j}(t)\,|e, (2q+1)\hbar k, j\rangle \right). \tag{4.28}$$

The interferometric operator can be expressed as the product of the pulse operator $\hat{L}$ times the propagation operator $\hat{U}$ which expresses the free propagation of the wavefunction after the n-th pulse

$$\hat{O}_n = \prod_{i=1}^{n} \hat{L}_i \hat{U}_i \tag{4.29}$$

$\hat{L}$ is a $2N \times 2N$ matrix having all the elements of the main diagonal and some elements of the first supradiagonal and subdiagonal different from 0. These elements are computed by solving systems 4.21 for two coupled states with δ defined by equation 4.22. For example, considering a pulse propagating in the negative y direction, the states $|g, 2q\hbar k\rangle$ couple with the states $|e, (2q-1)\hbar k\rangle$, thus, just considering $q = 0$, the two coupled states are $|g, 0\rangle$ and $|e, -\hbar k\rangle$. Since systems 4.21 have no analytical solution, we cannot explicitly write the elements of the operator $\hat{L}$ but we can substitute it with the probability amplitudes of the states of the system that would result from applying the operator by solving 4.21 numerically. Collecting these amplitudes into a matrix $\tilde{L}$, for a pulse with a negative propagation direction and assuming that N is even, the matrix $\tilde{L}^{\downarrow}$ takes the form

$$\begin{bmatrix} c_{\mathrm{e},-(N-1)} & c_{\mathrm{g},-(N-2)\to e,-(N-1)} & \cdots & 0 & 0 \\ c_{\mathrm{e},-(N-1)\to g,-(N-2)} & c_{\mathrm{g},-(N-2)} & \cdots & 0 & 0 \\ \vdots & \vdots & \ddots & \vdots & \vdots \\ 0 & 0 & \cdots & c_{\mathrm{e},N-1} & c_{\mathrm{g},N\to e,N-1} \\ 0 & 0 & \cdots & c_{\mathrm{e},N-1\to g,N} & c_{\mathrm{g},N} \end{bmatrix} \tag{4.30}$$

where, for instance, $\left|c_{\mathrm{g},-(N-2)\rightarrow e,-(N-1)}\right|^2$ is the probability to have a transition from a ground state with $-(N-2)\hbar k$ to an excited state with $-(N-1)\hbar k$ after the pulse. $\left|c_{\mathrm{e},-(N-1)}\right|^2$ is the probability to find the atom in the same $|e,-(N-1)\hbar k\rangle$ state before and after the pulse. For a pulse with a negative propagation direction, the matrix elements $[\tilde{L}_{j,j};\tilde{L}_{j+1,j}]$ and $[\tilde{L}_{j,j+1};\tilde{L}_{j+1,j+1}]$ are solution of the systems 4.21 with $[c_{\mathrm{e},2q};c_{\mathrm{g},2q}]=[0;1]$ and $[c_{\mathrm{e},2q-1};c_{\mathrm{g},2q-1}]=[1;0]$ as initial condition for the Runge-Kutta integrator. The propagation matrix is a $2N\times 2N$ diagonal matrix whose elements are $e^{-iH_0t/\hbar}$ (free propagation). By computing equation 4.26 with a matrix product, it would be impossible to distinguish the probability amplitudes of different trajectories belonging to the same momentum state since they would be mixed (*total mixing*). In this condition, the assumption for which only overlapping trajectories sum up would not be respected. It is therefore necessary to set up a symbolic calculation that uses the propagation operator to distinguish the trajectories and sum up the probability amplitudes with a common propagator only (*selective mixing*). In this way we are basically summing up the interferometers that close with the main pattern. Figure 4.6 shows the amplitude probabilities of all states grouped in bins as a function of their position at the interferometer output. The two probabilities which correspond to the main pattern are in the highest bin, all the other bins correspond to the parasitic pattern. The total number of states is about 1100000 which, starting from the initial 2^N, has been reduced by recombination in closed patterns.

Since the path and interactions of the main pattern are known, it is possible to determine its probability amplitude in absence of interference by manually selecting the elements of $\tilde{L}$ and $\hat{U}$ belonging to this path. By comparing this result with the selective mixing it is possible to verify that they coincide, proving that the parasitic pattern negligibly interfere with the main one. For this reason, it was decided to resort to computationally cheaper simulations with a semi-classical approach discussed in section 4.2.4: each atom is described by a classical point-like particle that crosses the laser beams with which it interacts in the way described by the quantum treatment of the system 4.21.

This semi-classical method was compared with the selective mixing, showing that their efficiencies coincide, thus validating the results of the semi-classical simulation.

Note that the matching among the different type of recombinations considered is expected, as the influence of parasitic patterns increases with the inefficiency of the interferometer. This efficiency is maximal for an atom with no initial position offset and zero initial transverse velocities, as considered in this section. Discrepancies could become more pronounced at larger angles. If an atom of this type were to reach the detector after appropriately interacting with all the pulses, its phase might not be correlated with gravitational acceleration anyway, thereby adding noise to the measurement. This remarks the utility of a mask in front of the detector to

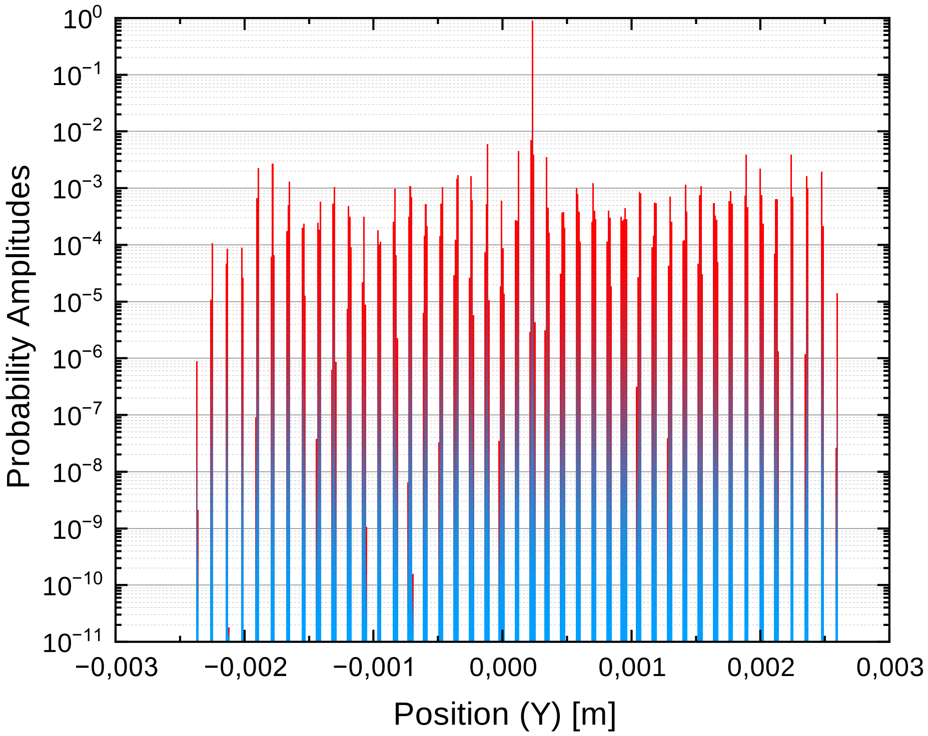

Figure 4.6: Probability amplitudes of the states corresponding to each possible trajectory for an atom with null entrance angles. The abscissa axis indicates the arrival position (y coordinate) at the detector of the Ps atoms having different trajectories. The highest bar represents the states that carry the gravitational information and the corresponding amplitude is about 0.92. The other bars represent the noise and the sum of their amplitudes covers the remaining probability, which is equal to 0.08.

filter out higher velocity classes and to select the atoms that carry the gravitational information.

What has been discussed so far represents the current state of this work, but the investigation of parasitic patterns has future developments in studying the intermediate case: the interference of parasitic patterns among themselves and with the main pattern for interferometers that close due to the broadening of the wave packet during propagation.

These analyses are interesting because parasitic patterns act as a loss channel for the interferometer. By appropriately configuring the spatial separation between pulses, it is possible to make them interfere destructively, thereby increasing the interferometer's efficiency [164]. This strategy requires the atomic wavefunctions to overlap throughout the interferometer to interfere, which is particularly relevant for positronium which, having a much smaller mass compared to typical atomic interferometry applications, is subject to significant atomic packet dilation.

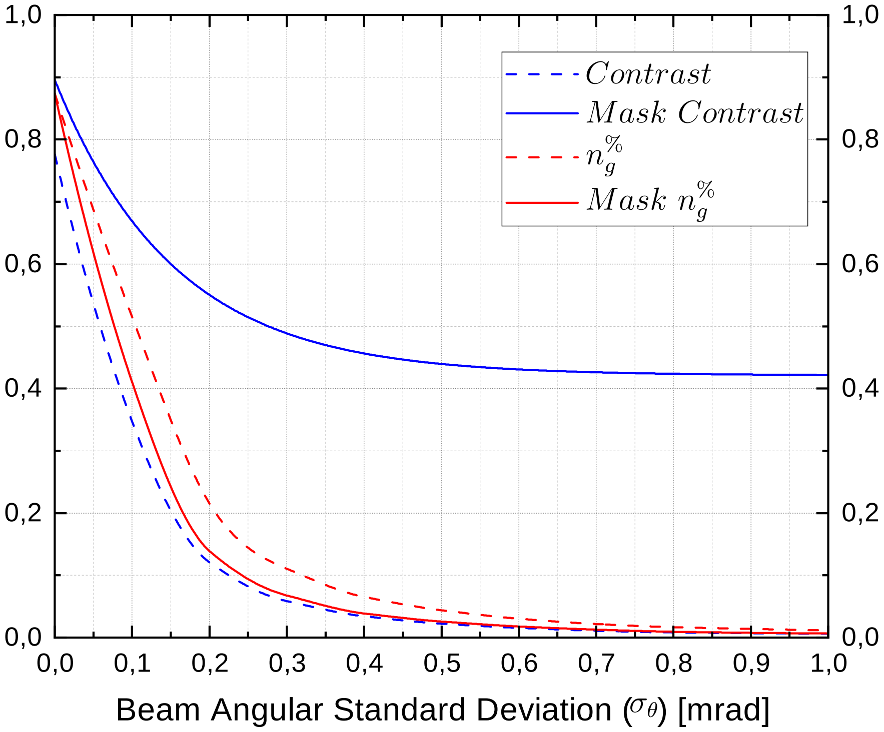

Figure 4.7: Contrast (blue) and percentage of atoms that have correctly crossed the interferometer (red) vs Ps beam angular standard deviation. The solid lines represent the statistics in a 1.5x1 mm^2 acceptance mask while the dashed ones correspond to the case of the whole screen (no mask). The contrast in the mask remains approximately constant and about 0.4 while the contrast of the whole detector tends to 0. The small difference between the percentage of "good" atoms (atoms that correctly crossed the interferometer) outside and inside the mask indicates the suitability of mask sizing.

4.2.4 Monte Carlo simulation

Since we are currently not focused on quantifying the phase shift (which may be useful in a later stage of the experiment when comparing results with simulations), we will only consider the contrast of the interferometer. Therefore, we treat the phase of the wavefunctions as a constant in each run, setting it to operate at a peak of the interference fringe.

In this algorithm the interaction between atom and laser, with consequent change of state, occurs in the case in which the transition probability between g and e is greater than a random number ranging from 0 to 1.
The Monte Carlo parameters of the positronium beam are the entrance angles and positions. The input coordinates have a uniform distribution on the entrance hole and the angular distributions are Gaussian. In this semi-classical approach, the annihilation and radiative decay were also modeled by comparing the probability

Table 4.1: ϵ ratio and interferometric contrast for different values of the beam angular standard deviation. All values have a relative error lower than 5%.

σ_θ **[mrad]**	ϵ	**C**
0.1	14%	60%
1	0.3%	40%
3	0.03%	40%
5	0.01%	40%
7	0.006%	40%
10	0.003%	40%

with a random number, like the laser-atom interaction, in every small step in which the space was divided (spatial mesh). The $n = 3$ Ps (n is the principal quantum number) can radiatively decay towards $n = 2$ or $n = 1$ with a probability equal to $1 - e^{-t/\tau}$, with $\tau_{3\to2} \simeq$89 ns and $\tau_{3\to1} \simeq$12 ns [52] while the $n = 2$ state radiatively decays into $n = 1$ in 0.24 s (the two-photon emission is the primary radiative decay mode) [165] and annihilates in 1.14 μs. It may happen that a Ps decays radiatively from $n = 3$ to $n = 2$ and then continues to run through the interferometer remaining in resonance with the laser excitation. In this case the atom loses the gravitational information, and it therefore adds noise on the detector. An atom that reaches the level with $n = 1$ continues to propagate until it decays or hits the detector, contributing to the noise. Each radiative decay involves the isotropic emission of a photon that randomly changes the atomic momentum.

In the proposed configuration the mask in front of the detector plays the important role of selecting atomic trajectories that typically tend to have a favourable interaction with the whole interferometer. Since Ps atoms failing the correct propagation have a lower probability of being accepted, the mask allows to clean up the accepted statistics in terms of fringe visibility (interferometric contrast), which can be set almost independently of the beam distribution.

If n_g is the number of atoms that correctly cross the interferometer and n_n is the number of atoms that fail the interferometer, we can define the percentage $n_\mathrm{g}^{\%} = \frac{n_\mathrm{g}}{n_\mathrm{g}+n_\mathrm{n}}\%$. In Figure 4.7 the contrast (blue curves) and $n_\mathrm{g}^{\%}$ (red curves) as a function of the Ps beam angular standard deviation, σ_θ, in presence (solid lines) and absence (dashed lines) of the mask are shown. Each point of the curves represents a run of the Monte Carlo simulation with different values of σ_θ. Here, the contrast (or visibility) is calculated as $\frac{n_\mathrm{g}-n_\mathrm{n}}{n_\mathrm{g}+n_\mathrm{n}}$, which holds if n_g is measured at a peak of the fringes by appropriately setting the phase shift of the wavefunctions.

After an initial decrease, the contrast with the mask stays approximately constant and equal to 0.4 while it tends to 0 without the mask. The difference between the percentage of signal with and without the mask is low, implying that the mask is well sized since it discards only a small part of the signal but a large amount of noise.

The effect of Ps decay is taken into account in the simulation, as can be appreciated by the difference between the initial values of the contrasts for a null σ_θ (perfectly collimated beam). In this case there is still some noise generated by decayed atoms reaching the detector at nonzero angles due to the decay recoil.

The minimum detectable acceleration value is defined by the sensitivity given in equation 4.6. Note that the mask reduces N_{Ps} but this effect is counteracted by the increase in C.

As discussed in section 3.2.3, it is reasonable to assume that the atomic beam can fit a Gaussian distribution with σ_θ ranging from 1 to 10 mrad on the angles and a uniform distribution extending for 0.25 mm in diameter on the entrance coordinates. Given the differential measurement (see equation 4.14) with two beams carrying the same number of atoms and taking into account the error propagation, the sensitivity to the gravitational acceleration g becomes

$$\Delta g = \frac{\sqrt{2}}{2C\sqrt{N_{\mathrm{Ps}}}k_{\mathrm{eff}}T^2} \tag{4.31}$$

The acquisition time can be defined as

$$t = \frac{N_{\mathrm{Ps}}}{\Phi_{\mathrm{Ps}}}\frac{1}{\epsilon} = \left(\frac{\sqrt{2}}{20kT^2\Delta gC}\right)^2 \frac{1}{\epsilon\Phi_{\mathrm{Ps}}} \tag{4.32}$$

where Φ_{Ps} is the Ps flux and ϵ is the ratio between the number of atoms entering the mask and the total number of atoms entering the interferometer. ϵ considers the annihilation and the probability that an atom ends up in the mask: $\epsilon = \epsilon_{\mathrm{ann}}\epsilon_{\mathrm{mask}}$.

Table 4.1 shows ϵ and contrast for different atomic beam divergences. For sigma greater than about 0.5 mrad, the mask begins to cut the beam at the interferometer exit while keeping constant the contrast and reducing ϵ. Note that the proposed detection method allows the interferometer to perform a "self-cleaning action" by removing from the mask the atoms that have lost the gravitational information. This effect is expressed by the behaviour of ϵ_{mask}: as σ_θ increases, ϵ_{mask} decreases by an amount not solely attributable to the different shape of the atomic beam but also to the scattering of the laser pulses. The advantage of this method is that while ϵ decreases, the contrast, on which the data acquisition time has a quadratic dependence, remains constant.

With an input flux of 0.5x10^8 Ps/s and $\sigma_\theta = 10$ mrad, one would obtain $\Delta g/g = 10\%$, which is significant for a fundamental physics test (see Chapter 1), in about 11 months of data acquisition. Figure 4.8 shows the desired sensitivity as a function of the signal acquisition time for σ_θ equal to 1, 5 and 10 mrad.

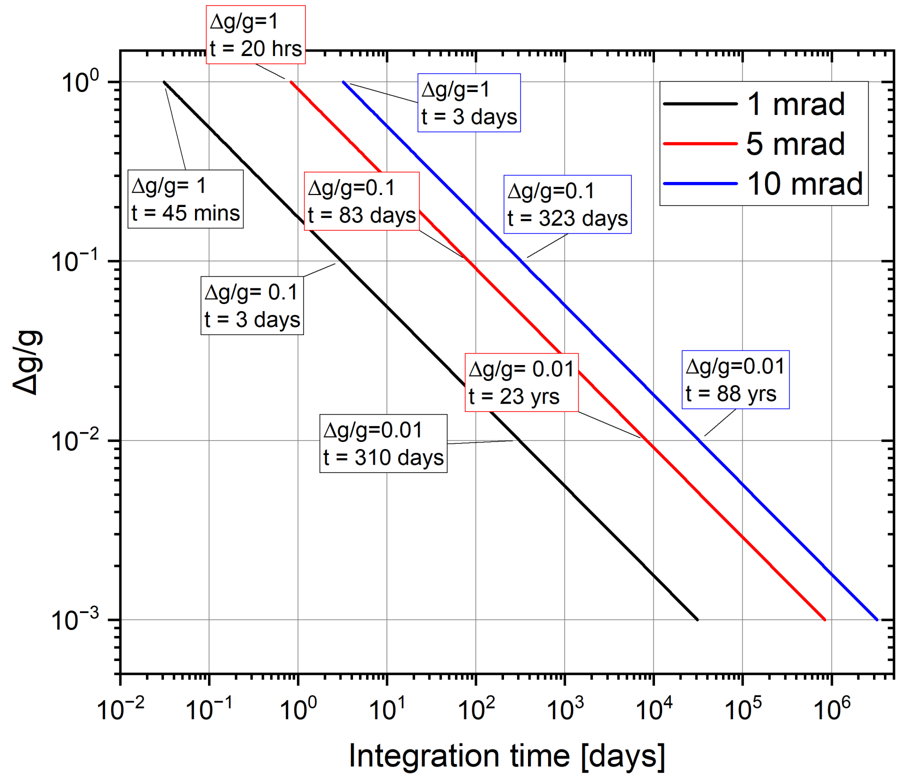

Figure 4.8: Behaviour of the relative error on gravitational acceleration as a function of the data acquisition time, for three values of the atomic beam angular standard deviation.

4.3 Bragg and SPLMT interferometers comparison

In this section we compare the interferometer proposed in this thesis with the literature, with reference to the Bragg interferometer (BI) proposed in Ref. [21]. In this regard, a similar interferometer has been designed and simulated: a standard Mach-Zehnder configuration (two $\pi/2$ pulses and one π-pulse) in Bragg regime at the first and fifth diffraction order, with detuning from the 2S-3P transition of the order of tens of GHz. To reduce the acquisition times, it is necessary to maximize the product $Ck_{\text{eff}}T^2$. For the comparison, a BI with the same T as the single photon LMT (SPLMT) has been considered. The Ps speed must also be equal because it strongly affects the atomic flux in the stages preceding the intererometer. This means that the lengths of the interferometers are the same but the BI waist along the z-direction must be much larger, about 7 mm. The constraint on the waist is given by the recoil frequency which sets a minimum value of the interaction time between the atoms and the pulses. The maximum power required by the BIs at the considered diffraction orders ranges from tens of W to kW. These powers with such laser beam sizes pose a major technological challenge, but we will neglect this aspect in this discussion to make an ideal comparison. The effective momentum is fixed by the design of the interferometers which is $2\hbar k$ for the first BI diffraction order and $10\hbar k$ for the SPLMT and the fifth BI order. The results are shown in Figure 4.10. The model used in for BIs pulses is described in section 2.2.1 and in Ref. [166]. Figure 4.9 provides a qualitative depiction of the transition probability for a 5th

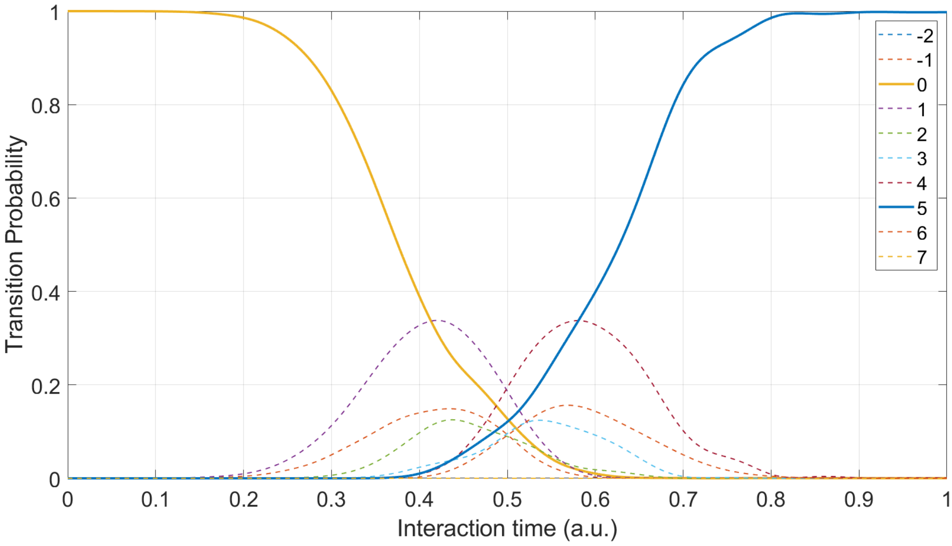

Figure 4.9: Transition probability of the atom after interaction with a Gaussian Bragg π-pulse as a function of the atom-pulse interaction time. The dashed curves represent the loss channels of the pulse, which are momentum states we aim to avoid populating.

order Bragg π-pulse as a function of normalized interaction time. The curves represent the momentum states with which the initial state can couple, based on the pulse parameters. The dashed curves represent states other than the initial and final states, indicating the loss channels of the pulse, which we don't want to populate. The interferometers have been simulated to analyze their efficiency as a function of the entrance angles and transverse coordinate, like in Figure 4.4. The efficiency of the BIs for θ_{y}=0 is higher because of the smaller number of pulses forming them (3 vs. 23), however, as soon as an imperfectly collimated atomic beam is considered, the Bragg efficiency collapses below that of the SPLMT interferometer due to the Bragg condition becoming more stringent at high atomic velocities. As the diffraction order increases, the angular acceptance decreases, and the efficiency drops to zero for lower values of θ_{y}. Note that this characteristic must also be considered in the alignment of the laser pulses, which must then respect a maximum relative angle with the atomic beam. The efficiency of BI as a function of input parameters related to the x direction is higher for first-order and equal to the SPLMT for fifth-order.

The time of flight through the interferometers is the same but the BIs do not create $n = 3$ states resulting in a different probability of survival to Ps beam decay,

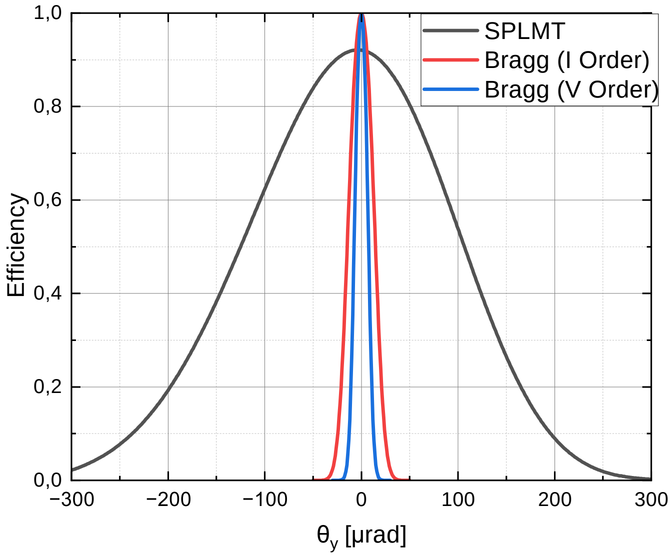

(a) Efficiency of the interferometers as a function of the y entrance angle for two Bragg diffraction orders. The degree of angular acceptance of Bragg interferometers decreases as the order of diffraction increases. The SPLMT interferometer has the best angular acceptance in the y direction which is the most critical.

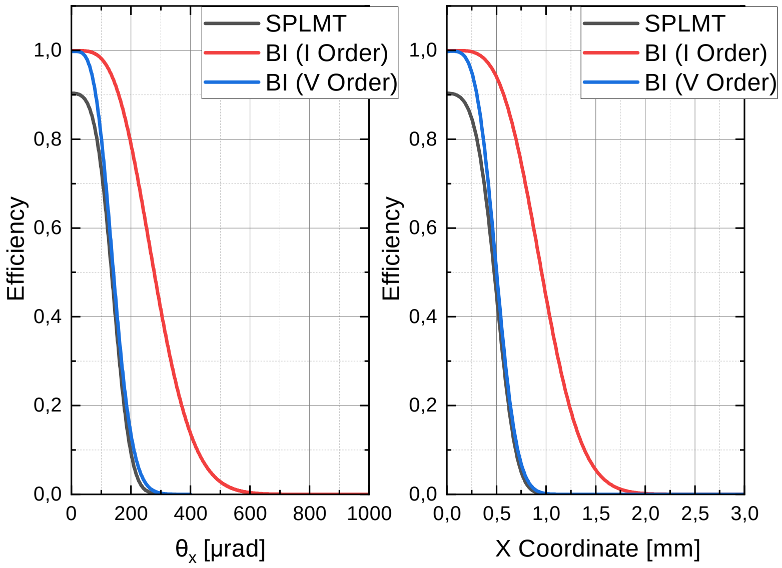

(b) Efficiency of the interferometers as a function of the x entrance angle and position for two Bragg diffraction orders. For the chosen parameters (see text), the BI results to be more efficient than the SPLMT.

Figure 4.10: Efficiency of the interferometers as a function of the entrance angles and position. The curves refer to different interferometric configurations: the Single Photon LMT interferometer discussed in this work (black), and the Bragg interferometers at the first (red) and the fifth (blue) diffraction order.

ϵ_{ann}. One of the main limitations of the BI is the impossibility of filtering the interferometric outputs based on the internal state. In fact, the atoms leaving the apparatus are in different momentum states but in the same internal state. This implies that in order to separate the arms and ensure that the signal spots do not overlap on the detector, several metres of downstream propagation could be necessary, resulting in a further loss due to annihilation (i.e. a further reduction of ϵ_{ann}), as already mentioned in Chapter 1. The separation of the spots must be sized according to the desired degree of angular acceptance and it is defined by

$$\Delta z_{sep} = [D_{\mathrm{y}} + 2\Delta z_{\mathrm{MZ}} \tan(\theta_{\mathrm{y}}^{\mathrm{max}})] \frac{v_{\mathrm{z}} m}{N_{do} \hbar k} \tag{4.33}$$

where D_y is the entrance hole diameter, Z_{MZ} is the interferometer length, $\theta_{\mathrm{y}}^{\mathrm{max}}$ is the maximum accepted angle of the atomic beam and N_{do} is the diffraction order. Choosing $D_{\mathrm{y}} = 0.25$ mm and $\theta_{\mathrm{y}}^{\mathrm{max}} = 125\ \mu$rad (as for the SPLMT), the propagation needed after the interferometer ranges from 32 m to 6.5 m from the first to the fifth order. As already mentioned, it is necessary to ensure that atoms with an angle greater than $\theta_{\mathrm{y}}^{\mathrm{max}}$ do not enter the interferometer via upstream collimation. This requires another 2.5 m of propagation. The total distance travelled by an atom exiting the microwave cavity would be 39.5 m and 14 m for the first and fifth diffraction order, respectively. ϵ_{ann} would be about 0.32% for the first order and 14% for the fifth order that should be compared with $\epsilon_{\mathrm{ann}} \sim 27\%$ of the SPLMT. In the Bragg configuration no mask is needed but the collimation reduces the atomic flux: ϵ_{BI}=$\epsilon_{\mathrm{ann}}\epsilon_{\mathrm{coll}}$. The beam is also collimated in the x direction so that the BIs operate at a minimum efficiency of about 30%: this selects a maximum angle and input coordinate that varies with diffraction order (see Figure 4.10, b). The ratio between the acquisition times of the two types of interferometers is given by

$$\frac{t_{\mathrm{BI}}}{t_{\mathrm{SPLMT}}} = \left(\frac{k^{\mathrm{eff}}_{\mathrm{SPLMT}} C_{\mathrm{SPLMT}}}{k^{\mathrm{eff}}_{\mathrm{BI}} C_{\mathrm{BI}}} \right)^2 \frac{\epsilon_{\mathrm{SPLMT}}}{\epsilon_{\mathrm{BI}}} \tag{4.34}$$

This ratio is shown in Figure 4.11 as a function of the BI's diffraction order for three angular standard deviation values. As the order increases, the ratio decreases due to the higher effective momentum and the lower separation length at the detection. This decrease is counteracted by the lower angular acceptance which is inversely proportional to the diffraction order (as shown in Figure 4.10). The higher value of the ratio at 0.1 mrad is due to the fact that, as σ_θ decreases, the contrast of SPLMT starts to increase earlier and more than that of BI. The difference between the curves at 1 and 3 mrad is not significative beacuse for $\sigma_\theta \geq 1$ mrad the contrasts and $\epsilon_{\mathrm{SPLMT}}/\epsilon_{\mathrm{BI}}$ are approximately constant. For fifth-order, the time ratio is driven by $C_{\mathrm{BI}}/C_{\mathrm{SPLMT}}$ and $\epsilon_{\mathrm{SPLMT}}/\epsilon_{\mathrm{BI}}$, where ϵ_{BI} is governed by the decay in the collimation and separation zone. Both ratios favor the SPLMT interferometer emphasizing the main differences between the two types of interferometer: BI is not optimal with high-speed atomic beams because of the minimal interaction time required between light and atom, and the detection mode is not selective on the internal atomic state. Given the technical difficulties of generating pulses with powers of tens of kW and waist of about 7 mm, it is not necessary to analyze and simulate BIs at higher orders. A Bragg interferometer may be feasible and cost-effective with a much slower beam, but a high reduction in speed would lead to a drastic reduction in atomic flux, both within the interferometer and in the focusing zone, resulting in an inconveniently large increase in integration time. This result shows that using a Single Photon LMT interferometer is more convenient than a Bragg interferometer for positronium inertial sensing.

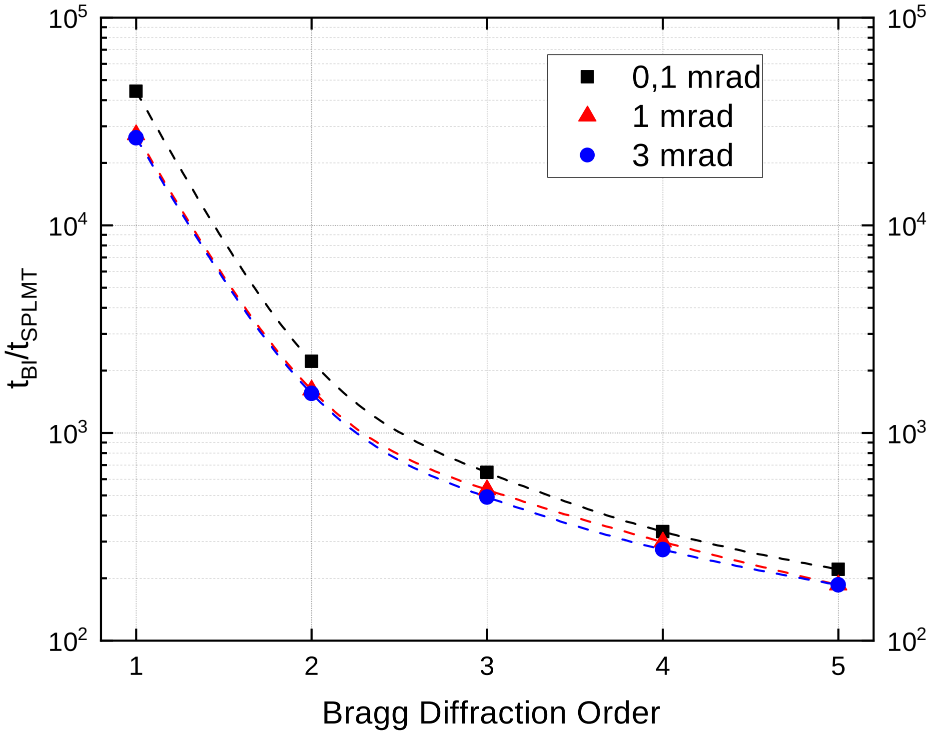

Figure 4.11: Data acquisition times ratio (Bragg over SPLMT) as a function of the first five Bragg diffraction orders, for three values of beam angular standard deviation. The rate decreases with the diffraction order and it is much greater than one for every order and σ_θ. The relative errors are lower than 5%.

Conclusions and future perspectives

This thesis explores the application of matter-wave interferometry techniques to antimatter, with a particular focus on measuring the gravitational effect on positronium atoms using a Large Momentum Transfer (LMT) interferometer and a high-power cavity for the photodetachment of the negative positronium ion. This study represents a significant step in the QUPLAS (Quantum Interferometry with Positrons and LASers) project, examining the feasibility of the experiment and addressing critical aspects of its implementation.

Matter-wave interferometry applied to positronium offers a unique window for testing the fundamental laws of physics, particularly gravity, on a purely leptonic system. Positronium, being the lightest bound state composed exclusively of leptons, represents a prime opportunity for high-precision experiments on exotic atoms.

The experimental part regarding photodetachment is still being refined, but simulation activities have demonstrated the feasibility of the experiment and provided guidance for optimizing the experimental setup. Specifically, simulations of the optical cavity were conducted using the MATLAB-based package OSCAR, FEM simulations via Ansys were performed to estimate the thermal effect on the mirrors caused by the high circulating power in the cavity, and Monte Carlo simulations were used to estimate the divergence of the photodetached beam. The results indicated that the thermal effect can be considered negligible and that a circulating power of about 200 kW should be achievable with the selected low-absorption mirrors. Additionally, the Monte Carlo simulations highlighted an expansion of the atomic beam following photodetachment, which, for the purposes of gravity measurement, can be mitigated by appropriately orienting the linear polarization of the laser field.

Despite being in the early stages of development, the cavity has been assembled and tested in air, showing that it is possible to use the Pound-Drever-Hall technique for laser locking through actuators on the diode current. The cavity exhibits characteristics similar to high-finesse cavities, with its finesse value measured using the Cavity Ring Down Spectroscopy technique. The measured finesse is lower than the nominal value (14,000 compared to 40,000), probably due to the non-negligible absorption of air in the near-infrared.

The final part of the thesis discusses the design of a single-photon LMT interferometer (SPLMT) to measure the gravitational effect on positronium.
The interferometer, like the entire experiment, is designed to operate with a very fast atomic beam and with a much higher energy spread compared to normal operational conditions for gravity measurements. These conditions are necessary because positronium has a short lifetime and can be focused in the form of Ps^-, which annihilates even faster. With the idea of operating a device with a wide angular acceptance, the work proposes a single-photon interferometer consisting of 23 pulses operating on the $2^3\mathrm{S}_1$-$3^3\mathrm{P}_2$ transition to exploit the relatively long lifetime of the $2^3\mathrm{S}_1$ state (1.14μs), with an interrogation time of less than one microsecond and an effective wave vector of $10\hbar k$.
The interferometer was simulated using the Monte Carlo method, with the parameters based on the atomic beam distributions. The results allowed for estimating the data integration time, which, for an atomic flux of 10^8 Ps/s with an angular divergence of 10 mrad and a relative measurement precision of $\frac{\Delta g}{g} = 10\%$, is approximately 11 months.
A quantum simulation was also conducted to estimate the influence of parasitic patterns generated due to non-idealities of the interferometer pulses. The result indicates that they do not have a significant influence.
The comparison between the SPLMT interferometer and the Bragg interferometer demonstrated that the SPLMT approach can offer greater sensitivity in measuring gravitational effects on positronium due to its higher robustness against the Doppler effect.

This work lays the foundation for a series of future developments in the project such as those listed below.

A. **Testing the photodetachment cavity in vacuum and at high power**
The next steps in the research will be crucial for testing the optical cavity for photodetachment under vacuum and high-power conditions. This will verify whether the cavity can achieve the desired power and its stability. If necessary, active or passive homogenization systems for the thermal profile of the mirrors and the laser beam wavefront can be developed, drawing on the extensive literature on the topic.

B. **Detailed analysis of other stages of the experiment**
Some components of the experimental system, such as the UV-microwave excitation system and the ionization system downstream of the interferometer, require more accurate sizing and efficiency estimation. It will be necessary to further design these systems to ensure they are optimized for the specific needs of the interferometer.

C. **Improving efficiency and optimizing the interferometer**

Once the operational parameter ranges of all stages of the experiment are carefully defined, it will be possible to determine the optimal parameters for the interferometer. This includes optimizing the effective wave vector, interrogation time, and atomic beam velocity. Techniques for efficiency enhancement can be considered, such as suppressing interferometer loss channels based on destructive interference of parasitic patterns. Additionally, the research will continue to explore other experimental configurations that may improve measurement efficiency and reduce demands on the atomic beam.

D. Studying other systematic effects

Although some systematic effects have already been addressed (e.g. gravity gradients, Earth's rotation), a more comprehensive analysis could be valuable. Other effects to consider may include, for instance, how the shape, alignment and chirp of the laser beams impact the interferometric phase.

E. Studying the interfacing between various stages of the experiment

Finally, it will be necessary to study more precisely how to interface the various stages of the experiment with each other. This involves optimizing the connections between positronium beam production, its preparation, passage through the interferometer, and final detection. A well-designed interface will ensure optimal signal transmission and minimize information loss during the measurement process.

In summary, this work has estimated the technical feasibility of the proposed experiment, highlighting its critical points and its potential impact on understanding gravity on quantum scales and verifying fundamental physics theories. The results obtained provide a solid foundation for future developments and refinements of the QUPLAS project, paving the way for new and promising lines of research in matter-wave interferometry and antimatter physics.

Bibliography

[1] M. Deutsch. Evidence for the formation of positronium in gases. *Phys. Rev.*, 82:455–456, May 1951.

[2] A. Rich. Recent experimental advances in positronium research. *Rev. Mod. Phys.*, 53:127–165, Jan 1981.

[3] E. Liang and C. D. Charles. Laser cooling of positronium. *Optics Communications*, 65(6):419–424, 1988.

[4] G. K. Savely. Precision study of positronium: Testing bound state QED theory. *International Journal of Modern Physics A*, 19(23):3879–3896, 2004.

[5] G. K. Savely. Precision physics of simple atoms: QED tests, nuclear structure and fundamental constants. *Physics Reports*, 422(1):1–63, 2005.

[6] J. Govaerts and M. V. Caillie. Neutrino decay of positronium in the Standard Model and beyond. *Physics Letters B*, 381(4):451–457, 1996.

[7] F. Castelli. The positronium atom as a benchmark for Rydberg excitation experiments in atomic physics. *The European Physical Journal Special Topics*, 203:137–150, Apr 2012.

[8] C. D. Dermer and J. C. Weisheit. Perturbative analysis of simultaneous Stark and Zeeman effects on n=1-n=2 radiative transitions in positronium. *Phys. Rev. A*, 40:5526–5532, Nov 1989.

[9] S. M. Curry. Combined Zeeman and motional Stark effects in the first excited state of positronium. *Phys. Rev. A*, 7:447–450, Feb 1973.

[10] M. L. Lewis and V. W. Hughes. Higher-order relativistic contributions to the combined Zeeman and motional Stark effects in positronium. *Phys. Rev. A*, 8:625–639, Aug 1973.

[11] F. C. Witteborn and W. M. Fairbank. Experimental comparison of the gravitational force on freely falling electrons and metallic electrons. *Phys. Rev. Lett.*, 19:1049–1052, Oct 1967.

[12] D. B. Cassidy. Experimental progress in positronium laser physics. *The European Physical Journal D*, 72:53, Mar 2018.

[13] H. Bondi. Negative mass in general relativity. *Rev. Mod. Phys.*, 29:423–428, Jul 1957.

[14] P. Morrison. Approximate nature of physical symmetries. *American Journal of Physics*, 26(6):358–368, 1958.

[15] J. Scherk. Antigravity: A crazy idea? *Physics Letters B*, 88(3):265–267, 1979.

[16] M. M. Nieto and T. Goldman. The arguments against “antigravity” and the gravitational acceleration of antimatter. *Physics Reports*, 205(5):221–281, 1991.

[17] E. G. Adelberger, B. R. Heckel, C. W. Stubbs, and Y. Su. Does antimatter fall with the same acceleration as ordinary matter? *Phys. Rev. Lett.*, 66:850–853, Feb 1991.

[18] F. M. Huber, R. A. Lewis, E. W. Messerschmid, and G. A. Smith. Precision tests of Einstein’s Weak Equivalence Principle for antimatter. *Advances in Space Research*, 25(6):1245–1249, 2000.

[19] G. Chardin and G. Manfredi. Gravity, antimatter and the Dirac-Milne universe. *Hyperfine Interactions*, 239(1):45, Oct 2018.

[20] O. Rousselle, P. Cladé, S. Guellati-Khélifa, R. Guérout, and S. Reynaud. Quantum interference measurement of the free fall of anti-hydrogen. *The European Physical Journal D*, 76(11):209, Nov 2022.

[21] M. K. Oberthaler. Anti-matter wave interferometry with positronium. *Nuclear Instruments and Methods in Physics Research Section B: Beam Interactions with Materials and Atoms*, 192(1):129–134, 2002.

[22] S. Mariazzi, R. Caravita, M. Doser, G. Nebbia, and R. S. Brusa. Toward inertial sensing with a 2^3S positronium beam. *The European Physical Journal D*, 74(4):79, Apr 2020.

[23] P. Crivelli, D. A. Cooke, and S. Friedreich. Experimental considerations for testing antimatter antigravity using positronium 1s-2s spectroscopy. *International Journal of Modern Physics: Conference Series*, 30:1460257, 2014.

[24] D. B. Cassidy and S. D. Hogan. Atom control and gravity measurements using Rydberg positronium. *International Journal of Modern Physics: Conference Series*, 30:1460259, Jan 2014.

[25] E. K. Anderson et al. Observation of the effect of gravity on the motion of antimatter. *Nature*, 621(7980):716–722, September 2023.

[26] C. Solaro, C. Debavelaere, P. Cladé, and S. Guellati-Khelifa. Atom interferometer driven by a picosecond frequency comb. *Phys. Rev. Lett.*, 129:173204, Oct 2022.

[27] A.P. Mills and M. Leventhal. Can we measure the gravitational free fall of cold rydberg state positronium? *Nuclear Instruments and Methods in Physics Research Section B: Beam Interactions with Materials and Atoms*, 192(1):102–106, 2002.

[28] S. Aghion et al. Laser excitation of the $n = 3$ level of positronium for antihydrogen production. *Phys. Rev. A*, 94:012507, Jul 2016.

[29] V. Mukhanov. Physical foundations of cosmology. *Cambridge University Press*, 2005:24, 2005.

[30] A. D. Sakharov. Violation of CP invariance, C asymmetry, and baryon asymmetry of the universe. *JETP Lett.*, 5:24, 1967.

[31] O. W. Greenberg. CPT violation implies violation of Lorentz invariance. *Phys. Rev. Lett.*, 89:231602, Nov 2002.

[32] D. Colladay and V. A. Kostelecký. CPT violation and the Standard Model. *Phys. Rev. D*, 55:6760–6774, Jun 1997.

[33] D. Colladay and V. A. Kostelecký. Lorentz-violating extension of the Standard Model. *Phys. Rev. D*, 58:116002, Oct 1998.

[34] V. A. Kostelecký and A. J. Vargas. Lorentz and CPT tests with hydrogen, antihydrogen, and related systems. *Phys. Rev. D*, 92:056002, Sep 2015.

[35] G. M. Tino. Testing gravity with cold atom interferometry: results and prospects. *Quantum Science and Technology*, 6(2):024014, Mar 2021.

[36] H. Batelaan, S. Bernet, M. K. Oberthaler, E. M. Rasel, J. Schmiedmayer, and A. Zeilinger. - classical and quantum atom fringes. In Paul R. Berman, editor, *Atom Interferometry*, pages 85–120. Academic Press, San Diego, 1997.

[37] S. Chu. Atom interferometry. In R. Kaiser, C. Westbrook, and F. David, editors, *Coherent atomic matter waves*, pages 317–370, Berlin, Heidelberg, 2001. Springer Berlin Heidelberg.

[38] S. Abend et al. Atom interferometry and its applications. 2020.

[39] Jr. Mills, A. P. and E. M. Gullikson. Solid neon moderator for producing slow positrons. *Applied Physics Letters*, 49(17):1121–1123, 10 1986.

[40] Hyeong il Kim et al. Electron-positron generation by irradiating various metallic materials with laser-accelerated electrons. *Results in Physics*, 57:107310, 2024.

[41] H. Bethe, W. Heitler, and Paul Adrien Maurice Dirac. On the stopping of fast particles and on the creation of positive electrons. *Proceedings of the Royal Society of London. Series A, Containing Papers of a Mathematical and Physical Character*, 146(856):83–112, 1934.

[42] G. Consolati, R. Ferragut, A. Galarneau, F. Di Renzo, and F. Quasso. Mesoporous materials for antihydrogen production. *Chem. Soc. Rev.*, 42:3821–3832, 2013.

[43] S. Aghion et al. Producing long-lived $2\,^3s$ positronium via $3\,^3p$ laser excitation in magnetic and electric fields. *Phys. Rev. A*, 98:013402, Jul 2018.

[44] P. Crivelli, U. Gendotti, A. Rubbia, L. Liszkay, P. Perez, and C. Corbel. Measurement of the orthopositronium confinement energy in mesoporous thin films. *Phys. Rev. A*, 81:052703, May 2010.

[45] Y. Nagashima and T. Sakai. First observation of positronium negative ions emitted from tungsten surfaces. *New Journal of Physics*, 8(12):319, Dec 2006.

[46] Y. Nagashima. Experiments on positronium negative ions. *Physics Reports*, 545(3):95–123, 2014.

[47] K. Michishio, T. Kanai, S. Kuma, T. Azuma, K. Wada, I. Mochizuki, T. Hyodo, A. Yagishita, and Y. Nagashima. Observation of a shape resonance of the positronium negative ion. *Nature Communications*, 7(1):11060, Mar 2016.

[48] Y. Nagashima, K. Michishio, L. Chiari, and Y. Nagata. An energy-tunable positronium beam produced via photodetachment of positronium negative ions and its applications. *Journal of Physics B: Atomic, Molecular and Optical Physics*, 54(21):212001, dec 2021.

[49] M. Sacerdoti, V. Toso, G. Vinelli, G. Rosi, L. Salvi, G. M. Tino, M. Giammarchi, and R. Ferragut. Towards the formation of a positronium coherent beam. *arXiv:2307.12894*, 2023.

[50] Akinori Igarashi, Isao Shimamura, and Nobuyuki Toshima. Photodetachment cross sections of the positronium negative ion. *New Journal of Physics*, 2(1):17, Aug 2000.

[51] L. Gurung, T. J. Babij, S. D. Hogan, and D. B. Cassidy. Precision microwave spectroscopy of the positronium $n = 2$ fine structure. *Phys. Rev. Lett.*, 125:073002, Aug 2020.

[52] M. Antonello et al. Efficient 2^3S positronium production by stimulated decay from the 3^3P level. *Phys. Rev. A*, 100:063414, Dec 2019.

[53] G. Feinberg, A. Rich, and J. Sucher. Quadratic zeeman effect in positronium. *Phys. Rev. A*, 41:3478–3480, Apr 1990.

[54] G. Vinelli, R. Ferragut, M. Giammarchi, G. Maero, M. Romé, and V. Toso. Real-time monitoring of a positron beam using a microchannel plate in single-particle mode. *Journal of Instrumentation*, 15(11):P11030, Nov 2020.

[55] C. N. Taylor, T. F. Fuerst, and M. Shimada. Characterization of coincidence Doppler broadening and positron annihilation lifetime systems at inl. *AIP Conference Proceedings*, 2182(1):040010, 2019.

[56] M. P. Petkov, M. H. Weber, K. G. Lynn, K. P. Rodbell, and S. A. Cohen. Doppler broadening positron annihilation spectroscopy: A technique for measuring open-volume defects in silsesquioxane spin-on glass films. *Applied Physics Letters*, 74(15):2146–2148, 1999.

[57] S. Sala, A. Ariga, A. Ereditato, R. Ferragut, M. Giammarchi, M. Leone, C. Pistillo, and P. Scampoli. First demonstration of antimatter wave interferometry. *Science Advances*, 5(5):eaav7610, 2019.

[58] A. Ariga et al. The quplas experimental apparatus for antimatter interferometry. *Nuclear Instruments and Methods in Physics Research Section A: Accelerators, Spectrometers, Detectors and Associated Equipment*, 951:163019, 2020.

[59] M. Charlton et al. Positron production using a 9 mev electron linac for the *GBAR* experiment. *Nuclear Instruments and Methods in Physics Research Section A: Accelerators, Spectrometers, Detectors and Associated Equipment*, 985:164657, 2021.

[60] A. Bacci et al. *TDR BriXSinO*: https://marix.mi.infn.it/wp-content/uploads/2022/04/BriXSino_TDR.pdf. Technical report, INFN, 2022.

[61] I. Drebot et al. *BriXSinO* high-flux dual X-ray and THz radiation source based on energy recovery linacs. *JACoW*, IPAC2022:THOXSP2, 2022.

[62] A. Bacci, F. Broggi, V. Petrillo, and L. Serafini. Low emittance positron beam generation: a comparison between photo-production and electro-production. *arXiv:2103.13167v1*, 2021.

[63] A. D. Cronin, J. Schmiedmayer, and D. E. Pritchard. Optics and interferometry with atoms and molecules. *Rev. Mod. Phys.*, 81:1051–1129, Jul 2009.

[64] A. Peters, K. Y. Chung, and S. Chu. High-precision gravity measurements using atom interferometry. *Metrologia*, 38(1):25, Feb 2001.

[65] J. M. McGuirk, G. T. Foster, J. B. Fixler, M. J. Snadden, and M. A. Kasevich. Sensitive absolute-gravity gradiometry using atom interferometry. *Phys. Rev. A*, 65:033608, Feb 2002.

[66] D. S. Durfee, Y. K. Shaham, and M. A. Kasevich. Long-term stability of an area-reversible atom-interferometer Sagnac gyroscope. *Phys. Rev. Lett.*, 97:240801, Dec 2006.

[67] R. H. Parker, C. Yu, W. Zhong, B. Estey, and H. Müller. Measurement of the fine-structure constant as a test of the Standard Model. *Science*, 360(6385):191–195, 2018.

[68] G. Rosi, F. Sorrentino, L. Cacciapuoti, M. Prevedelli, and G. M. Tino. Precision measurement of the Newtonian gravitational constant using cold atoms. *Nature*, 510(7506):518–521, Jun 2014.

[69] M. Kasevich and S. Chu. Atomic interferometry using stimulated Raman transitions. *Phys. Rev. Lett.*, 67:181–184, Jul 1991.

[70] D. M. Giltner, R. W. McGowan, and S. A. Lee. Atom interferometer based on Bragg scattering from standing light waves. *Phys. Rev. Lett.*, 75:2638–2641, Oct 1995.

[71] C. J. Bordé. Atomic interferometry with internal state labelling. *Physics Letters A*, 140(1):10–12, 1989.

[72] J. M. McGuirk, M. J. Snadden, and M. A. Kasevich. Large area light-pulse atom interferometry. *Phys. Rev. Lett.*, 85:4498–4501, Nov 2000.

[73] D. M. Greenberger and A. W. Overhauser. Coherence effects in neutron diffraction and gravity experiments. *Rev. Mod. Phys.*, 51:43–78, Jan 1979.

[74] R. P. Feynman and A. R. Hibbs. *Quantum Mechanics and Path Integrals.* New York, McGraw-Hill, 1965.

[75] P. Story and C. Cohen-Tannoudji. The feynman path integral approach to atomic interferometry. a tutorial. *J. Phys. II France*, 4(11), 1994.

[76] Charles Antoine. *Contribution à la théorie des interféromètres atomiques.* PhD thesis, Université Pierre et Marie Curie, 2004.

[77] R. P. Feynman. Space-time approach to non-relativistic quantum mechanics. *Rev. Mod. Phys.*, 20:367–387, Apr 1948.

[78] Xinan Wu. Gravity gradient survey with a mobile atom interferometer. 2009.

[79] Brenton Young, Mark Kasevich, and Steven Chu. Precision atom interferometry with light pulses. In Paul R. Berman, editor, *Atom Interferometry*, pages 363–406. Academic Press, San Diego, 1997.

[80] T. Byrnes and E. O. Ilo-Okeke. *Quantum Atom Optics: Theory and Applications to Quantum Technology.* Cambridge University Press, 2021.

[81] A. Chutjian and O.J. Orient. *Fast Beam Sources*, page 49–66. Elsevier, 1996.

[82] Stefan Hüfner. *Photoelectron Spectroscopy.* Springer Berlin Heidelberg, 2003.

[83] Linda Young. 15 - fast beam spectroscopy. In F.B. Dunning and Randall G. Hulet, editors, *Atomic, Molecular, and Optical Physics: Atoms and Molecules*, volume 29 of *Experimental Methods in the Physical Sciences*, pages 301–323. Academic Press, 1996.

[84] B. N. C. Tenorio, S. Coriani, A. B. Rocha, and M. A. C. Nascimento. Molecular photoionization and photodetachment cross sections based on l^2 basis sets: Theory and selected examples. In A. V. Glushkov, O. Yu. Khetselius, J. Maruani, and E. Brändas, editors, *Advances in Methods and Applications of Quantum Systems in Chemistry, Physics, and Biology*, pages 151–179, Cham, 2021. Springer International Publishing.

[85] K. Michishio, T. Tachibana, H. Terabe, A. Igarashi, K. Wada, T. Kuga, A. Yagishita, T. Hyodo, and Y. Nagashima. Photodetachment of positronium negative ions. *Phys. Rev. Lett.*, 106:153401, Apr 2011.

[86] Michishio K., L. Chiari, F. Tanaka, N. Oshima, and Y. Nagashima. A high-quality and energy-tunable positronium beam system employing a trap-based positron beam. *Review of Scientific Instruments*, 90, 2 2019.

[87] John Archibald Wheeler. Polyelectrons. *Annals of the New York Academy of Sciences*, 48(3):219–238, October 1946.

[88] Allen P. Mills. Observation of the positronium negative ion. *Phys. Rev. Lett.*, 46:717–720, Mar 1981.

[89] J. Botero and Chris H. Greene. Resonant photodetachment of the positronium negative ion. *Phys. Rev. Lett.*, 56:1366–1369, Mar 1986.

[90] A. K. Bhatia and Y. K. Ho. Complex-coordinate calculation of ^{1,3}p resonances in ps$^-$ using hylleraas functions. *Phys. Rev. A*, 42:1119–1122, Aug 1990.

[91] Y. K. Ho and A. K. Bhatia. P-wave shape resonances in positronium ions. *Phys. Rev. A*, 47:1497–1499, Feb 1993.

[92] M. Emami-Razavi and J. W. Darewych. Review of experimental and theoretical research on positronium ions and molecules. *The European Physical Journal D*, 75(6), June 2021.

[93] Allen Paine Mills. Cross section for photoionization of the positronium negative ion at the lowest feshbach resonance. *Canadian Journal of Physics*, 91(9):751–755, 2013.

[94] Akinori Igarashi. Calculation of two-photon detachment cross sections of the positronium negative ion. *Journal of Physics B: Atomic, Molecular and Optical Physics*, 45(24):245201, nov 2012.

[95] S. J. Ward, J. W. Humberston, and M. R. C. McDowell. Elastic scattering of electrons (or positrons) from positronium and the photodetachment of the positronium negative ion. *Journal of Physics B: Atomic and Molecular Physics*, 20(1):127, jan 1987.

[96] A. K. Bhatia and Richard J. Drachman. Photodetachment of the positronium negative ion. *Phys. Rev. A*, 32:3745–3747, Dec 1985.

[97] A. Igarashi, S. Nakazaki, and A. Ohsaki. Phase shifts of $e^- + \mathrm{Ps}$ scatterings and photodetachment cross sections of ps^-. *Phys. Rev. A*, 61:032710, Feb 2000.

[98] L. M. Branscomb and S. J. Smith. Experimental cross section for photodetachment of electrons from h^- and d^-. *Phys. Rev.*, 98:1028–1034, May 1955.

[99] Jérôme Degallaix. Oscar: A matlab based package to simulate realistic optical cavities. *SoftwareX*, 12:100587, 2020.

[100] Partha Saha. Fast estimation of transverse fields in high-finesse optical cavities. *J. Opt. Soc. Am. A*, 14(9):2195–2202, Sep 1997.

[101] Justin D. Mansell et al. Evaluating the effect of transmissive optic thermal lensing on laser beam quality with a shack–hartmann wave-front sensor. *Appl. Opt.*, 40(3):366–374, Jan 2001.

[102] P. L. Rall, D. Förster, T. Graf, and C. Pflaum. Simulation and compensation of thermal lensing in optical systems. *Opt. Express*, 30(21):38643–38662, Oct 2022.

[103] K. R. Hansen, T. T. Alkeskjold, J. Broeng, and J. Lægsgaard. Thermo-optical effects in high-power ytterbium-doped fiber amplifiers. *Opt. Express*, 19(24):23965–23980, Nov 2011.

[104] Yung-Sheng Huang, Hsien-Liang Tsai, and Fang-Ling Chang. Thermo-optic effects affecting the high pump power end pumped solid state lasers: Modeling and analysis. *Optics Communications*, 273(2):515–525, 2007.

[105] W. Winkler, K. Danzmann, A. Rüdiger, and R. Schilling. Heating by optical absorption and the performance of interferometric gravitational-wave detectors. *Phys. Rev. A*, 44:7022–7036, Dec 1991.

[106] W. Winkler, R. Schilling, K. Danzmann, J. Mizuno, A. Rüdiger, and K. A. Strain. Light scattering described in the mode picture. *Appl. Opt.*, 33(31):7547–7550, Nov 1994.

[107] Loïc Amoudry et al. Modal instability suppression in a high-average-power and high-finesse fabry–perot cavity. *Appl. Opt.*, 59(1):116–121, Jan 2020.

[108] G. Mueller, R. S Amin, D. Guagliardo, D. McFeron, R. Lundock, D. H. Reitze, and D. B. Tanner. Method for compensation of thermally induced modal distortions in the input optical components of gravitational wave interferometers. *Classical and Quantum Gravity*, 19(7):1793, mar 2002.

[109] K.A. Strain, K. Danzmann, J. Mizuno, P.G. Nelson, A. Rüdiger, R. Schilling, and W. Winkler. Thermal lensing in recycling interferometric gravitational wave detectors. *Physics Letters A*, 194(1):124–132, 1994.

[110] Jerome Degallaix. *Compensation of strong thermal lensing in advanced interferometric gravitational waves detectors*. PhD thesis, Western Australia U., 2006.

[111] H Wang et al. Thermal modelling of advanced ligo test masses. *Classical and Quantum Gravity*, 34(11):115001, may 2017.

[112] Aidan F. Brooks et al. Overview of advanced ligo adaptive optics. *Appl. Opt.*, 55(29):8256–8265, Oct 2016.

[113] The Virgo collaboration. Advanced virgo technical design report. Technical report, VIR-0128A-12, 2012.

[114] J. Ramette, M. Kasprzack, A. Brooks, C. Blair, H. Wang, and M. Heintze. Analytical model for ring heater thermal compensation in the advanced laser interferometer gravitational-wave observatory. *Appl. Opt.*, 55(10):2619–2625, Apr 2016.

[115] R. Lawrence, D. Ottaway, M. Zucker, and P. Fritschel. Active correction of thermal lensing through external radiative thermal actuation. *Opt. Lett.*, 29(22):2635–2637, Nov 2004.

[116] M. A. Arain, W. Z. Korth, L. F. Williams, R. M. Martin, G. Mueller, D. B. Tanner, and D. H. Reitze. Adaptive control of modal properties of optical beams using photothermal effects. *Opt. Express*, 18(3):2767–2781, Feb 2010.

[117] I. Nardecchia, Y. Minenkov, M. Lorenzini, L. Aiello, E. Cesarini, D. Lumaca, V. Malvezzi, F. Paoletti, A. Rocchi, and V. Fafone. Optimized radius of curvature tuning for the virgo core optics. *Classical and Quantum Gravity*, 40(5):055004, feb 2023.

[118] J. Cooper and R. N. Zare. Angular distribution of photoelectrons. *The Journal of Chemical Physics*, 48:942–943, 1 1968.

[119] V. T. Davis. *Introduction to Photoelectron Angular Distributions: Theory and Applications*. Springer International Publishing, 2022.

[120] Koji Michishio, Luca Chiari, Fumi Tanaka, and Yasuyuki Nagashima. Anisotropic photodetachment of positronium negative ions with linearly polarized light. *Phys. Rev. Lett.*, 132:203001, May 2024.

[121] Xiaohui Li, Xiwei Huang, Xichen Hu, Xiaoxiao Guo, and Yueheng Han. Recent progress on mid-infrared pulsed fiber lasers and the applications. *Optics & Laser Technology*, 158:108898, 2023.

[122] Eric D. Black. An introduction to Pound–Drever–Hall laser frequency stabilization. *American Journal of Physics*, 69(1):79–87, 01 2001.

[123] R. W. P. Drever, J. L. Hall, F. V. Kowalski, J. Hough, G. M. Ford, A. J. Munley, and H. Ward. Laser phase and frequency stabilization using an optical resonator. *Applied Physics B Photophysics and Laser Chemistry*, 31(2):97–105, June 1983.

[124] Thorlabs. Optical coatings: https://www.thorlabs.com/newgrouppage9.cfm?objectgroup_id=5840.

[125] Liufeng Li, Fang Liu, Chun Wang, and Lisheng Chen. Measurement and control of residual amplitude modulation in optical phase modulation. *Review of Scientific Instruments*, 83(4):043111, 04 2012.

[126] K. Kokeyama, K. Izumi, W. Z. Korth, N. Smith-Lefebvre, K. Arai, and R. X. Adhikari. Residual amplitude modulation in interferometric gravitational wave detectors. *J. Opt. Soc. Am. A*, 31(1):81–88, Jan 2014.

[127] H. Kogelnik and T. Li. Laser beams and resonators. *Appl. Opt.*, 5(10):1550–1567, Oct 1966.

[128] A. Siegman. *Lasers*. University Science Books, 1986.

[129] Orazio Svelto. *Principles of Lasers*. Springer US, 2010.

[130] D. A. Steck. *Classical and Modern Optics*. Open Access, 2021. https://atomoptics.uoregon.edu/~dsteck/teaching/optics/.

[131] M. J. Lawrence, B. Willke, M. E. Husman, E. K. Gustafson, and R. L. Byer. Dynamic response of a fabry–perot interferometer. *J. Opt. Soc. Am. B*, 16(4):523–532, Apr 1999.

[132] Michael J. Martin. *Quantum Metrology and Many-Body Physics: Pushing the Frontier of the Optical Lattice Clock*. PhD thesis, Harvey Mudd College, 20006.

[133] N. Ismail, C. C. Kores, D. Geskus, and M. Pollnau. Fabry-pérot resonator: spectral line shapes, generic and related airy distributions, linewidths, finesses, and performance at low or frequency-dependent reflectivity. *Opt. Express*, 24(15):16366–16389, Jul 2016.

[134] Atomic and Molecular Physics Division, Harvard-Smithsonian Center for Astrophysics. HIgh-resolution TRANsmission molecular absorption database (HITRAN).

[135] S.N. Mikhailenko, S. Kassi, D. Mondelain, and A. Campargue. Water vapor absorption between 5690 and 8340 cm^{-1}: Accurate empirical line centers and validation tests of calculated line intensities. *Journal of Quantitative Spectroscopy and Radiative Transfer*, 245:106840, 2020.

[136] H. Müller, S. Chiow, Q. Long, S. Herrmann, and S. Chu. Atom interferometry with up to 24-photon-momentum-transfer beam splitters. *Phys. Rev. Lett.*, 100:180405, May 2008.

[137] S. B. Cahn, A. Kumarakrishnan, U. Shim, T. Sleator, P. R. Berman, and B. Dubetsky. Time-domain de Broglie wave interferometry. *Phys. Rev. Lett.*, 79:784–787, Aug 1997.

[138] M. Weitz, B. C. Young, and S. Chu. Atomic interferometer based on adiabatic population transfer. *Phys. Rev. Lett.*, 73:2563–2566, Nov 1994.

[139] A. Wicht, J. M. Hensley, E. Sarajlic, and S. Chu. A preliminary measurement of the fine structure constant based on atom interferometry. *Physica Scripta*, 2002(T102):82, Jan 2002.

[140] A. Arvanitaki, P. W. Graham, J. M. Hogan, S. Rajendran, and K. Van Tilburg. Search for light scalar dark matter with atomic gravitational wave detectors. *Phys. Rev. D*, 97:075020, Apr 2018.

[141] Y. A. El-Neaj. AEDGE: Atomic experiment for dark matter and gravity exploration in space. *EPJ Quantum Technology*, 7(1):6, Mar 2020.

[142] S. Dimopoulos, P. W. Graham, J. M. Hogan, M. A. Kasevich, and S. Rajendran. Atomic gravitational wave interferometric sensor. *Phys. Rev. D*, 78:122002, Dec 2008.

[143] N. Yu and M. Tinto. Gravitational wave detection with single-laser atom interferometers. *General Relativity and Gravitation*, 43(7):1943–1952, Jul 2011.

[144] W. Chaibi, R. Geiger, B. Canuel, A. Bertoldi, A. Landragin, and P. Bouyer. Low frequency gravitational wave detection with ground-based atom interferometer arrays. *Phys. Rev. D*, 93:021101, Jan 2016.

[145] S. Loriani, D. Schlippert, C. Schubert, S. Abend, H. Ahlers, W. Ertmer, J. Rudolph, J. M. Hogan, M. A. Kasevich, E. M. Rasel, and N. Gaaloul. Atomic source selection in space-borne gravitational wave detection. *New Journal of Physics*, 21(6):063030, Jun 2019.

[146] Ming-Sheng Zhan et al. ZAIGA: Zhaoshan long-baseline atom interferometer gravitation antenna. *International Journal of Modern Physics D*, 29(04):1940005, 2020.

[147] C. Schubert, D. Schlippert, S. Abend, E. Giese, A. Roura, W. P. Schleich, W. Ertmer, and E. M. Rasel. Scalable, symmetric atom interferometer for infrasound gravitational wave detection, 2019.

[148] J. Rudolph, T. Wilkason, M. Nantel, H. Swan, C. M. Holland, Y. Jiang, B. E. Garber, S. P. Carman, and J. M. Hogan. Large momentum transfer clock atom interferometry on the 689 nm intercombination line of strontium. *Phys. Rev. Lett.*, 124:083604, Feb 2020.

[149] P. W. Graham, J. M. Hogan, M. A. Kasevich, S. Rajendran, and R. W. Romani. Mid-band gravitational wave detection with precision atomic sensors, 2017.

[150] P. W. Graham, J. M. Hogan, M. A. Kasevich, and S. Rajendran. New method for gravitational wave detection with atomic sensors. *Phys. Rev. Lett.*, 110:171102, Apr 2013.

[151] G Vinelli, F Castelli, R Ferragut, M Romé, M Sacerdoti, L Salvi, V Toso, M Giammarchi, G Rosi, and G M Tino. A large-momentum-transfer matter-wave interferometer to measure the effect of gravity on positronium. *Classical and Quantum Gravity*, 40(20):205024, sep 2023.

[152] O. Homburg and T. Mitra. Gaussian-to-top-hat beam shaping: an overview of parameters, methods, and applications. In Alexis V. Kudryashov, Alan H. Paxton, and Vladimir S. Ilchenko, editors, *Laser Resonators, Microresonators, and Beam Control XIV*, volume 8236, page 82360A. International Society for Optics and Photonics, SPIE, 2012.

[153] A. Laskin and V. Laskin. Imaging techniques with refractive beam shaping optics. In Andrew Forbes and Todd E. Lizotte, editors, *Laser Beam Shaping XIII*, volume 8490, page 84900J. International Society for Optics and Photonics, SPIE, 2012.

[154] S. Ngcobo, K. Ait-Ameur, I. Litvin, A. Hasnaoui, and A. Forbes. Tuneable Gaussian to flat-top resonator by amplitude beam shaping. *Opt. Express*, 21(18):21113–21118, Sep 2013.

[155] Anne Louchet-Chauvet, Tristan Farah, Quentin Bodart, André Clairon, Arnaud Landragin, Sébastien Merlet, and Franck Pereira Dos Santos. The influence of transverse motion within an atomic gravimeter. *New Journal of Physics*, 13(6):065025, jun 2011.

[156] G. Rosi, G. D'Amico, L. Cacciapuoti, F. Sorrentino, M. Prevedelli, M. Zych, Č Brukner, and G. M. Tino. Quantum test of the equivalence principle for atoms in coherent superposition of internal energy states. *Nature Communications*, 8(1):15529, Jun 2017.

[157] F. Sorrentino, Q. Bodart, L. Cacciapuoti, Y.-H. Lien, M. Prevedelli, G. Rosi, L. Salvi, and G. M. Tino. Sensitivity limits of a Raman atom interferometer as a gravity gradiometer. *Phys. Rev. A*, 89:023607, Feb 2014.

[158] G. T. Foster, J. B. Fixler, J. M. McGuirk, and M. A. Kasevich. Method of phase extraction between coupled atom interferometers using ellipse-specific fitting. *Opt. Lett.*, 27(11):951–953, Jun 2002.

[159] S. Chiow, T. Kovachy, J. M. Hogan, and M. A. Kasevich. Generation of 43 w of quasi-continuous 780 nm laser light via high-efficiency, single-pass frequency doubling in periodically poled lithium niobate crystals. *Opt. Lett.*, 37(18):3861–3863, Sep 2012.

[160] E. Seise, A. Klenke, J. Limpert, and A. Tünnermann. Coherent addition of fiber-amplified ultrashort laser pulses. *Opt. Express*, 18(26):27827–27835, Dec 2010.

[161] I. N. Meshkov, V. N. Pavlov, A. O. Sidorin, and S. L. Yakovenko. A cryogenic source of slow monochromatic positrons. *Instruments and Experimental Techniques*, 50(5):639–645, Sep 2007.

[162] D. Trezzi. *Study of Positronium Converters in the AEgIS Antimatter Experiment*. PhD thesis, Università degli Studi di Milano, 2010.

[163] We can define the spatial extension of the Ps wave function in the laser beams propagation direction as $\Delta y_{\mathrm{Ps}} = \hbar/\Delta p$ and $\Delta p = 2m_{\mathrm{e}}\Delta v_y = 2m_{\mathrm{e}}v_z\tan(\Delta\theta_y)$, where $\mathrm{m_e}$ is the mass of the electron, $\mathrm{v_z}$ is the Ps velocity in the direction of propagation assumed constant and θy is the Ps entrance angle between the directions z and y. We can assume a collimation that sets $\Delta\theta y = 1$ mrad, which gives $\Delta y_{\mathrm{Ps}} \simeq 10$ nm. The minimum spatial separation between the centres of two wave functions that propagate in the interferometer is $\Delta y_{\min} = \frac{2\Delta z\hbar k}{v_z 2m_e} \simeq 0.38\mu$m with the distance Δz between two laser beams equal to 4 mm. Given that $\Delta y_{\mathrm{Ps}} < \Delta y_{\min}$ we can consider that two wave functions overlap only when their trajectories intersect at a laser pulse.

[164] A. Béguin, T. Rodzinka, L. Calmels, B. Allard, and A. Gauguet. Atom interferometry with coherent enhancement of bragg pulse sequences. *Phys. Rev. Lett.*, 131:143401, Oct 2023.

[165] A. M. Alonso, B. S. Cooper, A. Deller, S. D. Hogan, and D. B. Cassidy. Positronium decay from $n = 2$ states in electric and magnetic fields. *Phys. Rev. A*, 93:012506, Jan 2016.

[166] H. Müller, S. Chiow, and S. Chu. Atom-wave diffraction between the Raman-Nath and the Bragg regime: Effective Rabi frequency, losses, and phase shifts. *Phys. Rev. A*, 77:023609, Feb 2008.